DOT/FAA/AR-03/64

Office of Aviation Research
Washington, D.C. 20591

Effect of Airfoil Geometry on Performance With Simulated Ice Accretions Volume 1: Experimental Investigation

August 2003

Final Report

U.S. Department of Transportation
Federal Aviation Administration

NOTICE

Technical Report Documentation Page

1. Report No.	2. Government Accession No.	3. Recipient's Catalog No.
DOT/FAA/AR-03/64		

4. Title and Subtitle	5. Report Date
EFFECT OF AIRFOIL GEOMETRY ON PERFORMANCE WITH SIMULATED ICE ACCRETIONS VOLUME 1: EXPERIMENTAL INVESTIGATION	August 2003
	6. Performing Organization Code

7. Author(s)	8. Performing Organization Report No.
Andy P. Broeren, Sam Lee, Christopher M. LaMarre, and Michael B. Bragg	

9. Performing Organization Name and Address	10. Work Unit No. (TRAIS)
University of Illinois at Urbana-Champaign 104 S. Wright Street Urbana, IL 61801	11. Contract or Grant No.

12. Sponsoring Agency Name and Address	13. Type of Report and Period Covered
U.S. Department of Transportation Federal Aviation Administration Office of Aviation Research Washington, DC 20591	Final Report
	14. Sponsoring Agency Code AIR-100

15. Supplementary Notes

The FAA William J. Hughes Technical Center Technical Monitor was James Riley.

16. Abstract

This report presents the key findings of a 3-year experimental investigation into the effects of ice shape and airfoil geometry on airfoil performance. The overall objective of this report was to improve the understanding of the relationship between airfoil geometry, ice shape geometry, and the resulting degradation in aerodynamic performance. Three airfoils were tested with three different types of simulated ice accretions. The types of ice shapes were (1) supercooled, large droplet (SLD) ridge-type ice, (2) intercycle ice, and (3) glaze horn type ice. The NACA 23012, NLF 0414, and NACA 3415 airfoils were chosen to provide a broad range of aerodynamic characteristics.

The full parametric variation of ice shape simulations and airfoil geometry testing was carried out at the University of Illinois. Airfoil performance and surface pressure coefficients were acquired during angle of attack sweeps at $Re = 1.0\times10^6$, $Ma = 0.10$ and $Re = 1.8\times10^6$, $Ma = 0.18$. In addition, higher Reynolds (from 2.0×10^6 to 10.6×10^6) and Mach number (from 0.10 to 0.28) testing was performed for a subset of the ice-shape matrix on the NACA 23012 airfoil at the NASA Langley Low-Turbulence Pressure Tunnel.

The major conclusion of this study was that the chordwise location of an ice accretion feature is equally important as its size in determining the airfoil performance degradation, particularly in terms of maximum lift. The results of this study also showed that areas close to the leading edge were not necessarily the most sensitive in terms of ice accretion performance degradation. In all cases tested, the smallest performance loss occurred when the ice shape was located at the leading edge. This study continued to support the conclusion than an airfoil's load distribution plays a signal role in its sensitivity to ice accretion, particularly in the first 20% chord where ice is most likely to accrete. The results with SLD ridge-type ice simulations generally indicated that more front-loaded airfoils tended to be more sensitive to these types of ice accretion. Finally, the results of this study have shown that Reynolds and Mach number effects are small for ice-contaminated airfoils. There was little variation in the integrated aerodynamic coefficients for a Reynolds number range from 1.0×10^6 to 10.5×10^6 and over a Mach number range of 0.10 to 0.28. The effect of Reynolds and Mach numbers were especially small when compared to the performance degradations due to the simulated ice shapes.

17. Key Words	18. Distribution Statement
Simulated ice shape, Iced airfoil, Ridge ice, Glaze ice, Intercycle ice, Aerodynamic penalty, Performance degradation	This document is available to the public through the National Technical Information Service (NTIS) Springfield, Virginia 22161.

19. Security Classif. (of this report)	20. Security Classif. (of this page)	21. No. of Pages	22. Price
Unclassified	Unclassified	120	

TABLE OF CONTENTS

LIST OF FIGURES

LIST OF TABLES

EXECUTIVE SUMMARY

This report presents the key findings of a 3-year investigation into the effects of ice shape and airfoil geometry on airfoil performance. The overall objective of this investigation was to improve the understanding of the relationship between airfoil geometry, ice shape geometry, and the resulting degradation in aerodynamic performance. The new information obtained was applied as part of this study to the formulation of a preliminary methodology to determine critical ice shape geometry, including the influence of airfoil geometry on the critical ice shape geometry. An additional objective was to determine the effects of Reynolds and Mach numbers for both clean and iced airfoil configurations.

To accomplish these objectives, three airfoils were each tested with three different types of simulated ice accretions. The types of ice shapes tested were (1) supercooled large droplet (SLD) ridge-type ice, (2) intercycle ice, and (3) glaze horn-type ice. The simulation method for each of these ice shape types was different and is detailed in the report. The airfoils used in this investigation were the NACA 23012, the NLF 0414, and the NACA 3415. These airfoils were chosen to encompass a broad range of aerodynamic characteristics. The NACA 23012 is a traditional forward-loaded, low pitching moment airfoil. In contrast, the NLF 0414 was designed to maintain laminar flow over most of the upper surface. This resulted in a more uniform pressure loading over the forward and mid-chord regions. The NACA 3415 had aerodynamic characteristics between the other two airfoils.

The full parametric variation of ice shape simulations and airfoil geometry testing was carried out at the University of Illinois, using the low-speed wind tunnel. The NACA 23012, NLF 0414, and NACA 3415 airfoil models had an 18-inch chord and a 25% simple flap. The lift coefficient, drag coefficient, pitching-moment coefficient, flap hinge moment coefficient, and surface pressure coefficients were acquired during angle of attack sweeps at $Re = 1.0\times10^6$, $Ma = 0.10$ and $Re = 1.8\times10^6$, $Ma = 0.18$. In addition, higher Reynolds number and Mach number testing was performed for a subset of the ice shape matrix on the NACA 23012 airfoil. This testing was conducted at the NASA Langley Low-Turbulence Pressure Tunnel using an unflapped, 36-inch chord model. Since this was a pressure tunnel, a large range of Reynolds numbers (from 2.0×10^6 to 10.6×10^6) and Mach numbers (from 0.10 to 0.28) were tested.

A major conclusion of this study was that the chordwise location of an ice accretion feature is equally important as its size in determining the airfoil performance degradation, particularly in terms of maximum lift. For the NACA 23012 airfoil, a quarter-round shape with height $k/c = 0.0139$ resulted in a $C_{l,max}$ of less than 0.25 when located in the range of $x/c = 0.10$ to 0.20. However, a glaze horn-type shape with a height of $k/c = 0.0667$ (nearly five times larger) located at $s/c = 0.034$ (close to the leading edge) resulted in a higher $C_{l,max}$ of approximately 0.30. Therefore, a much smaller ice accretion located further downstream of the leading edge caused nearly the same or larger performance loss (in terms of $C_{l,max}$). This same trend was also true for the NACA 3415 airfoil. For the NLF 0414 airfoil, the lowest $C_{l,max}$ measured with the $k/c = 0.0139$ quarter round was 0.58 when located far downstream at $x/c = 0.30$. The lowest $C_{l,max}$ with the much larger ($k/c = 0.0667$) glaze horn shape had a similar value of 0.51. The results of this study showed that areas close to the leading edge were not necessarily the most

sensitive in terms of ice accretion performance degradation. In all cases tested, the smallest performance loss occurred when the ice shape was located at the leading edge ($x/c = s/c = 0.000$).

This study supports the conclusion than an airfoil's pressure load distribution plays a signal role in its sensitivity to ice accretion, particularly in the first 20% chord where ice is most likely to accrete. The results with SLD ridge-type ice simulations generally indicated that more front-loaded airfoils tended to be more sensitive to these types of ice accretion. Of the three airfoils tested, the NACA 23012 was the most front-loaded and had the largest performance degradation due to spanwise ridge ice accretions, especially when located in the range of $x/c = 0.10$ to 0.20. The NLF 0414 airfoil, which was the most aft-loaded of the three airfoils tested, was the least sensitive to SLD ice simulations. The NACA 3415 had a pressure loading between the NACA 23012 and the NLF 0414 airfoils. The results of this study showed that the performance penalties for this airfoil with the SLD ice simulations were also between the other two airfoils. This trend was also generally true for the other two types of ice shapes tested. These conclusions directly contributed to the application of the results to a methodology for determining a critical ice shape.

The results of this study have shown that Reynolds and Mach numbers effects are small for ice-contaminated airfoils. There was little variation in the integrated aerodynamic coefficients for a Reynolds number range from 1.0×10^6 to 10.5×10^6 and over a Mach numbers range of 0.10 to 0.28. Because of this Reynolds and Mach numbers insensitivity, a geometric scaling of a full-size airfoil section and ice accretion to small sizes suitable for small wind tunnels can yield very acceptable performance results. There can still be significant Reynolds and Mach numbers effects on clean airfoils. If the changes in the aerodynamic coefficients due to icing (when compared to the clean airfoil) need to be known, these effects could be significant. However, clean airfoil data at high Reynolds and Mach numbers can be more easily obtained through computational methods, historical data, or lower-cost (relative to iced configuration) aerodynamic testing.

1. INTRODUCTION.

This report summarizes the key findings of a 3-year investigation into the effect of ice shape and airfoil geometry on airfoil performance. Because the ice accretion process is dependent upon both atmospheric and aerodynamic conditions, many different sizes, shapes, locations, and textures result. It is also known that the resulting aerodynamic performance penalties are dependent upon the airfoil geometry, in the case of a conventional, fixed wing aircraft. For the purposes of this investigation, a subset of three ice accretion types was selected as typically encompassing many features of the wide array documented throughout the past 50 years of icing research. Likewise, three airfoils were selected that had very different aerodynamic characteristics and geometries. This report illustrates how different types of ice accretions have varying aerodynamic effects depending upon the baseline airfoil. The effects of Reynolds and Mach numbers were also explored for some cases.

The three classes of ice shapes considered in this investigation were glaze horn-type ice, supercooled large droplet (SLD) runback ridge ice, and intercycle ice. Glaze horn-type ice refers to leading-edge horn-shaped glaze ice accretions that form in the Appendix C envelope of icing conditions. These are classic glaze type ice shapes that have been documented in countless icing tunnel tests and in flight. Supercooled large droplet runback ridge ice refers to the spanwise ridge-type ice shapes that can form aft of a deicer surface in SLD icing conditions. This type of accretion was the subject of detailed investigations after the ATR-72 accident at Roselawn, Indiana, in October of 1994. Attention to the potential aerodynamic severity of intercycle-type ice accretions is perhaps the most recent and is usually always mentioned in conjunction with residual ice accretions. These accretions result from the cyclic operation of a typical pneumatic aircraft deicing system. Pneumatic boots operated in automatic mode are often inflated and deflated at either 1- or 3-minute intervals, depending upon the severity of icing. After the system has been cycled a sufficient number of times, the periodic activation and ice accretion cycle reaches steady state. After steady state has been reached, intercycle ice refers to the ice shape as it exists immediately before subsequent activations of the deicer. This is not to be confused with residual ice, which refers to any ice that remains on the surface immediately after the deicer activation.

The three airfoils used in this investigation were the NACA 23012, the NLF 0414, and the NACA 3415. These airfoils encompass a distinct range of aerodynamic characteristics. For example, the NACA 23012 is a traditional forward-loaded section having low pitching moment. Boundary layer transition on the upper surface is close to the leading edge at moderate to high lift coefficients. On the other hand, the NLF 0414 airfoil was designed to maintain a laminar boundary layer over a majority of the upper surface at moderate lift coefficients. As a result, the pressure loading is more uniform over the leading-edge and mid-chord regions. Both of these sections (or similar airfoils from those families) have been used, or are currently in use, on turbopropeller or piston-engine aircraft. The NACA 3415 airfoil was selected because it has aerodynamic characteristics that lie between the other two. While not nearly as popular for aircraft use as the NACA 23012, this airfoil has aerodynamic characteristics similar to NACA six-series airfoils, which have been quite widely used for aircraft applications.

Some background information that led to the selection of these ice shape classifications and airfoil types is provided in section 2 of this report. Previous studies are referenced and reviewed

where appropriate. The details of the ice shape simulation methods and parametric variations of size, location, roughness, etc., are given in section 3. This section also describes the various wind tunnel facilities, airfoil models, and aerodynamic conditions used during the experimental investigation. The differences in the clean and iced airfoil characteristics are presented in section 4. The results used to develop the critical ice shape methodology are provided in section 5. Finally, section 6 summarizes this work and states the main conclusions and recommendations.

1.1 MOTIVATION.

In general terms, the primary motivation for this investigation is to ensure the safety of present and future aircraft operations in an icing environment. That said, there were several contributing factors that helped define the scope of this investigation. One of these arose through a previous study commissioned by the Federal Aviation Administration (FAA). Bragg and Loth [1] employed experimental and computational methods to analyze the aerodynamic effect of SLD ridge-type ice accretions on two airfoils, the NACA 23012 and the NLF 0414. The results of this work showed that the former airfoil was more sensitive to this type of ice accretion. The lowest maximum lift coefficient ($C_{l,max}$) measured for the NACA 23012 with simulated ridge ice, having a height-to-chord ratio (k/c) of 0.0139 on the upper surface, was 0.25. The lowest $C_{l,max}$ measured for the NLF 0414 with the same ice accretion simulation was 0.68. Another important finding was that the upper surface location of the ridge ice simulation had a larger effect, in terms of maximum lift, for the NACA 23012 airfoil than for the NLF 0414 airfoil. These results contributed directly to the formulation of the present investigation by providing the basis for selecting the NACA 23012 and the NLF 0414 airfoils and including the SLD ridge-type accretions in the parametric variation. In this way, the present investigation is a logical extension of the study reported by Bragg and Loth.

Another motivation for this research was contributing to the efforts of the FAA 12A Working Group to develop guidance material, working methods, and recommendations for establishing the criticality of ice accretion characteristics on aircraft aerodynamic performance and handling qualities [2]. This research is directly applicable to the airfoil sensitivity approach described in the 12A Working Group report. The idea behind this approach is to gauge the sensitivity of an airfoil to ice contamination represented by various geometries over a range of locations on the airfoil. Less emphasis is placed upon determining the atmospheric conditions that would lead to such an ice shape. The working group suggested that research be conducted in support of this approach. One of the specific tasks mentioned was an investigation of aerodynamic effects of parametric variation in ice accretion features (such as upper horn height and location) on different types of airfoil geometries.

The 12A Working Group defined the concept of a critical ice shape based upon determining the minimal amounts of ice contamination required to exceed some critical level of aircraft performance and control degradation. This concept implies that the degradation or change in an aerodynamic parameter that would significantly affect the safety of flight can be identified. The minimum sized roughness, protuberance, or contamination is then determined that would cause each parameter to achieve this critical level. The last step would be to determine the icing conditions (if any) that could produce an ice accretion with those roughness and protuberance

features. The concept of a critical ice shape or critical ice shape methodology is important to the objectives of this study.

1.2 OBJECTIVES.

The overall objective of this investigation is to improve ones understanding of the relationship between airfoil geometry, ice shape geometry, and the resulting degradation in aerodynamic performance. This is essential information for the development of the critical ice shape concept as previously described. Contributing to this effort, the primary objective of this investigation is to formulate a preliminary methodology to determine critical ice shape geometry, including the influence of airfoil geometry. Aerodynamic performance testing was carried out on three airfoils (NACA 23012, NLF 0414, and NACA 3415) with parametric variations in ice shape simulations. The three classes of ice shapes tested were glaze horn-type shapes, SLD ridge shapes, and intercycle shapes and roughness. In the case of the former two, the size and upper surface location of the ice shape simulation were also parametrically varied. The standard measurements included lift coefficient, drag coefficient, pitching-moment coefficient, surface pressure distribution and, in some cases, for airfoil models with flaps, hinge-moment coefficient was also determined. The airfoils were tested at the University of Illinois wind tunnel at Reynolds numbers from 1.0×10^6 to 1.8×10^6 and Mach numbers from 0.10 to 0.18. In addition, higher Reynolds number and Mach number testing was performed for a limited number of cases, using the Low-Turbulence Pressure Tunnel (LTPT) at NASA Langley Research Center. The Reynolds number range covered by these tests was 2.0×10^6 to 10.5×10^6 and the corresponding Mach number range was 0.10 to 0.28.

2. BACKGROUND.

The purpose of this section is to review previous government-sponsored research at the University of Illinois because it relates to the activities summarized in this report. Some of this material was partially described in section 1.1. This lays the foundation for the presentation of the key results of the present investigation. The references included herein provide more comprehensive literature reviews for each classification of icing investigated.

2.1 SUPERCOOLED LARGE DROPLET ICE ACCRETIONS.

The initial study of SLD ice accretions reported by Bragg and Loth [1] was motivated, in part, by the ATR-72 accident at Roselawn, Indiana. An important component to that study was a consideration of the effect of ice on aircraft control. For this reason, the NACA 23012 airfoil used in that study was built with a 25% chord simple flap. This allowed for direct measurement of the hinge moment. As explained in their report, SLD can impinge and accrete ice downstream of ice protection systems designed for icing conditions, which are defined in Title 14 Code of Federal Regulations (CFR) Part 25 Appendix C. This may lead to the formation of a spanwise running ridge or step. For the purposes of the present investigation, this is referred to as a ridge ice accretion. It is usually associated with SLD conditions, but may also form in other conditions. This type of ice shape was simulated with a forward-facing quarter round of various heights (k). Different ridge shapes (e.g., backward-facing quarter-round, half-round, triangular, etc.) were also tested. Bragg and Loth [1] found that the simulated SLD ice shapes significantly affected the aerodynamic performance of the NACA 23012 airfoil. The ice shape also had a

significant effect on the flap hinge moment. The maximum lift coefficient was reduced from 1.50 (clean) to 0.25 with a $k/c = 0.0139$ quarter round located at $x/c = 0.12$ for $Re = 1.8\times10^6$ and $Ma = 0.18$. The change in maximum lift coefficient was a function of the upper surface location of the quarter round. Profound effects were also observed in the pitching moment and hinge moment coefficients for the airfoil with the quarter round. Large nose-down, pitching moments and trailing edge up flap hinge moments were generated before and during the stall.

The second part of the initial study of ridge ice accretions on airfoils involved experiments with the NLF 0414 airfoil. Like the NACA 23012 model, the NLF 0414 was also equipped with a 25% chord simple flap. While the quarter-round ice simulation caused significant effects on the performance of the NLF 0414 airfoil, they were not as severe as for the NACA 23012. For example, the lowest $C_{l,max}$ value measured was 0.68 compared to the clean value of 1.35 for $Re = 1.8\times10^6$ and $Ma = 0.18$. Unlike for the NACA 23012, there was only a small variation of maximum lift with the chordwise location of the quarter round. In further contrast, the ice shape simulations had a much smaller effect on the hinge moment coefficients for the NLF 0414 than for the NACA 23012.

The profound differences in the behavior of these two airfoils with the simulated ridge ice accretions is thoroughly discussed in the report by Bragg and Loth [1]. In addition, there are many other sources available in the public domain that detail these findings. A comprehensive literature review, discussion of the experimental methods and uncertainties, and more results can be found in the Ph.D. thesis by Lee [3]. References 4, 5, and 6 are three papers that provide additional analysis of this type of data. These key publications will be referred to frequently throughout this report. In this investigation, the quarter-round ice shape simulations were tested on the intermediate airfoil (NACA 3415) to complete the parametric variation of airfoil type for this classification of icing type. In addition, a limited number of quarter-round cases were tested on the NACA 23012 airfoil at the NASA Langley LTPT in order to gauge the Reynolds and Mach numbers effects.

2.2 INTERCYCLE ICE ACCRETIONS.

The effect of residual and intercycle ice accretions was considered as a part of the present investigation; however, some results have already been formally reported to the FAA and will, therefore, be covered in less detail in this report. The portion of this work that has already been reported was a collaborative effort between the FAA, NASA Glenn Research Center at Lewis Field, Goodrich Corporation, and the University of Illinois. The purpose was to characterize the nature of residual and intercycle ice accretions, determine the magnitude of the resulting performance penalties, and determine if a more detailed study was warranted [7]. The residual and intercycle ice was accreted on a 36-inch chord NACA 23012 airfoil equipped with a typical pneumatic deicing boot at the Goodrich Icing Wind Tunnel. Molds were made of selected intercycle ice accretions. Ice shape casting simulations were built from these molds and were tested on another 36-inch chord airfoil model at the NASA Langley LTPT. The ice shape castings were considered to be the highest fidelity simulation of the actual ice accretions. They captured all of the spanwise and three-dimensional variations in these shapes. The resulting aerodynamic performance penalties were found to be very severe. The maximum lift coefficient was typically reduced from 1.80 (clean) to 0.70 (iced) and stall angles were reduced from 17°

(clean) to 9° (iced) for $Re = 7.5\times10^6$ and $Ma = 0.21$. In addition to the iced airfoil testing, the clean NACA 23012 airfoil was tested for a large range of Reynolds and Mach numbers ($Re = 2.0\times10^6$ to 10.5×10^6 and $Ma = 0.10$ to 0.28). More analysis of the data, plus more information about the residual and intercycle ice characteristics, can also be found in reference 8.

The results presented in references 7 and 8 provide important information about the characteristics of residual and intercycle ice that were used in the present investigation to ascertain the airfoil sensitivity. The ice accretion castings were used as the basis for roughness simulations that were tested on all three airfoils in the Illinois wind tunnel. The LTPT data were considered as the standard of comparison for these tests on the NACA 23012 airfoil. All of the intercycle ice shape simulations were tested on all three of the airfoils, to complete the full parametric variation.

2.3 GLAZE HORN-TYPE ACCRETIONS.

The simulation of traditional glaze horn-type ice accretions was initiated under a grant from the NASA Glenn Research Center. This program is summarized in a paper by Kim and Bragg [9]. The objective was to determine the individual effects of glaze horn-type ice characteristics like horn height, radius, angle, and chordwise position. The authors tested a 3 by 3 matrix of horn shapes encompassing three different heights (k/c) and three different radii at the tip of the horn. Each of these nine shapes was tested at six different locations around the leading edge (thus, varying the position and angle) on a NLF 0414 airfoil model. This flapped model was identical to the one described in section 2.1. The geometry of the simulated ice horns was based upon measurements of ice shapes (i.e., upper surface horns) accreted in Appendix C conditions in the Icing Research Tunnel at NASA Glenn. Unlike the actual accretions, the simulations had no variation in the spanwise direction. The results showed that the simulated horn size and location had the largest effect on airfoil maximum lift, while the radius effects were small in comparison. More details can be found in reference 9.

In the present investigation, a subset of the glaze horn-type simulations were tested on the NACA 23012 and the NACA 3415 airfoils. The size, radius, and location details are given in section 3.3, and only single-horn shapes were used. This testing completed the airfoil geometry variation for this classification of ice shape type. A small subset of the glaze horn-type simulations were also tested on the NACA 23012 airfoil at the LTPT to provide higher Reynolds and Mach numbers data.

3. EXPERIMENTAL METHODS AND APPARATUS.

This section describes the various facilities, airfoil models, ice shape simulation methods, and test matrices employed in this investigation. The wind tunnels used were the Low-Speed Wind Tunnel (LSWT) at the University of Illinois and the LTPT at the NASA Langley Research Center. A total of five airfoil models were used. There were three versions of the NACA 23012 airfoil to complement the NLF 0414 and the NACA 3415 models. Each of the three classifications of ice accretion types were simulated using different methods.

3.1 FACILITIES.

3.1.1 Illinois LSWT.

The LSWT, shown in figure 1, is a conventional, open-return type having test section dimensions of 33.6 inches high by 48 inches wide by 96 inches long. The maximum speed attainable in the empty test section was 235 ft/sec (160 mph), which corresponded to a Reynolds number of 1.5×10^6 per foot and a Mach number of 0.21. Since this is an atmospheric facility, the Reynolds and Mach numbers cannot be independently controlled. The inlet contraction ratio was 7.5:1, and the inlet settling chamber had a 4-inch-thick honeycomb flow straightener followed by four turbulence reduction screens. The resulting turbulence intensity in the working section was generally less than 0.1% for all operating speeds over a 10- to 5000-Hz bandwidth [10]. During the data acquisition, the velocity was adjusted for each model angle of attack until the Reynolds number was within 2% of the desired value.

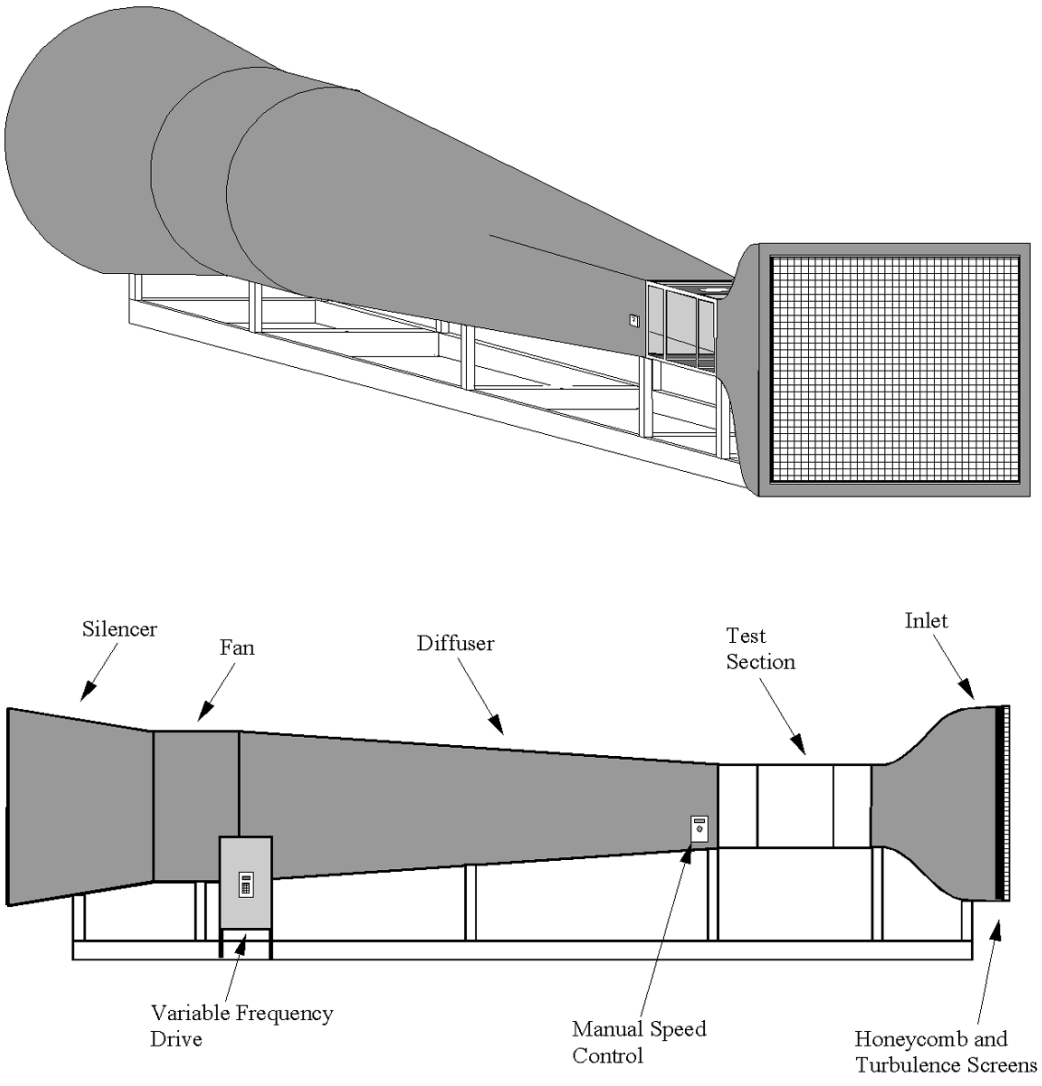

FIGURE 1. ILLINOIS LSWT

For this investigation, all the airfoil models were mounted vertically spanning the 33.6-inch height of the test section. The models were supported from the floor-mounted force balance. This cantilevered arrangement required small gaps (≈0.020 inch) between the ends of the model and the test section floor and ceiling. The three-component force balance was manufactured by Aerotech, Ltd., (see reference 11 for additional information). The force balance measurements of lift and quarter-chord pitching moment were compared to the integrated surface static-pressure measurements. Good agreement between these methods was observed, except when large ice shape simulations located near the airfoil leading edge were tested. The force balance data were considered more reliable in these cases because the ice shape simulations did not have static-pressure orifices. Therefore, the majority of the lift and pitching moment data presented in this report are from the integrated surface static pressures, except for the large leading-edge ice shape cases. The drag coefficient was determined from wake survey measurements using the standard momentum-deficit method. A traversable wake rake, having 59 stagnation pressure probes, was built specifically for this purpose. The integrated performance coefficients were corrected for solid and wake blockage and streamline curvature effects using the methods of Rae and Pope [12] and Allen and Vincenti [13].

Three of the four LSWT airfoil models had 25% chord simple flaps. This arrangement required additional apparatus to actuate the flap and measure the hinge moment. A linear traverse system combined with a two-arm linkage was used for flap positioning. A strain gauge load cell was incorporated into one of the linkage members. The load cell was calibrated prior to each test by applying calibration weights to the flap via a pulley system. There was usually good agreement between the hinge moment determined from the load cell and the integrated surface static pressures. Therefore, the majority of the hinge moment data present in this report are from the integrated surface static pressures, to be consistent with the lift and pitching moment data. More details about the experimental arrangement at the Illinois LSWT can be found in references 1, 3, and 6.

3.1.2 NASA Langley LTPT.

The LTPT, shown schematically in figure 2, is a closed return wind tunnel that is principally used for two-dimensional (2-D) airfoil testing and is described in detail in references 14 and 15. It can be operated at stagnation pressures from near vacuum to 147 psia (except 15 to 20 psia) and over a Mach number range of 0.05 to 0.40. The maximum Reynolds number is dependent upon the Mach number. For example, the maximum Reynolds number per foot is 15×10^6 at a Mach number of 0.22. Since the tunnel can be pressurized, it was possible to independently control the Reynolds and Mach numbers over certain ranges of either parameter. A heat exchanger and nine turbulence reduction screens were located in the inlet-settling chamber. The contraction ratio was 17.6:1, and the test section dimensions were 36 inches wide by 90 inches high by 90 inches long. The tunnel was designed for 2-D airfoil testing with model chord lengths up to 36 inches [14]. The free-stream turbulence levels are generally less than 0.1% for all operating conditions [15]. Given these specifications, the LTPT is capable of simulating near-flight conditions for 2-D airfoil models.

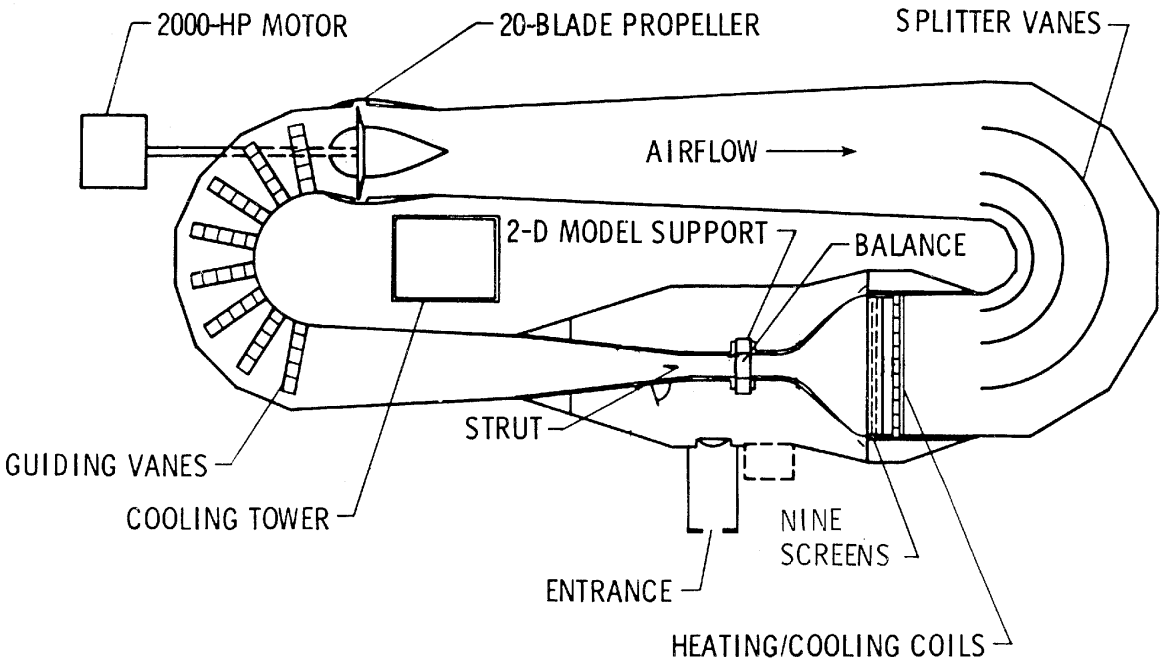

FIGURE 2. NASA LANGLEY LTPT

The 36-inch chord NACA 23012 airfoil model was supported horizontally across the width of the test section between two 34.5-inch-diameter circular end plates. The end plates are flush with the sidewalls and rotate for angle of attack adjustment. They also contained a section of porous plate for sidewall boundary layer control. This sidewall venting system was originally developed for testing high-lift, multielement airfoil configurations, and a detailed description is given by Pascal, et al. [16]. During the testing, some runs were performed with and without sidewall venting and there was very little difference in the results (see Broeren and Bragg [7] for more details). All the data presented here were acquired with sidewall venting, except for the data at $Re = 2.0\times10^6$, since this capability was not available for this condition.

The LTPT was equipped with a three-component force balance; however, it was designed for operation with high-lift airfoil systems and for higher dynamic pressures than were run in these experiments. Therefore, the data from the force balance were deemed unreliable, except at the higher dynamic pressures, and the lift and pitching moment data were generally determined from the integration of surface static pressures. All of the lift and pitching-moment coefficient data from the LTPT presented in this report were determined from the pressure integration, except for the large glaze horn-type simulated ice shapes located near the airfoil leading edge. Since these simulations did not have pressure taps, these data were not completely accurate. Therefore, the data from the force balance were used for the higher dynamic pressures. The pitching-moment coefficient was determined for the quarter-chord location. Drag coefficients were calculated from wake pressures measured with a wake rake, using the standard moment-deficit method. Corrections to the integrated performance coefficients accounting for solid and wake blockage and streamline curvature were applied to the data during postprocessing using the methods of Allen and Vincenti [13].

3.2 AIRFOIL MODELS.

3.2.1 Illinois LSWT Models.

The data presented in this report were acquired using four different airfoil models in the LSWT. They were (1) NACA 23012m with flap, (2) NLF 0414 with flap, (3) NACA 3415 with flap, and (4) NACA 23012 (no flap). All of the models had an 18-inch chord with 33.56-inch span and were built using a composite construction method. The outer shell or skin was molded from carbon fiber, and the models used rectangular steel spars to provide added structure. The spars extended 4 inches past one end of the model to provide for mounting in force balance. Three of the models had 25% chord (4.5 inches) simple flap, with the hinge location at $x/c = 0.779$ (or 14 inches). The flap gap was sealed on the lower surface using a 1-inch-wide strip of Mylar. This sealing method prevented airflow through the flap gap without adversely affecting the hinge-moment load cell measurements.

The NACA 23012m airfoil model with flap was used extensively in previous work, and details about this model can be found in references 1, 3, 4, and 6. The "m" designation after 23012 indicates that the airfoil was slightly modified from the true NACA coordinates. This difference was relatively minor and is thoroughly documented in the previous work. The majority of data showing the effect of ridge ice simulations on NACA 23012 performance were acquired using this model. However, some runs were performed using the single-element NACA 23012 for comparison. No significant differences in the iced airfoil results were observed.

The NLF 0414 airfoil model was also used extensively in previous work, and details about this model can be found in references 5, 9, 17, and 18. In the previous work, this model was tested with the full array of glaze horn-type ice simulations along with the ridge ice simulations. Testing performed for the present investigation involved the intercycle ice simulations.

The single-element NACA 23012 and the flapped NACA 3415 were built specifically for the present investigation. Both of these models had steel inserts fabricated into the leading edge at each end of the model to allow for mounting of the glaze horn-type ice simulations. The NACA 23012 model had 87 surface static pressure orifices. As shown in figure 3(a), 68 of these were located along the main chordwise row and 19 were located along a spanwise row at $x/c = 0.70$ on the upper surface. The NACA 3415 airfoil model had 62 taps on the main element and 28 taps on the flap (including 13 spanwise taps), as shown in figure 3(b). For both models, the main chordwise tap row was angled at 15° with respect to the direction of flow so that the orifices would be located outside a possible turbulent-flow wedge generated by the orifices upstream. The spanwise taps were used to gauge the extent of spanwise variation in the flow near the test section walls. The flap geometry used for the NACA 3415 is shown in figure 4. A typical model installation in the LSWT is shown in figure 5.

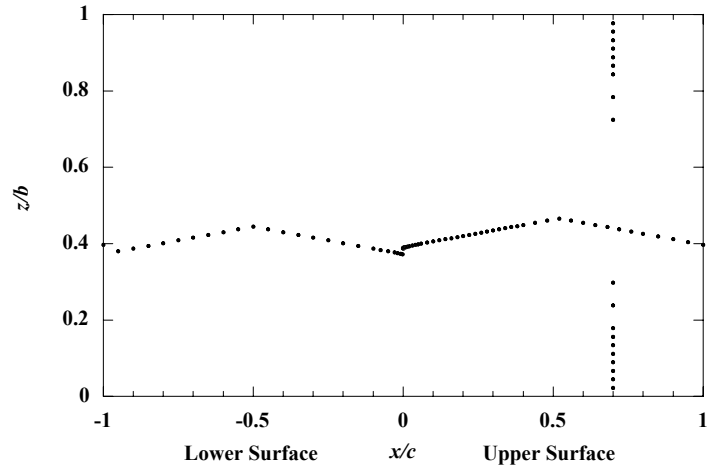

(a) NACA 23012

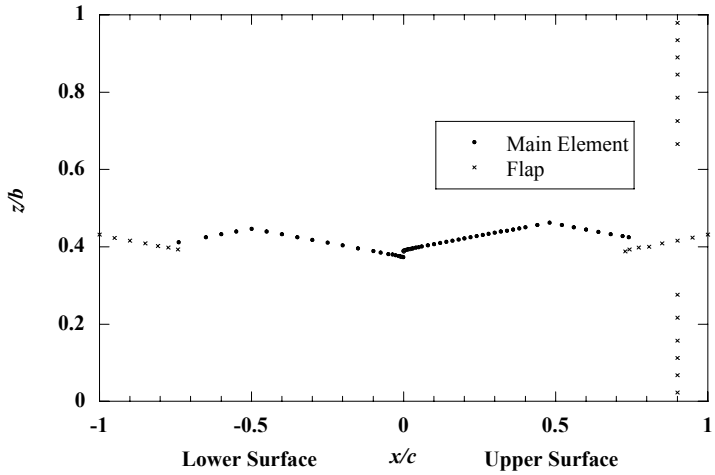

(b) NACA 3415

FIGURE 3. SURFACE PRESSURE TAP LAYOUT ON LSWT MODELS

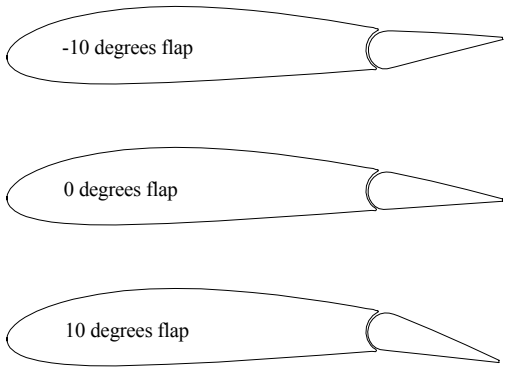

FIGURE 4. FLAP CONFIGURATION ON NACA 3415 MODEL

FIGURE 5. LOW-SPEED WIND TUNNEL TEST SECTION

3.2.2 NASA Langley LTPT Model.

The 36-inch chord, single-element NACA 23012 airfoil model was machined from solid aluminum and had recessed cavities for pressure instrumentation. The model was designed and built with a removable leading edge. There was a single baseline, or clean leading edge, and an alternate leading edge. The high-fidelity intercycle ice shape castings were mounted to the alternate leading edge. In addition, an instrumentation slice was installed near the model midspan. The instrumentation slice was cut out of stainless steel to match the ice shape contour. This allowed for a good approximate pressure distribution around the ice shape and also provided pressures for determination of the lift and pitching-moment coefficients. The simulated SLD ridge shapes (forward-facing quarter round) and the simulated glaze horn-type shapes were bolted onto the removable leading edge. An array of holes were drilled and tapped to mount the shapes in various chordwise locations. Figure 6 shows the model mounted in the test section with a simulated ice shape. The baseline model had 67 static pressure orifices along the main chordwise row and 17 orifices in a spanwise row located at $x/c = 0.70$ on the upper surface. This pressure tap layout is shown in figure 7.

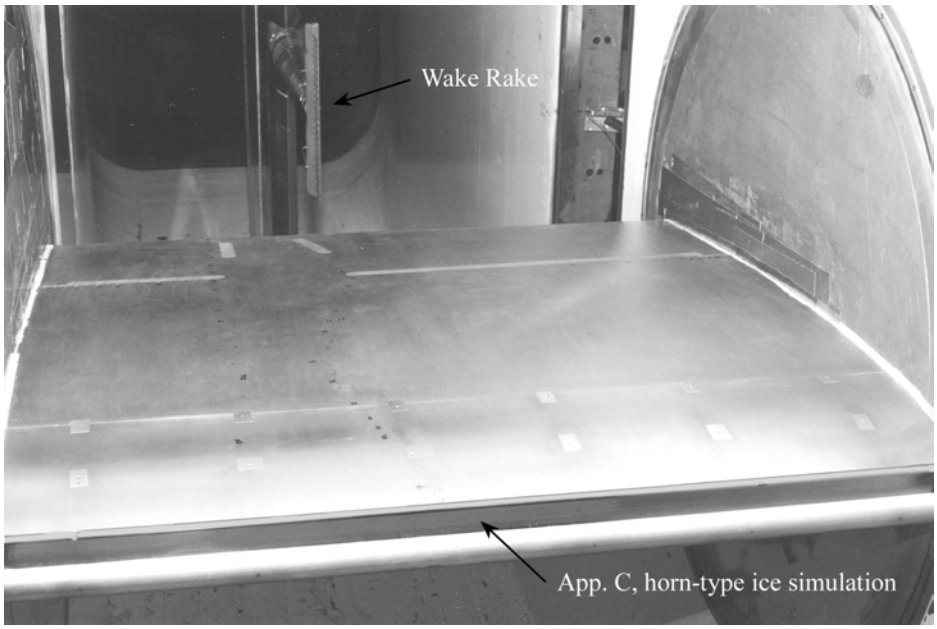

FIGURE 6. LOW-TURBULENCE PRESSURE TUNNEL TEST SECTION

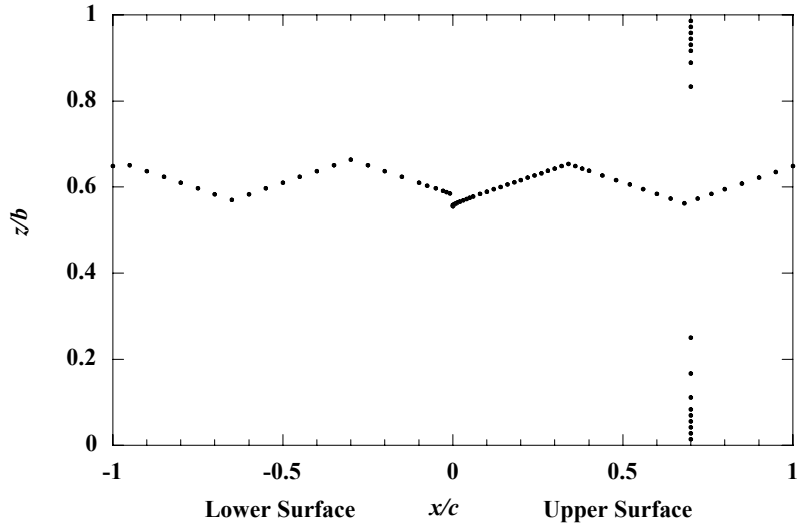

FIGURE 7. SURFACE PRESSURE TAP LAYOUT ON LTPT NACA 23012 MODEL

3.3 ICE SHAPE SIMULATIONS.

3.3.1 Supercooled Large Droplet, Ridge-Type Ice Simulation.

For tests in the Illinois LSWT, the SLD ridge-type ice accretions were simulated using wooden forward-facing quarter rounds with 0.10- and 0.25-inch heights. These heights corresponded to k/c values of 0.0056 and 0.0139, respectively. This geometry was used because it has a vertical step facing the flow, which is consistent with the shape of accretions that form aft of a wing ice

protection system during an SLD encounter. The quarter-round shapes were uniform in cross section across the span of the wind tunnel model. The quarter rounds were simply taped to the model surface at the desired chordwise location. For most of the cases tested, the boundary layer was tripped at $x/c = 0.02$ on the upper surface and at $x/c = 0.05$ on the lower surface. The trip consisted of glass microbeads, sized to trip the boundary layer on the clean model. The NACA 23012m and the NLF 0414 were tested with 0.0125-inch ($k/c = 0.00069$) microbeads [1]. Later calculations showed that these were larger than was required to trip the flow. The NACA 3415 was tested with smaller 0.0080-inch ($k/c = 0.00044$) microbeads based on this finding. The microbeads were applied onto a 0.003-inch-thick by 0.25-inch-wide, double-sided tape, using a sparse coverage (approximately less than 20%). The models were tripped for two reasons. When the leading-edge deicing boot is activated, it usually does not remove all the ice accretion. Instead, a residual ice roughness is usually left behind, which causes the flow to be turbulent (or at least transitional) from the leading edge. Another reason for the trip was to provide a fixed transition location for Computational Fluid Dynamics (CFD) simulations. Figure 8 shows the NACA 23012 airfoil with the $k/c = 0.0139$ forward-facing quarter round located at $x/c = 0.10$.

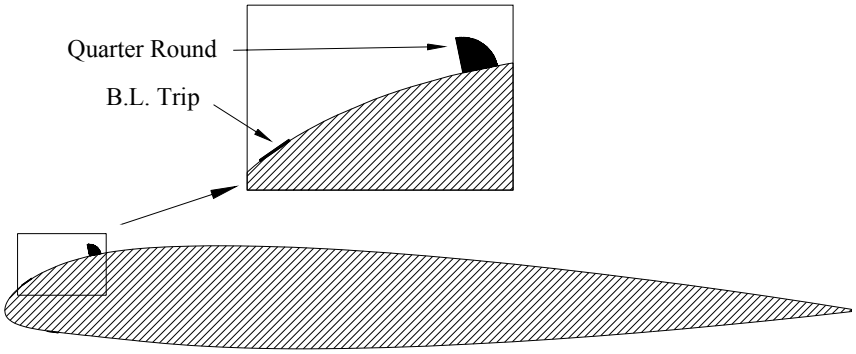

FIGURE 8. QUARTER-ROUND ICE SHAPE SIMULATION ON NACA 23012 MODEL

Tests conducted with simulated ridge-type ice accretions in the NASA Langley LTPT were very similar to those described above. In this case, the forward-facing quarter round was built from aluminum and bolted to the airfoil model. Aluminum tape was then placed over the quarter round to prevent any airflow between it and the airfoil surface. Only the $k/c = 0.0139$ (0.50 inch) simulation was tested. The boundary layer was tripped as described above using 80- to 100-grit microbeads (0.0083 to 0.0059 inch in diameter).

3.3.2 Intercycle Ice Simulations.

The intercycle ice simulations tested in the Illinois LSWT were based upon the four ice accretion castings tested at the NASA Langley LTPT. The characteristics of these four ice shapes, including tracings and photographs, are presented in references 7 and 8. They are designated as ice shape 290, 296, 312, and 322, after the icing run number. Tracings for each of these shapes are shown in figure 9. The ice shape castings used for the LTPT testing represented the highest level of simulation, since these shapes, in particular, had very irregular roughness size and spanwise variation. Despite this, a common characteristic among the shapes were ridge-like features that were distinct formations in the roughness. Because of the irregularities, the simulations used in the Illinois LSWT were built-up using various sizes of loose grit

roughnesses. This included silicon carbide, aluminum oxide, and ground walnut shells. These materials are commonly used in industrial finishing processes. The roughness height and distribution were determined from the photographs and tracings of the actual ice shapes. The heights and locations were scaled by the chord length. That is, the k/c and x/c values were preserved between the ice shape and the roughness simulation. This was also true for the NLF 0414 and the NACA 3415 airfoils. This was the best approximation that could be made for these airfoils. The actual intercycle shapes on these airfoils would likely be different in some respects from those acquired on the NACA 23012. However, this did not compromise the objective of this investigation, which was to determine the effect of this classification of shape on different airfoils. In fact, to determine the effect of airfoil shape on the aerodynamics with intercycle ice, the same ice shape must be tested. Determination of the icing conditions that would lead to such a shape was a secondary concern here.

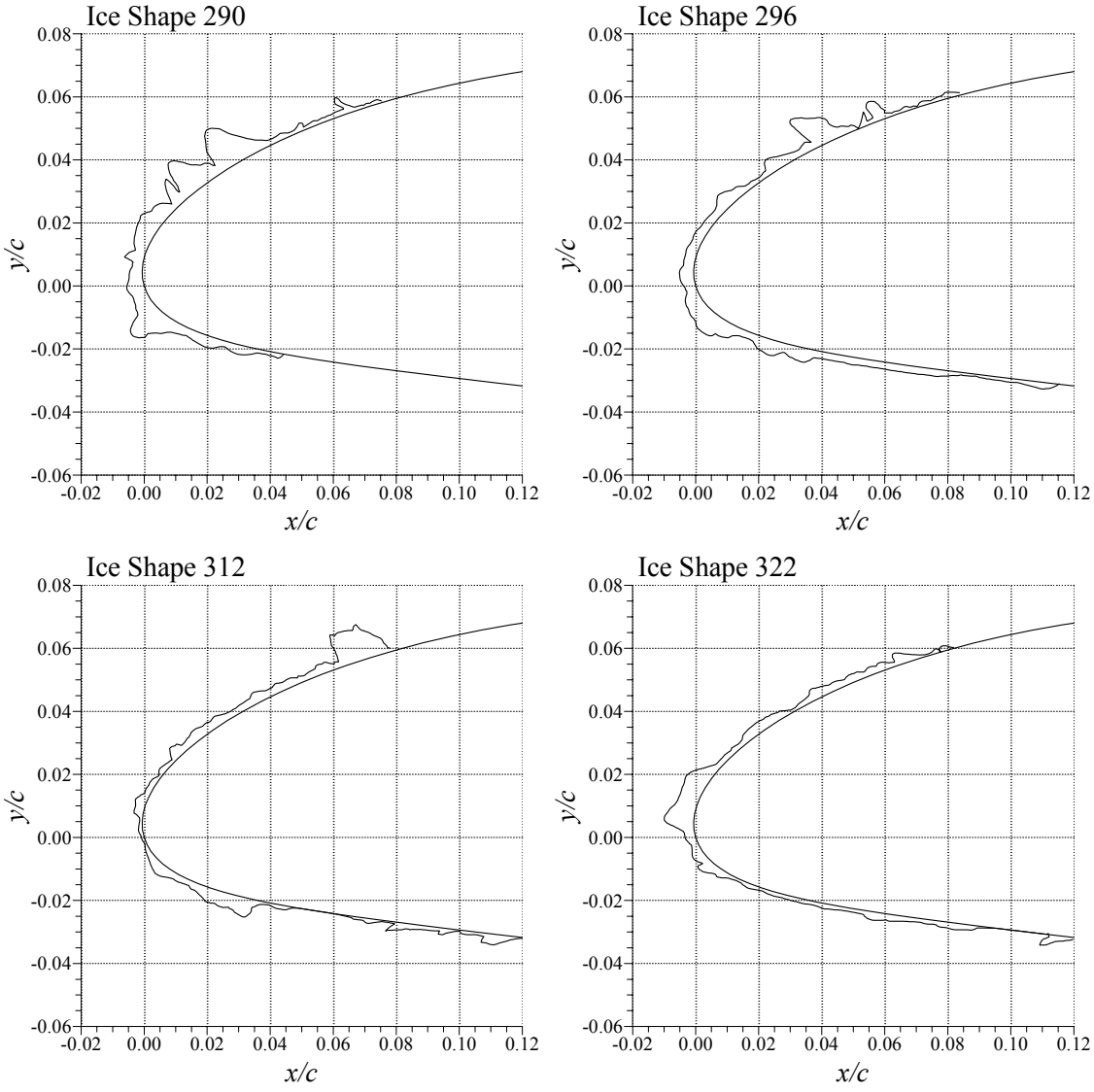

FIGURE 9. TRACINGS OF INTERCYCLE ICE ACCRETIONS ON NACA 23012 MODEL

The following procedure for constructing an intercycle ice simulation was used. The total surface extent of the accretion was determined from the ice shape tracing. Double-sided tape was laid out on a flat surface to a width equal to the determined surface extent. The roughness heights of the ice accretion was determined from the tracing. The appropriately sized grit roughness was selected and applied to the tape in the appropriate location. Particular attention was given to ridge-like features. The k/c and x/c values for these features were preserved as accurately as possible in the simulation. In many cases these ridges had to be built-up with layers of roughness. This was accomplished by applying a common spray-on adhesive to each layer. In fact, the entire area was coated with spray adhesive to help hold the roughness in place. The photographs of the actual ice castings were useful for determining the amount of spanwise variation to incorporate into the simulations. When this process was complete, the entire strip of roughness was lifted off the flat surface and wrapped around the leading edge of the airfoil model. A portion of the simulation was cut away around the pressure taps in the model. This allowed for approximate measurement of the pressure distribution over the ice shape simulation. The simulations were not durable enough to be reused for each of the three airfoils, so they were built-up separately for each airfoil test. This may have introduced some variation in the simulations from airfoil to airfoil. A typical completed simulation, as installed on a model is shown in figure 10.

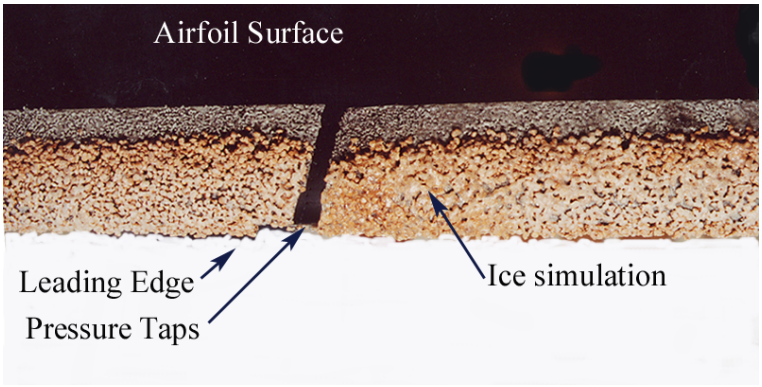

FIGURE 10. BUILT-UP ROUGHNESS METHOD FOR SIMULATING AN INTERCYCLE ICE SHAPE ON LSWT MODELS

In addition to the intercycle ice simulations, the airfoil models were also tested with standard roughness in the form of 80- and 150-grit, paper-backed garnet sandpaper. The purpose in testing these simulations was to provide a repeatable form of simulated ice roughness that could be identically duplicated on each of the airfoil models. As shown in table 1, these grit sizes approximately represent the chord length-scaled equivalent of the 40- and 80-grit sizes that were tested on the LTPT model [7 and 8]. The roughness heights listed in the table do not include the thickness of the paper backing that was approximately one and a half times as large as the roughness itself. Also, the sizes given in table 1 do not include the 0.003-inch-thick, double-sided tape used to attach the sandpaper to the model. The surface extent of the sandpaper roughness was $x/c = 0.10$ on the lower surface to $x/c = 0.07$ on the upper surface and was cut out around the pressure orifices. This is illustrated in figure 11.

TABLE 1. COMPARISON OF SANDPAPER ROUGHNESS HEIGHTS

Sandpaper Grit No.	Roughness Height (k, inches)*	Normalized Height (k/c) for c = 36 inches	Normalized Height (k/c) for c = 18 inches
40	0.0205	0.00057	0.00114
80	0.0083	0.00023	0.00046
150	0.0041	0.00011	0.00023

*Based upon nominal size of commercial carborundum [12].

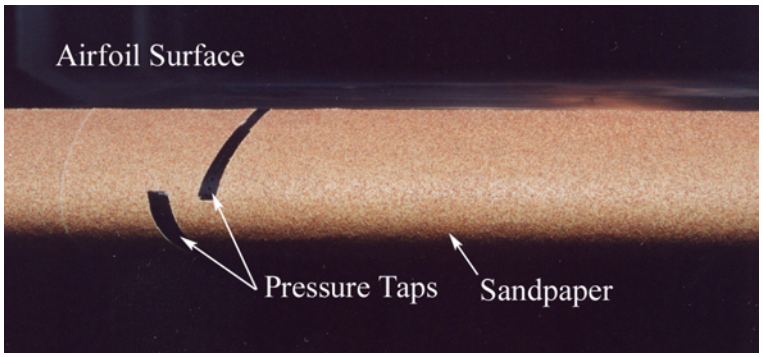

FIGURE 11. SANDPAPER ROUGHNESS APPLIED TO LSWT MODELS

3.3.3 Glaze Horn-Type Ice Simulations.

The simulated glaze horn-type ice accretions were determined from averaging geometry data from a set of actual ice accretions collected in a test at the NASA Glenn Icing Research Tunnel [19], for icing conditions see 14 CFR Part 25 Appendix C. Leading-edge glaze ice accretions characteristically consist of an upper and lower surface horn. However, only single-horn simulations were used for this research. A 3 by 3 matrix of ice shape size and radius was designed to parametrically vary these parameters and is shown in figure 12. The three sizes were k = 0.36, 0.78, and 1.20 inches, corresponding to k/c = 0.0020, 0.0433, and 0.0667, respectively. The base width of the shape was 52% of the height. Figure 12 also shows that the radius was varied from the zero radius (r/w = 0.00), or sharp, case to the full radius (r/w = 0.50). Each of these shapes could be positioned at six locations around the leading edge of each airfoil. Figure 13 shows the surface locations (s/c) and angles for all three airfoils tested in the LSWT. The intent here was to preserve the s/c locations among the airfoils. This resulted in different angles owing to the differences in the airfoil contour. Since the centerline of each shape was oriented perpendicular to the local surface contour, the shapes formed different angles with the chord line for each airfoil. For the NACA 23012 and the NACA 3415 airfoil, the s/c location given is referenced to the forward most point on the airfoil. This is different from the leading edge, as defined by x = 0.0, y = 0.0. Since these are NACA airfoils with camber, the forward most point on the airfoil has a small negative x coordinate and small positive y coordinate. In this way, the geometric ice shapes located at s/c = 0.0 would have a 0° angle with the chord.

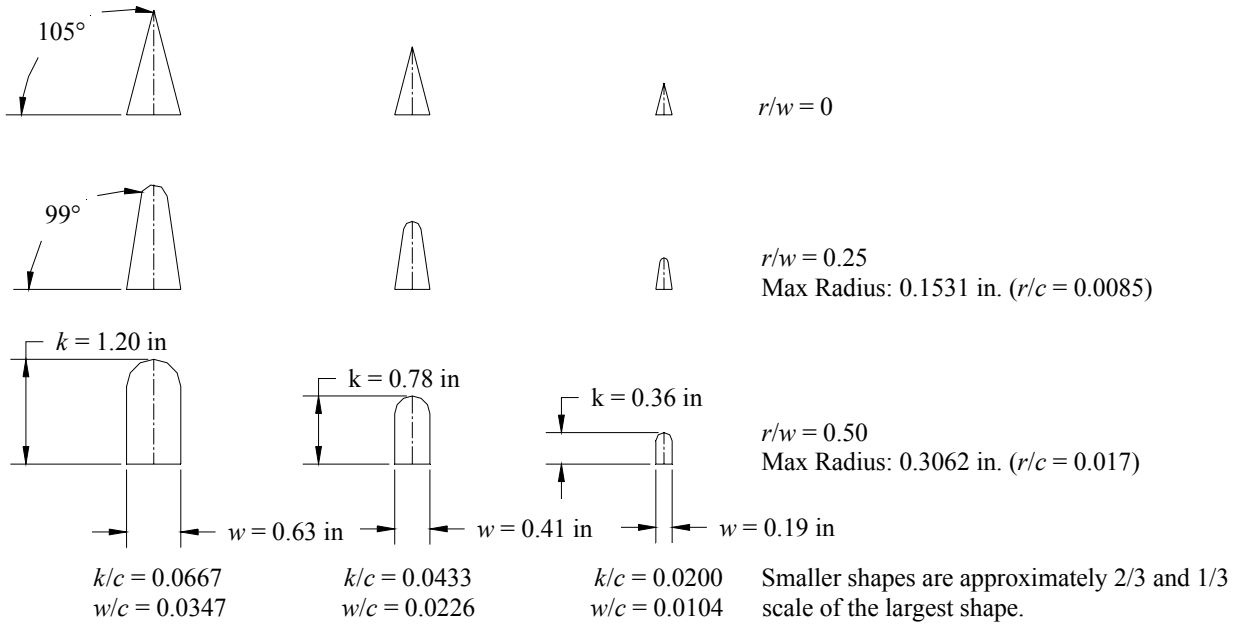

FIGURE 12. GLAZE HORN ICE SIMULATIONS TESTED AT LSWT

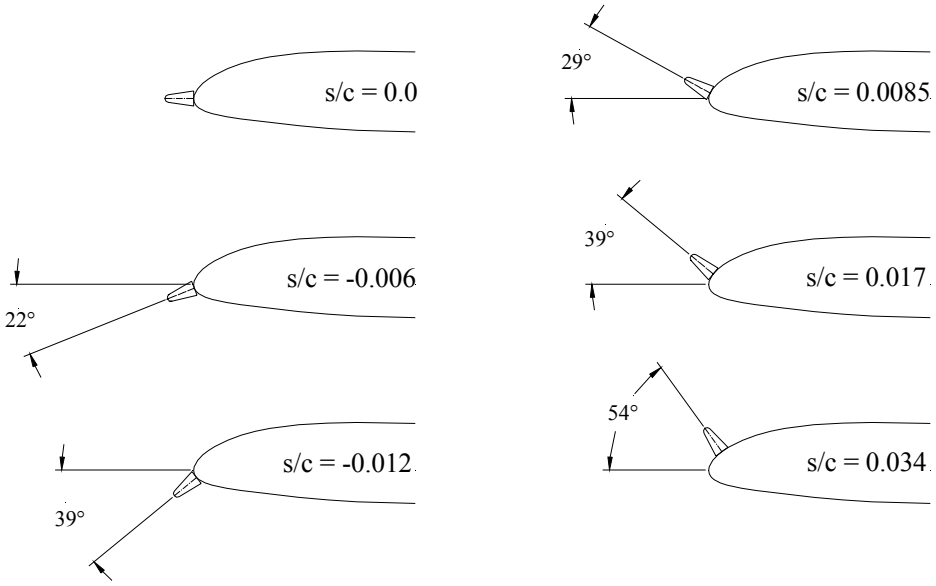

(a) NACA 23012

FIGURE 13. SURFACE LOCATIONS AND HORN ANGLES FOR GLAZE HORN ICE SIMULATIONS TESTED AT LSWT

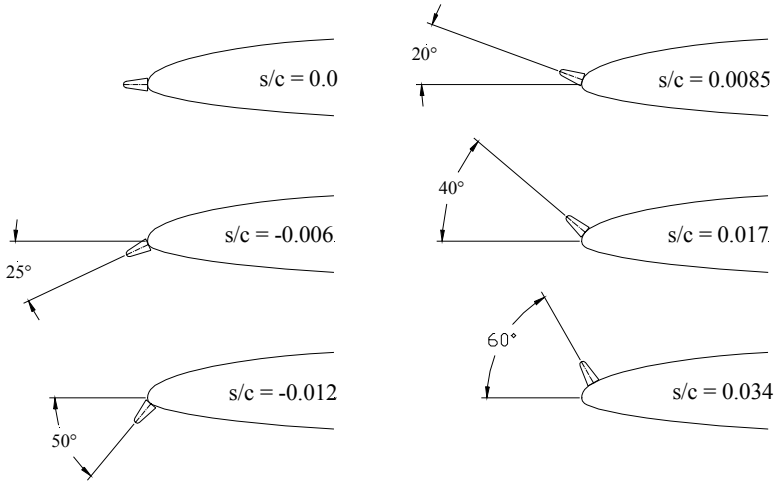

(b) NLF 0414

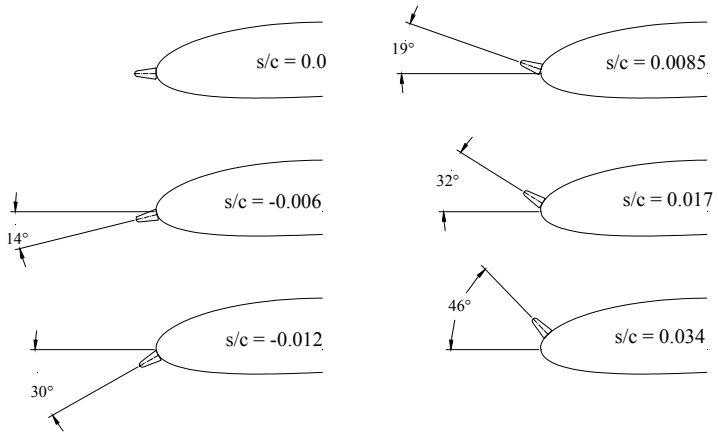

(c) NACA 3415

FIGURE 13. SURFACE LOCATIONS AND HORN ANGLES FOR GLAZE HORN ICE SIMULATIONS TESTED AT LSWT (Continued)

For tests in the LSWT, the geometric shapes were attached to the model using mounting brackets at the ends of the model. Tape was also placed over the simulation to prevent airflow between the base of the shape and the airfoil surface. For the LTPT model, the geometric shapes were bolted to the model along the span, similar to the quarter-round mounting. Likewise, the geometric shapes were also covered with aluminum tape. Also, the geometry of the shapes was scaled by the chord length to preserve the normalized height, radius, base width, and location on the leading edge.

3.4 TEST MATRICES.

This section describes, in general terms, the test matrices for all the different ice shape classifications and airfoils tested in this investigation for both the Illinois LSWT and NASA Langley LTPT. Experiments performed and reported from previous studies are not repeated here.

3.4.1 Low-Speed Wind Tunnel Test Matrices.

The NACA 23012 and the NACA 3415 were both tested in the clean configuration and with boundary layer trips to establish the baseline performance. In this report, the iced airfoil results are compared to the clean performance. The airfoils were tested with boundary layer trips to facilitate comparison with computational results or results from other facilities. This testing was carried out at two different aerodynamic conditions: (1) $Re = 1.0\times10^6$, $Ma = 0.10$ and (2) $Re = 1.8\times10^6$, $Ma = 0.18$. The angle of attack range was generally from negative stall to positive stall, taken in 1-degree increments. The boundary layer trips were similar to those used with the quarter-round shapes, as described in section 3.3.1. For the NACA 3415 airfoil, all of these cases were run at each of five flap settings: -10°, -5°, 0°, 5°, and 10°. Note that the standard sign convention applies: a positive flap deflection is trailing edge down.

The quarter-round shapes were tested on the NACA 3415 airfoil over several different chordwise locations. The majority of runs were performed using the $k/c = 0.0139$ quarter-round (with boundary layer trips) at $Re = 1.8\times10^6$, $Ma = 0.18$. A run was done for each of the five flap deflections. A subset of this matrix was carried out using the smaller, $k/c = 0.0056$ quarter round. A limited number of cases were also run at the lower speed: $Re = 1.0\times10^6$, $Ma = 0.10$. The $k/c = 0.0139$ quarter round (with trips) was tested on the NACA 23012 airfoil model at $x/c =$ 0.02, 0.10, and 0.20 for both $Re = 1.8\times10^6$, $Ma = 0.18$ and $Re = 1.0\times10^6$, $Ma = 0.10$. These tests generated data for comparison to equivalent data on NACA 23012m airfoil and the LTPT NACA 23012 airfoil model. The general angle of attack range was from -6° to stall, in 1-degree increments.

The four intercycle ice roughness simulations, as well as the 80- and 150-grit sandpaper, were tested on the NACA 23012, NACA 3415, and NLF 0414 airfoils. Both Reynolds number and Mach number combinations were tested. The standard five flap deflections (-10°, -5°, 0°, 5°, and 10°) were used for the NACA 3415 and NLF 0414 airfoils. The general angle of attack range was from -6° to stall, in 1-degree increments.

A subset of the geometric ice shapes was tested on the NACA 23012 and the NACA 3415 airfoils. All three sizes of the $r/w = 0.25$ radius shapes were tested along with the $k/c = 0.0433$ shapes with the $r/w = 0.00$ and 0.50 radii. Each of these shapes were tested at all six leading edge locations on each airfoil. Both Reynolds number and Mach number combinations were used. The flap deflections tested on the NACA 3415 were -5°, 0°, and 5°. The general angle of attack range was from -6° to stall, in 1-degree increments.

3.4.2 Low-Turbulence Pressure Tunnel Test Matrices.

The strength of the LTPT as a research facility lies in the ability to independently control the Reynolds number and Mach numbers. Therefore, more emphasis was placed on testing at many different aerodynamic conditions than on testing many different ice shape configurations. A total of eight Reynolds and Mach number combinations were used for the clean and iced configurations. These are summarized in table 2. Runs were performed at $Re = 2.0\times10^6$ to compare with data from the LSWT. Note that the two Mach numbers for this case, 0.10 and 0.21, closely match the Mach numbers from the LSWT (0.10 and 0.18). No sidewall venting

was available for runs performed at $Re = 2.0\times10^6$, however, the effect of sidewall venting was found to be small [7]. The remainder of the matrix was designed to isolate the effects of Reynolds number from Mach number. There is a Reynolds number variation from 3.5×10^6 to 10.5×10^6 at a constant Mach number of 0.12. Likewise, there is a Mach number variation from 0.12 to 0.28 at a constant Reynolds number of 7.5×10^6. Data were collected over an angle of attack range of -6° to stall, except for drag, which was collected in 2-degree increments in the linear-lift range.

A subset of all three ice shape classifications was tested at the LTPT on the 36-inch chord NACA 23012 airfoil model. The intercycle ice shape castings and sandpaper cases are described in references 7 and 8. The $k/c = 0.0139$ quarter-round shape was tested at x/c locations of 0.02, 0.10, and 0.20. The $k/c = 0.0020$ and 0.0433 geometric ice simulations were also run. Each of these had a nondimensional tip radius (r/w) of 0.25 and were located at $s/c = 0.000$ and 0.034.

TABLE 2. TEST MATRIX FOR LTPT AERODYNAMIC CONDITIONS

Reynolds Number	Mach Number			
	0.10	0.12	0.21	0.28
2.0×10^6	X		X	
3.5×10^6		X		
7.5×10^6		X	X	X
10.5×10^6		X		X

4. RESULTS AND DISCUSSION.

This sections presents and discusses the key results of this investigation. The body of previous work is incorporated into these results so that the full story of ice shape classifications and airfoil characteristics may be told. This section is organized by ice shape classification. The clean airfoil results are presented first. The effect of SLD ridge-type ice simulations on the three airfoils is discussed, followed by the effects of intercycle ice simulations, and glaze horn-type ice simulations.

4.1 CLEAN AIRFOIL DATA.

4.1.1 Comparison of Performance Data for the Three Airfoils Tested.

Figure 14 compares the geometry of the three airfoils tested. The NACA 3415 was the thickest airfoil tested, followed by the NLF 0414. The NACA 23012 was the thinnest airfoil. The NACA 3415 and the NLF 0414 were highly cambered, while the NACA 23012 was not.

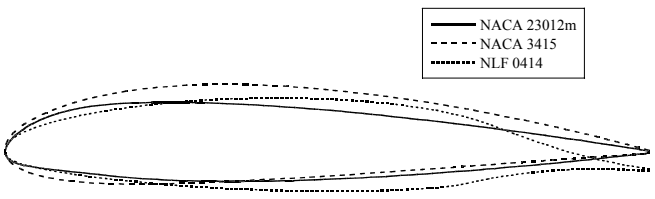

FIGURE 14. GEOMETRIES OF THE THREE AIRFOILS TESTED AT LSWT

The clean airfoil-integrated aerodynamic coefficient comparisons are shown in figure 15. The results were from the Illinois LSWT at $Re = 1.8\times10^6$ and $Ma = 0.18$. The NACA 23012m had the highest $C_{l,max}$ of the three airfoils tested (1.50). The NACA 3415 and the NLF 0414 had very similar $C_{l,max}$ of 1.35 and 1.34, respectively. The NACA 23012m had a leading-edge stall, indicated by a sudden loss in lift at stall [20]. The NACA 3415 and the NLF 0414 had a more gradual stall typical of trailing-edge stall.

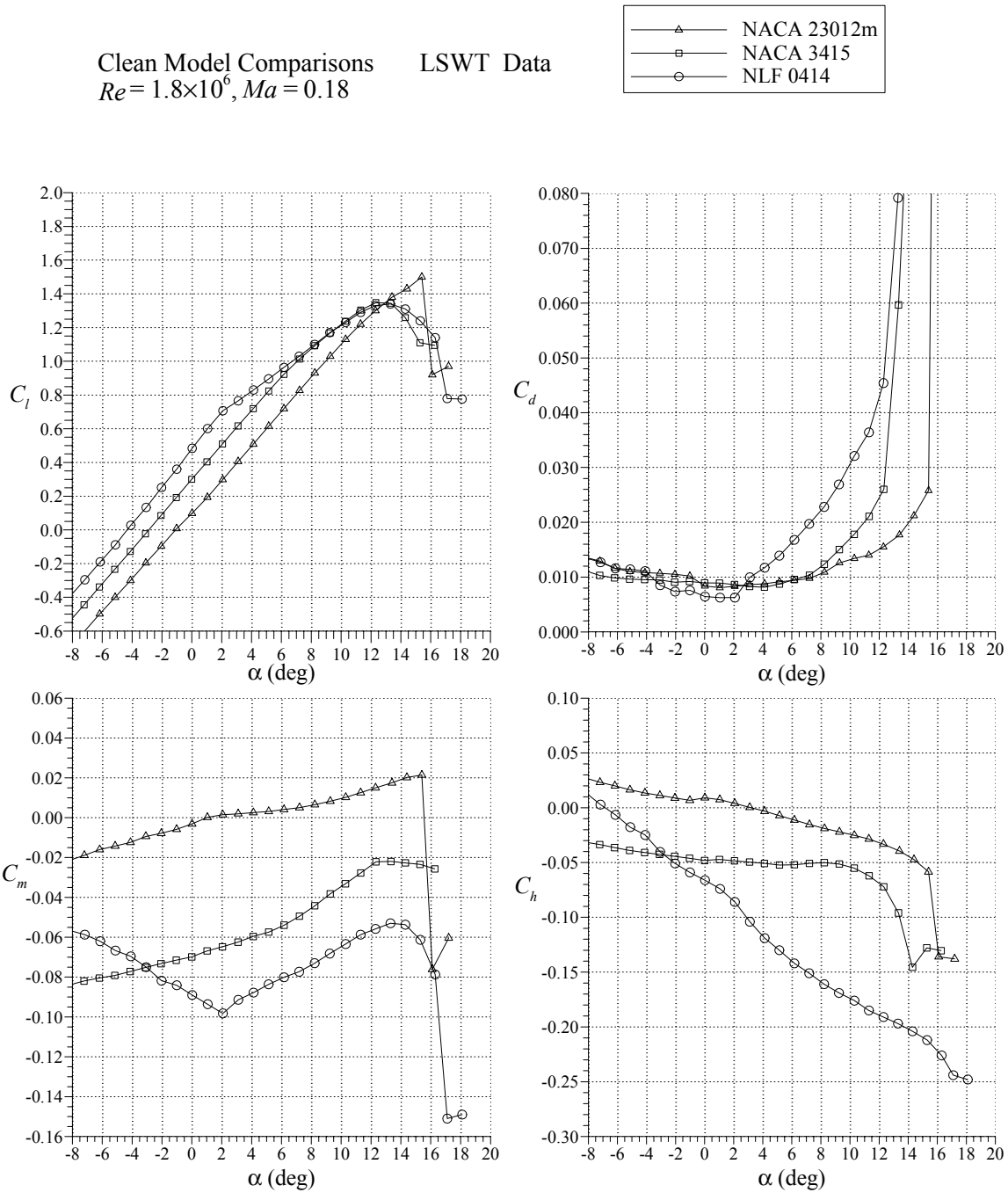

FIGURE 15. CLEAN AIRFOIL DATA FOR THE THREE AIRFOILS TESTED AT LSWT

The NLF 0414 had the lowest drag for $-3° < \alpha < 3°$, since it was a laminar flow airfoil. However, at angles of attack outside of this range, there was significant flow separation near the trailing edge, which resulted in higher drag than the two NACA airfoils. The NACA 23012m and the NACA 3415 had nearly identical drag for $0° < \alpha < 7°$. At $\alpha < 0°$, NACA 23012m had higher drag, and for $\alpha > 7°$, the NACA 3415 had higher drag.

The NLF 0414 had the most negative C_m values, followed by the NACA 3415 and the NACA 23012m. This indicated that the NLF 0414 had the largest amount of positive camber, followed by the NACA 3415 and the NACA 23012m. The flap hinge moment results show that on the NACA 23012m, there was a sudden break in the C_h when the airfoil stalled. This is typical of a leading-edge stall where the flow over the flap is suddenly separated. The break in C_h for the NACA 3415 was much more gradual. This is typical of a trailing-edge stall because the separation first forms at the trailing edge and slowly moves upstream with increasing angle of attack. The magnitude of C_h was large at nearly all angles of attack for the NLF 0414. This was due to the flow over the flap being separated at nearly all angles of attack. The large differences in pressures between the stalled surface and unstalled opposite surface led to the large values in C_h.

Figure 16 shows the clean model pressure distribution comparison at a nominal lift coefficient of 0.5. Because of varying degrees of camber, each model was at a different angle of attack. The NACA 23012m has a very large suction peak (with $C_{p,min} = -1.4$) centered near $x/c = 0.08$. There was a severe pressure recovery (with very adverse pressure gradient) from $x/c = 0.08$ to 0.22. The pressure recovery became more gradual downstream of this location and extended to the trailing edge.

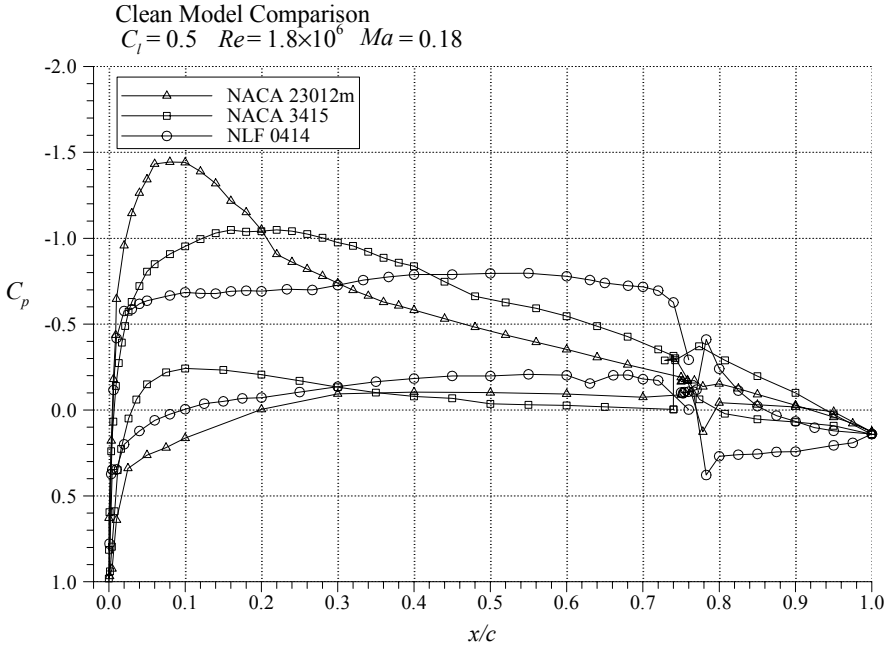

FIGURE 16. CLEAN AIRFOIL SURFACE PRESSURE DISTRIBUTIONS FOR THE THREE AIRFOILS TESTED AT LSWT

The NACA 3415 had a pressure distribution that was quite different. A large suction peak was not present on this airfoil at this angle of attack, with a $C_{p,min}$ value of only -1.05 located near x/c = 0.20. Because a large suction peak was not present, the pressure recovery was very gradual, with a nearly constant pressure gradient extending from x/c = 0.25 to the trailing edge. The NLF 0414 had a nearly constant C_p between x/c = 0.04 to 0.72 on the upper surface. The pressure recovery did not start until x/c = 0.72. Because of the short recovery region, the adverse pressure gradient in this region was the most severe of the three airfoils tested and was the reason why the flow was separated over the flap at nearly all angles of attack.

4.1.2 NACA 3415 Airfoil Performance Details.

Since the NACA 23012m and the NLF 0414 airfoils were used extensively in previous work, the detailed clean performance data were reported in other sources [1 and 18] and will not be repeated here. However, the NACA 3415 airfoil was built specifically for this investigation, and this section provides more detailed performance data.

The clean baseline measurements taken on the NACA 3415 model were compared to previously published data [21] and XFOIL [22] numerical results to validate the airfoil model geometry, experimental apparatus, and data acquisition/reduction methods. Figure 17 shows the comparisons in the integrated coefficients among the LSWT data, XFOIL, and airfoil data from Abbott and von Doenhoff [21]. Previously published data for the NACA 3415 were not available for comparisons. The two closest airfoils with previously published data were the NACA 2415 and the NACA 4415. The aerodynamic characteristics of NACA 3415 should fall in between these two airfoils, and figure 17 shows that they do (at least for lift and pitching moment). The Reynolds number and the Mach number for the LWST data and XFOIL simulations were 1.8×10^6 and 0.18, respectively. The Reynolds number and Mach number for the NACA 2415 and the NACA 4415 data were 3.0×10^6 and 0.17 (or less).

Figure 17 shows that the lift curves from the pressure and the balance data (for the NACA 3415) were nearly identical until 2° past stall, where the balance data exhibited higher values. The NACA 3415 lift curve fit roughly between the NACA 2415 and the NACA 4415, with similar lift curve slopes in the linear regions. The $C_{l,max}$ was about 0.05 lower than the NACA 2415 and the NACA 4415, but this was likely due to the lower Reynolds number for the LSWT data. The XFOIL results showed much higher lift curve slope and $C_{l,max}$. However, this is typical for a thick airfoil such as the NACA 3415 with trailing-edge separation prior to stall since XFOIL does not simulate separated regions accurately, in the authors' experience. The drag comparisons showed that the LSWT NACA 3415 had higher C_d values than XFOIL, NACA 2415, and NACA 4415 for $C_l < 0.80$. This was likely due to a combination of flap gap discontinuity (flap gap was not modeled in the XFOIL simulation) and lower Reynolds number (when compared to the NACA 2415 and the NACA 3415 data). The pitching moment results showed that the LSWT NACA 3415 data again fell in between the NACA 2415 and the NACA 4415. The flap hinge moment data were not present for the NACA 2415 and the NACA 4415. Also, XFOIL does not accurately predict the flap hinge moment coefficients. Because of this, only the pressure and balance data for the NACA 3415 from LSWT are presented. Again, the pressure and balance data show good agreement.

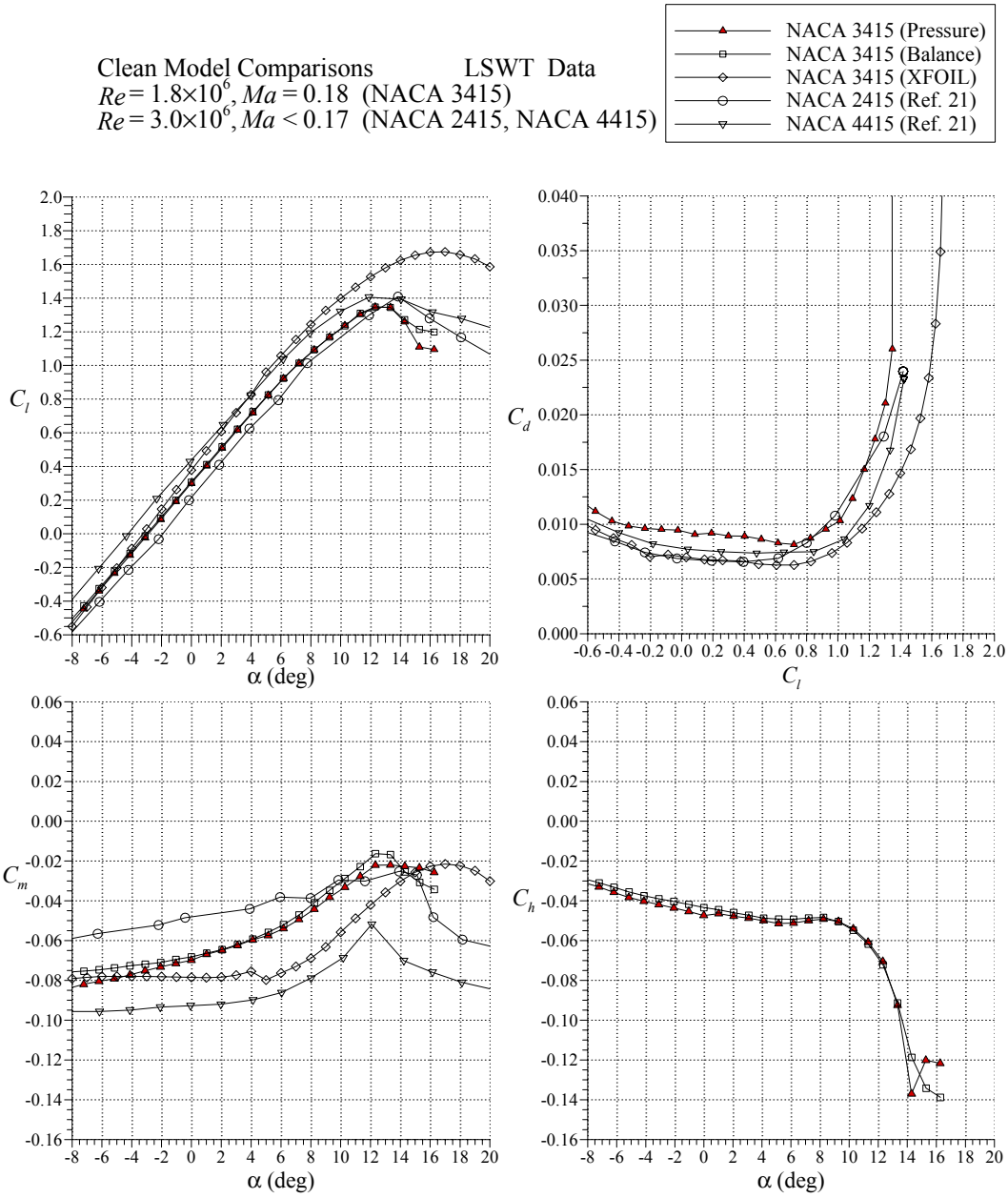

FIGURE 17. COMPARISON OF LSWT NACA 3415 CLEAN AIRFOIL DATA WITH XFOIL RESULTS AND HISTORICAL DATA

The surface pressure distribution on the NACA 3415 from the LSWT data were compared to the XFOIL simulation results. Because the LSWT data and XFOIL results showed different lift values at the same angles of attack, the comparison was made at matched lift coefficients. Figure 18(a) shows the surface pressure comparisons at $C_l = 0.30$. This corresponded to $\alpha = 0°$ for LWST and $\alpha = -0.68°$ for the XFOIL. First, it is important to note the discontinuity in the pressure distribution at $x/c = 0.74$ in the LSWT data was due to the flap gap. The LSWT data and the XFOIL results showed reasonably good agreement. In the LSWT data, there was a small change in the pressure gradient at $x/c = 0.48$ due to a laminar separation bubble. In the XFOIL

results, this occurred at $x/c = 0.56$. Figure 18(b) shows the comparison at $C_l = 0.72$. Again, the comparisons were reasonable. The laminar bubble was located at $x/c = 0.38$ on the LSWT data and at $x/c = 0.44$ on the XFOIL results. Figure 18(c) shows the comparison at $C_l = 1.09$ with reasonable agreement. The LSWT data indicate the beginning of trailing-edge separation (nearly constant C_p at the trailing edge), while the XFOIL results do not. Figure 18(d) shows the comparison at $C_l = 1.3$ ($C_{l,max}$ for LSWT data). The comparison at this lift coefficient was not as good as at the lower lift values. For the LWST data, the flow was separated from $x/c = 0.74$ to the trailing edge, indicated by nearly constant C_p values in this region. For the XFOIL results, the flow separation occurred at $x/c = 0.96$. This showed that XFOIL did not accurately predict the trailing-edge flow separation and the stall process.

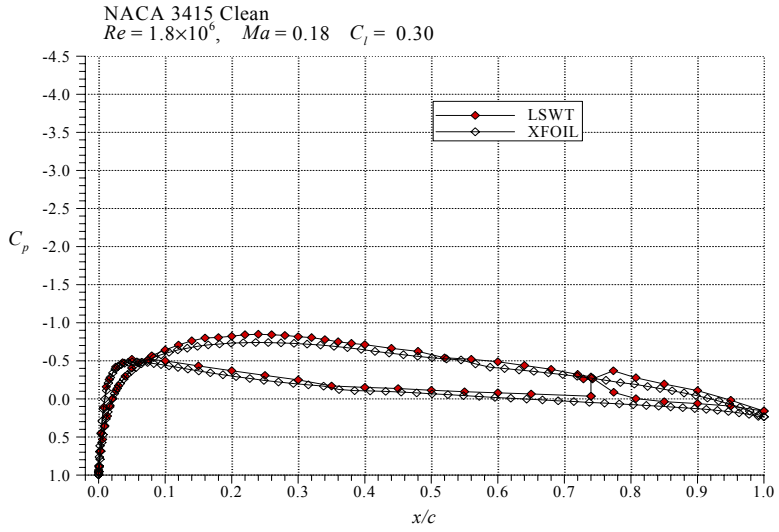

(a) $C_l = 0.30$

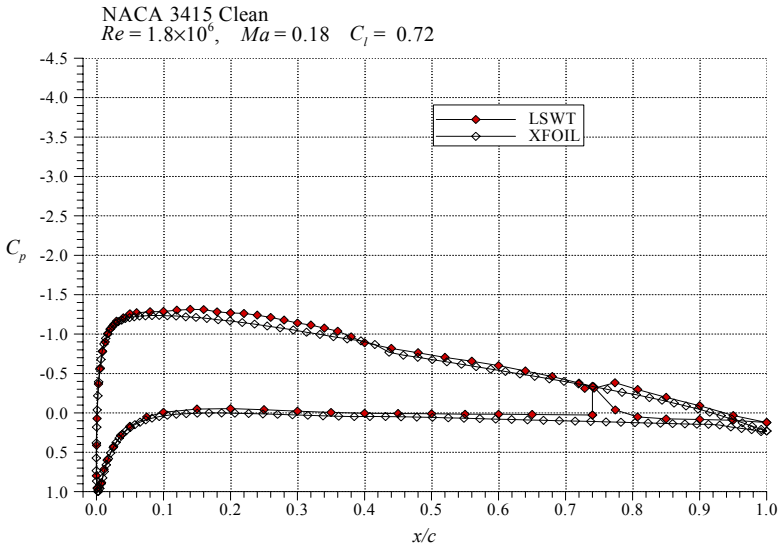

(b) $C_l = 0.72$

FIGURE 18. COMPARISON OF LSWT NACA 3415 CLEAN AIRFOIL PRESSURE DISTRIBUTION WITH XFOIL

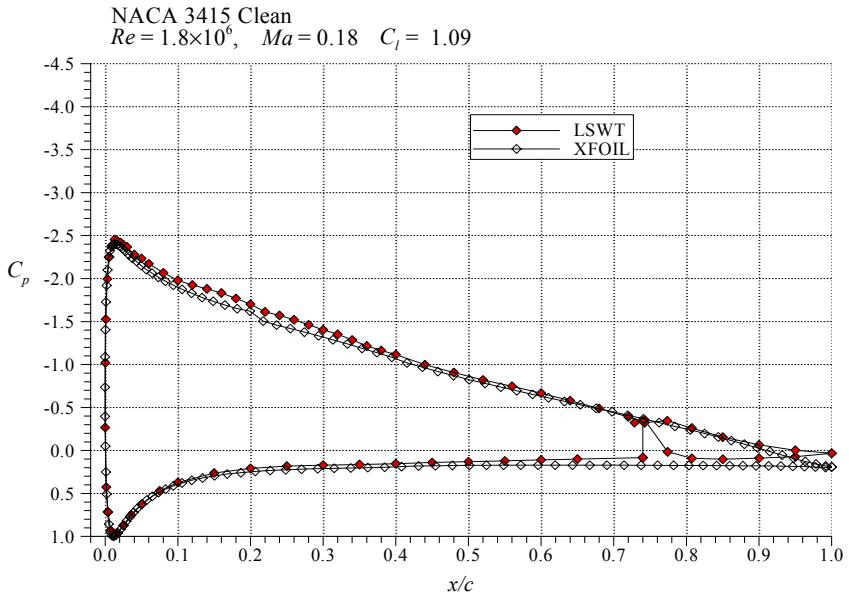

(c) $C_l = 1.09$

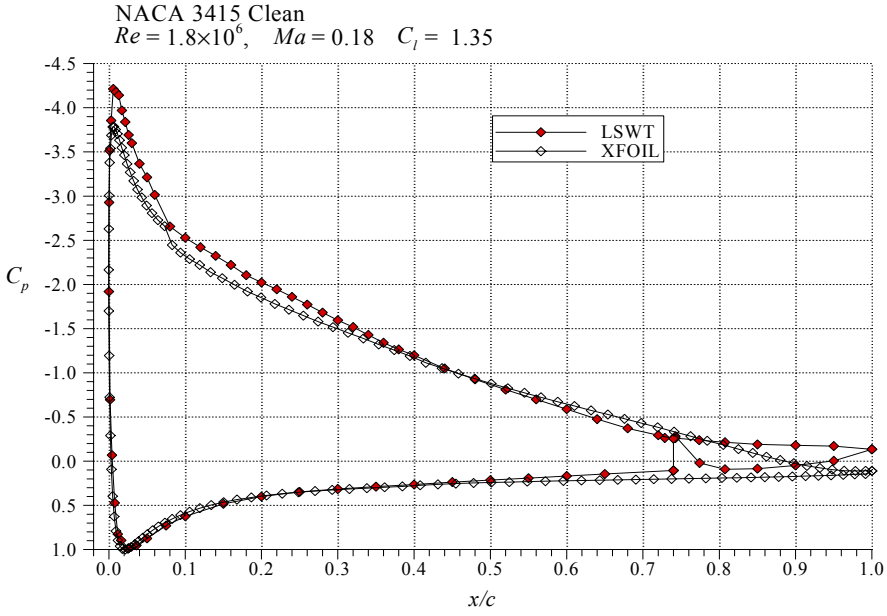

(d) $C_l = 1.35$

FIGURE 18. COMPARISON OF LSWT NACA 3415 CLEAN AIRFOIL PRESSURE DISTRIBUTION WITH XFOIL (Continued)

The comparison of clean NACA 3415 data from LSWT to those of NACA 2415 and NACA 4415 showed that NACA 3415 lift and pitching moment data fit in between the other two NACA airfoils, as expected. The pressure distribution data from LSWT only showed reasonable agreement with the XFOIL results. This may have been due to early trailing-edge separation on the LSWT model due to the flap gap discontinuity or XFOIL not modeling the trailing-edge separation properly.

4.1.3 Reynolds and Mach Numbers Effects.

The Reynolds and Mach numbers effects on the performance of the NACA 23012 airfoil were thoroughly documented in references 7 and 8. However, given that the clean airfoil baseline is important to understanding the effects of ice accretions, some of these results are repeated here. NACA 23012 performance data from the LTPT are also compared with data from the LSWT.

Overall, the clean airfoil results followed classic airfoil behavior and compared favorably with historical data and computational results. Figure 19 shows the effect of Reynolds number at constant Mach number on the performance coefficients. The maximum lift coefficient increased by approximately 0.10 from $Re = 3.5\times10^6$ to 7.5×10^6. Predictable results were also observed in the drag data, where the drag coefficients tended to decrease with increasing Reynolds number from $Re = 3.5\times10^6$ to 7.5×10^6. The effect of Mach number at constant Reynolds number is illustrated in figure 20. Again, classic airfoil behavior was observed in the performance coefficients. The lift curve slope $C_{l,\alpha}$ increased with Mach number, but $C_{l,max}$ decreased about 0.05 from $Ma = 0.12$ to $Ma = 0.28$. The stalling angle of attack was also reduced about 1 degree. The difference in stall parameters (not shown) was more pronounced at $Re = 10.5\times10^6$, where $C_{l,max}$ was reduced by 0.10 and α_{stall} was reduced by 2 degrees as the Mach number was increased from 0.12 to 0.28. Classic Mach number effects were observed in the drag and pitching moment data as well. There was a significant increase in drag at low angles of attack from $Ma = 0.12$ to 0.28. The increasing $C_{l,\alpha}$ noted above occurred along with an attendant increase in C_d. The variation in pitching moment indicates that the airfoil became more front-loaded for higher angles of attack as the Mach number increased. The clean airfoil data acquired at $Re = 10.5\times10^6$ showed no dependence on Mach number over the range that was tested. As illustrated in figure 21, there is very little difference in the performance coefficients for a greater than two-fold increase in Mach number. Conversely, the increase in Reynolds number caused the $C_{l,max}$ to increase about 0.20.

The Reynolds and Mach numbers effects were also consistent with previous airfoil tests conducted in the LTPT. For example, Ladson [23] analyzed data from previous experiments using a NACA 0012 airfoil, having a 24-inch chord. The independent effects of Reynolds and Mach numbers on $C_{l,max}$ were very similar to the present results. Furthermore, the present data also compared very favorably with historical data on the NACA 23012 airfoil from Abbott and von Doenhoff [21]. Detailed comparisons are presented in references 7 and 8.

The LTPT data were also compared to data acquired at the LSWT on the NACA 23012 airfoil. These data are plotted in figure 22 for closely matched Reynolds and Mach numbers. There is very good agreement in the lift data, except near $C_{l,max}$. This discrepancy is small and may even be attributable to the small difference in Reynolds number. The pitching moment data acquired in the LSWT were slightly more nonlinear than the LTPT data. Agreement in the drag values was good except at certain odd-numbered angles of attack (e.g., -1° and 5°). Comparison here was difficult because there were no wake survey drag data available in the LTPT data set for odd-numbered angles of attack. The drag coefficients from the LTPT experiments were slightly higher than the LSWT data for angles of attack in the range of 2° to 10°. It is possible that the spanwise-running seams (on both lower and upper surface) from the removable leading edge caused an artificial boundary layer transition, thus, resulting in higher drag for the LTPT model.

The effect of the removable leading-edge seams was also discussed in references 7 and 8 and was investigated computationally.

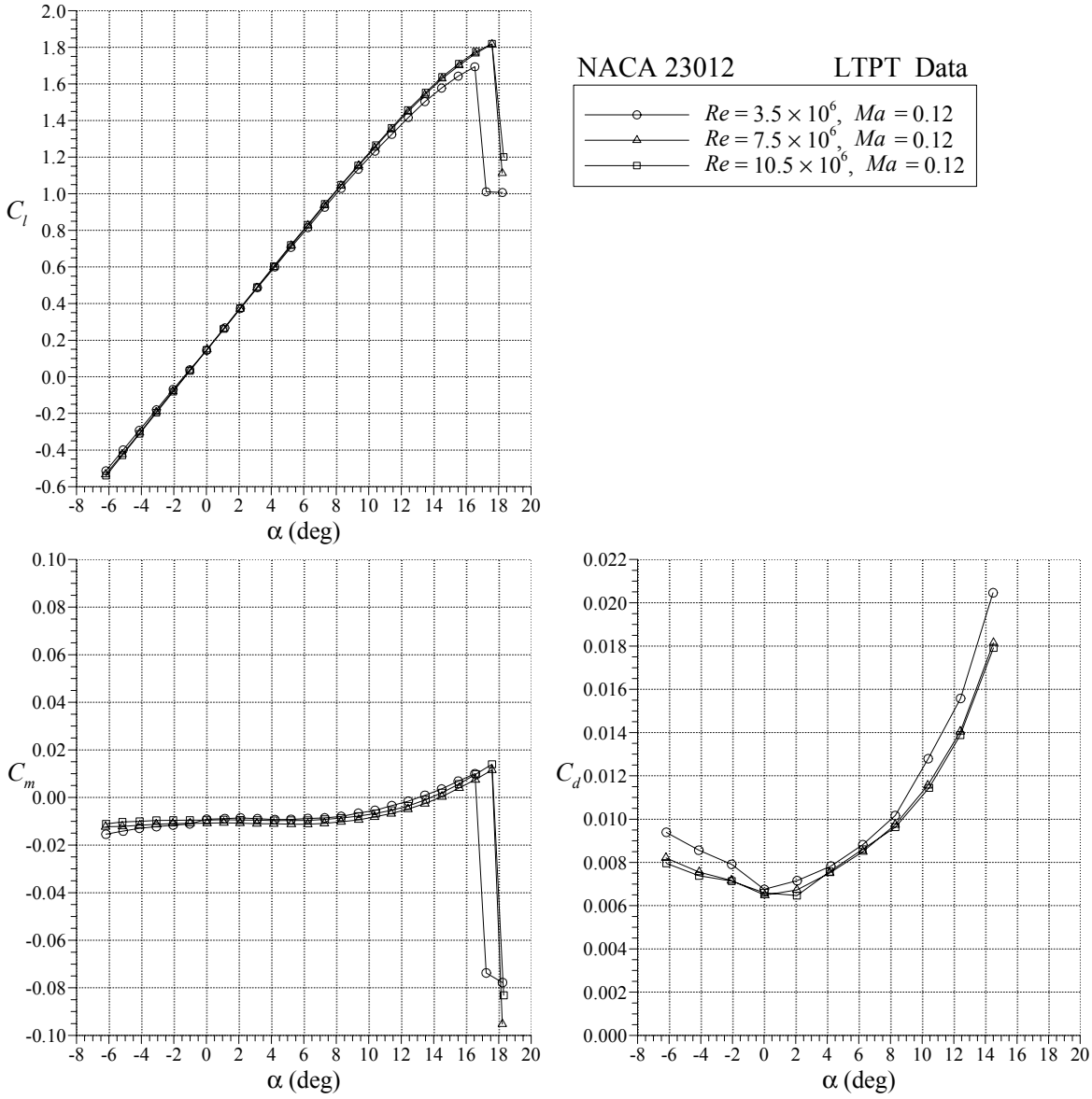

FIGURE 19. EFFECT OF REYNOLDS NUMBER ON CLEAN NACA 23012 AIRFOIL PERFORMANCE

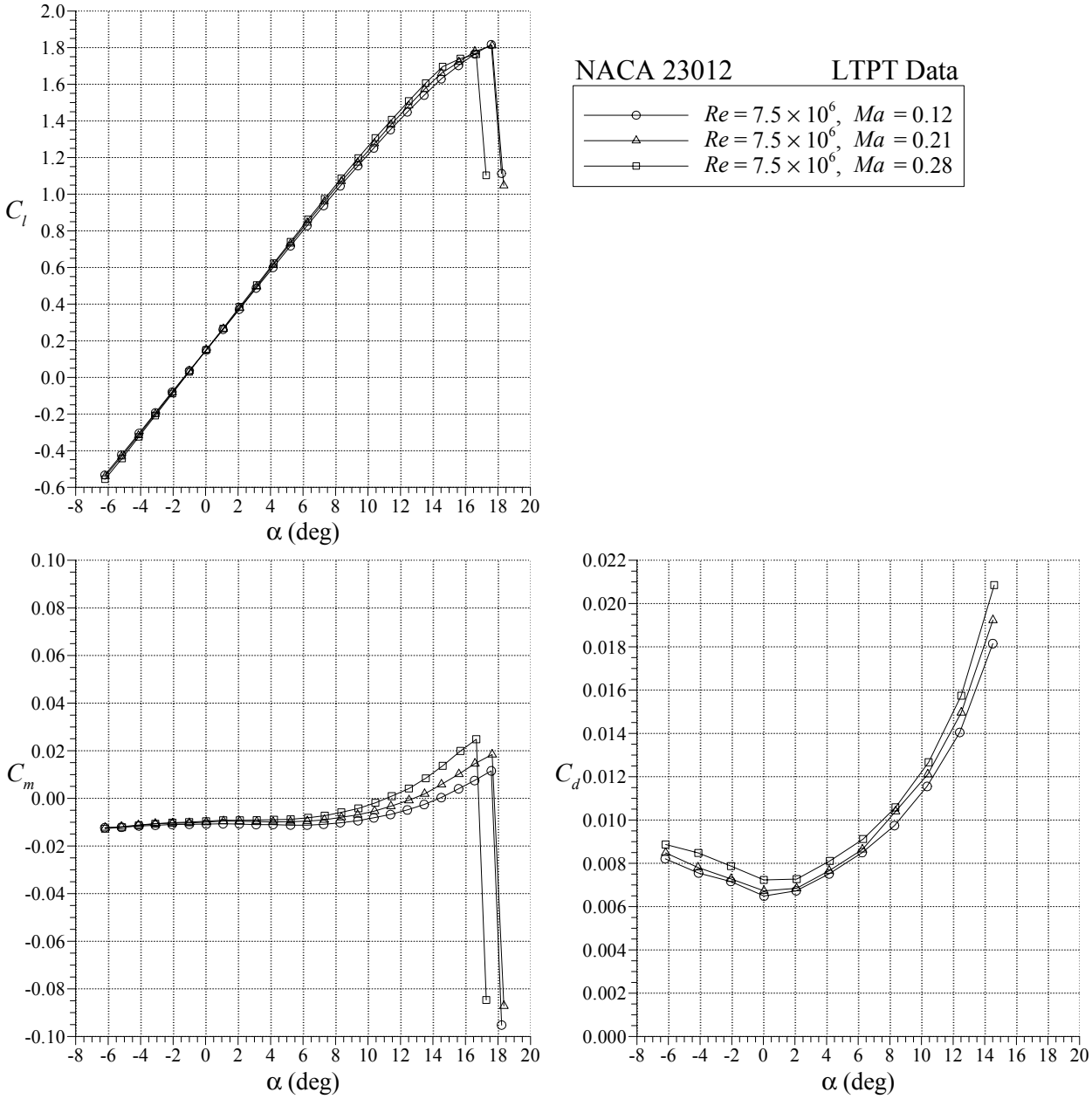

FIGURE 20. EFFECT OF MACH NUMBER CLEAN NACA 23012 AIRFOIL PERFORMANCE

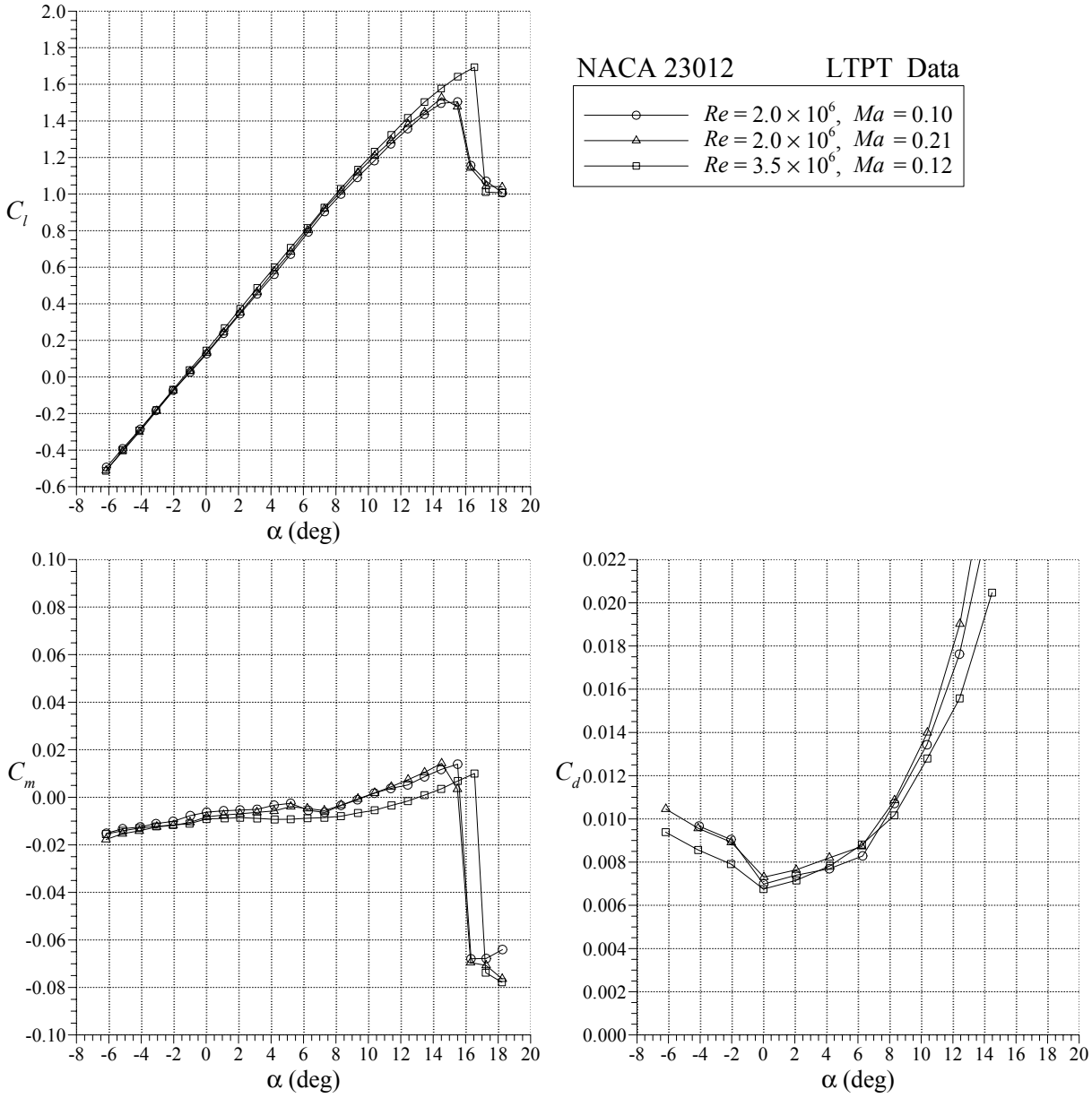

FIGURE 21. EFFECT OF REYNOLDS AND MACH NUMBERS ON CLEAN NACA 23012 AIRFOIL PERFORMANCE

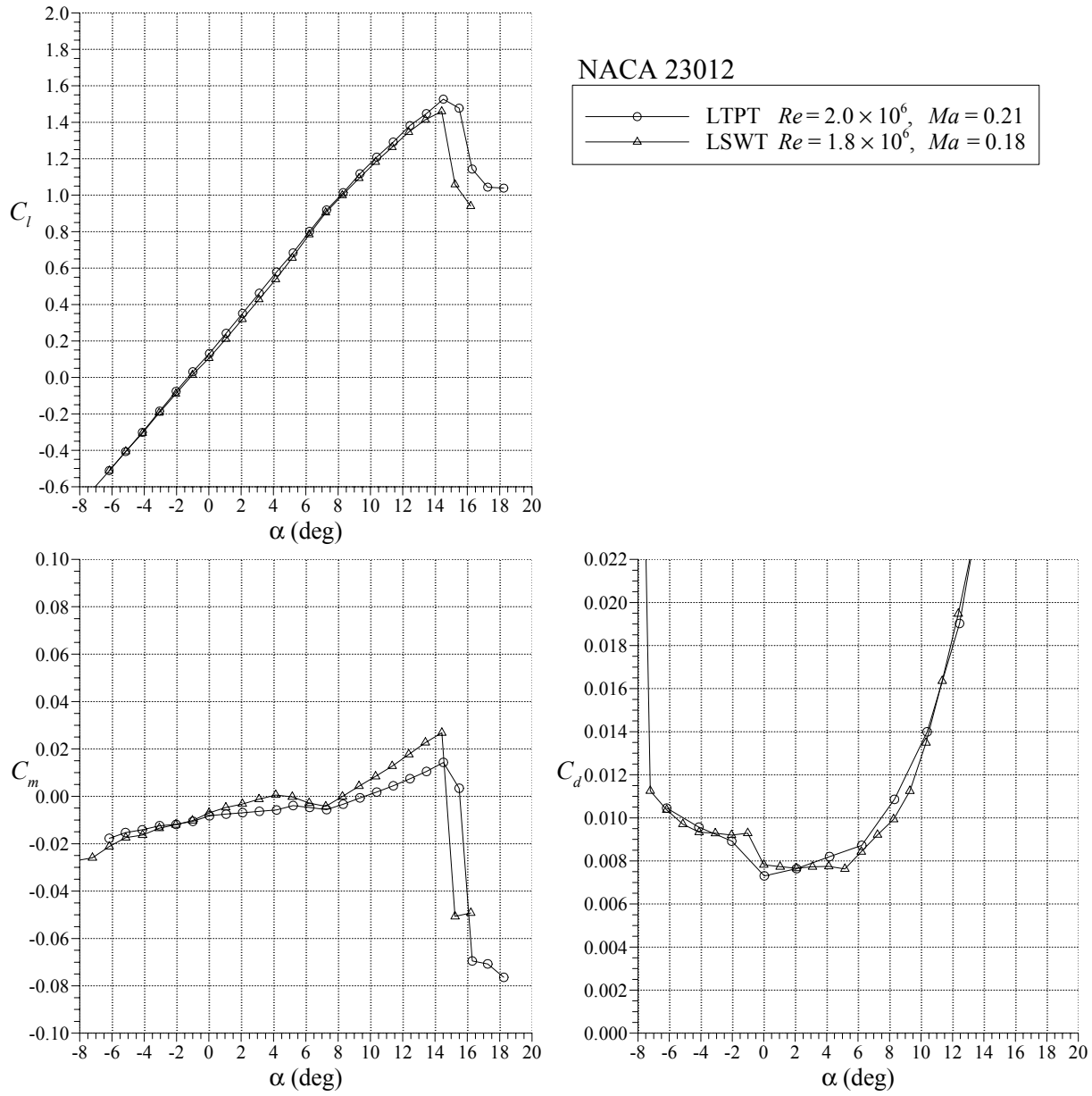

FIGURE 22. COMPARISON OF LTPT AND LSWT CLEAN NACA 23012 AIRFOIL DATA

The effects of Reynolds number on the maximum lift coefficient are summarized in figure 23 for the NACA 23012 airfoil. The data shown are for Mach numbers in the range of 0.10 to 0.12, except for the LSWT datum at $Re = 1.8 \times 10^6$. However, Mach number effects between 0.10 and 0.18 should be very small (cf. figure 21). The data illustrate the strong dependence of $C_{l,max}$ on Reynolds numbers between 1.0×10^6 and 3.5×10^6 for the clean NACA 23012. The plot also shows that the difference in $C_{l,max}$ between the LTPT and the LSWT could be attributable to the small difference in Reynolds numbers.

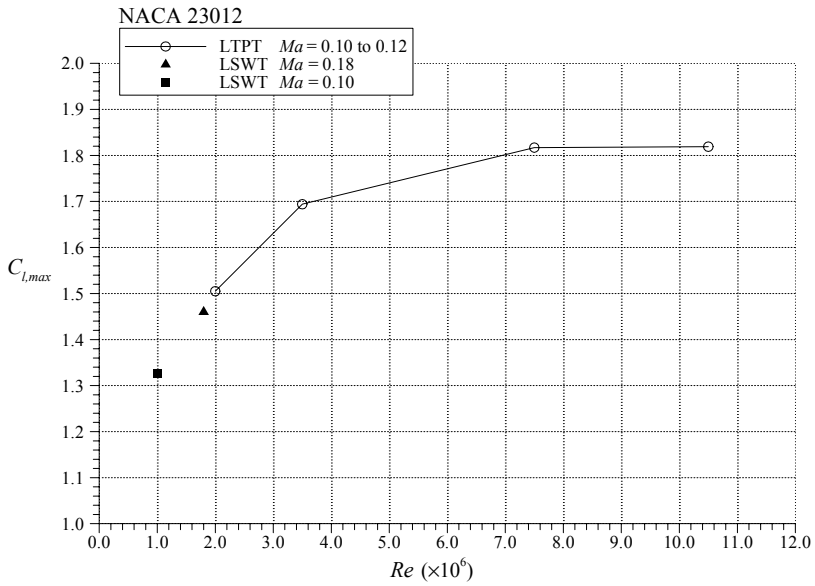

FIGURE 23. EFFECT OF REYNOLDS NUMBER ON THE CLEAN NACA 23012 AIRFOIL $C_{l,max}$

4.2 SUPERCOOLED LARGE DROPLET, RIDGE-TYPE ICE ACCRETIONS.

4.2.1 Airfoil Geometry Effects.

The forward-facing, quarter-round ice simulation was the standard SLD geometry used in previous work [1]. In that investigation, three heights were tested (k/c = 0.0056, 0.0083, and 0.0139) on the NACA 23012m, and one height (k/c = 0.0139) was tested on the NLF 0414. In this investigation, two heights (k/c = 0.0056 and 0.0139) were tested on the NACA 3415.

Figure 24 shows the integrated coefficients for the k/c = 0.0139 quarter round at various chordwise locations at $Re = 1.8\times10^6$ and Ma = 0.18. It shows that as the ice shape was moved downstream from the leading edge to x/c = 0.15, both the $C_{l,max}$ and α_{stall} decreased. When the ice shape was located between x/c = 0.20 and 0.30, there was little change in $C_{l,max}$, which remained nearly constant at 0.30. When the ice shape was located at x/c = 0.40 and 0.50, a $C_{l,max}$ in the traditional sense was not observed. Instead, there was simply an inflection in the lift curve when the flow downstream of the ice shape became fully separated. As the angle of attack was increased, the lift continued to increase. This was because lift was still being generated from the portion of the airfoil upstream of the ice shape that was still attached.

Figure 24 shows that the drag increased as the ice shape was moved downstream from the leading edge to x/c = 0.30. However, when the ice shape was located at x/c = 0.40, the drag at positive angles of attack decreased. This trend continued when the ice shape was located at x/c = 0.50. The pitching moment results showed that the angle of attack at which the negative break in C_m occurred (which coincided with the rapid bubble growth downstream of the ice shape) decreased as the ice shape was moved downstream from the leading edge to x/c = 0.30. When the ice shape was located at x/c = 0.40 and 0.50, a break in the C_m was not observed.

Similar results were observed for the flap hinge moments. For the hinge moments, the negative breaks were due to the separation bubble reaching the flap. As the ice shape was moved downstream from the leading edge to mid-chord, the angle of attack at which the break in the C_h occurred decreased.

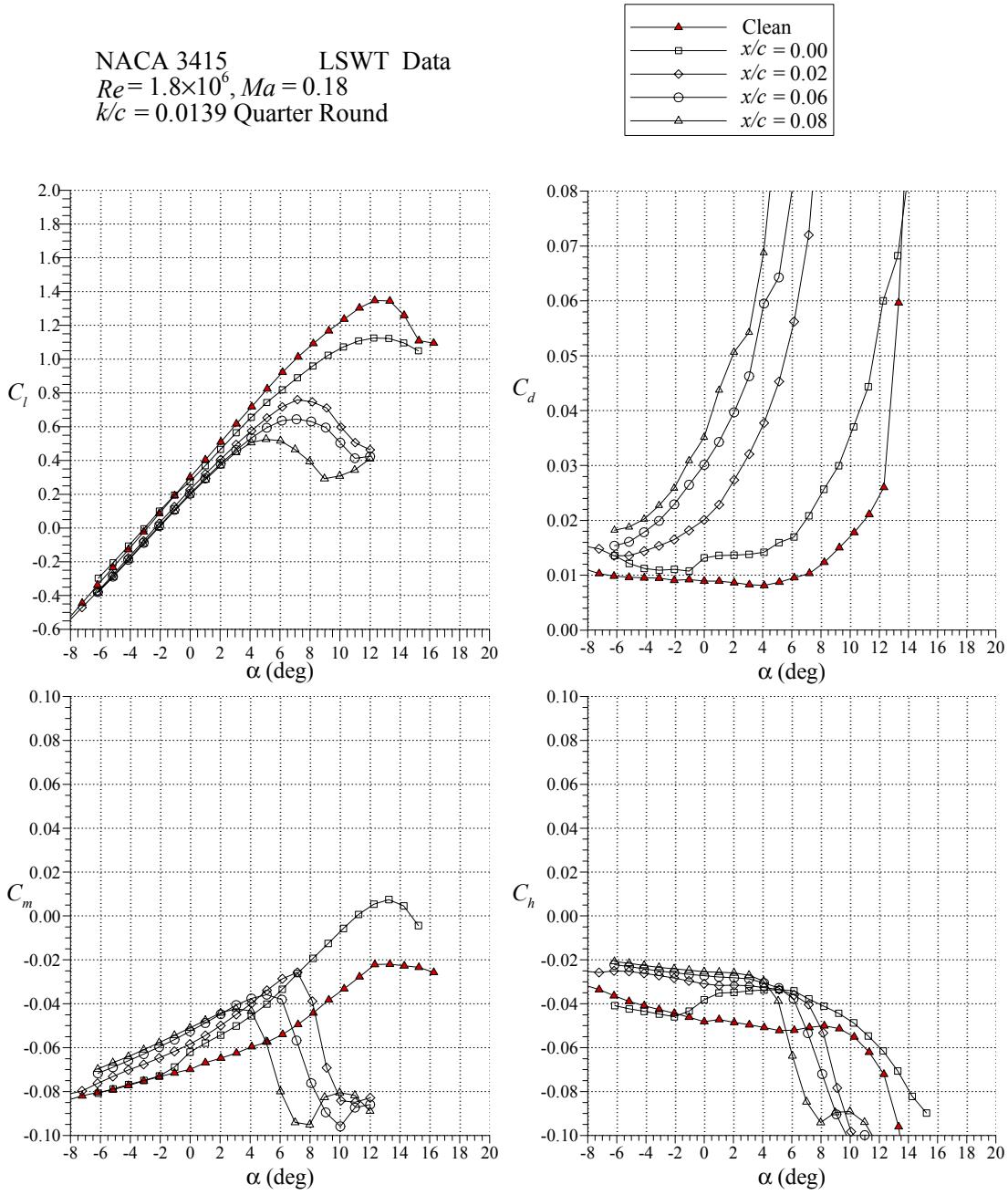

(a) x/c = 0.00 to 0.08

FIGURE 24. EFFECT OF k/c = 0.0139 QUARTER-ROUND ICE SHAPE LOCATION ON NACA 3415 AIRFOIL PERFORMANCE

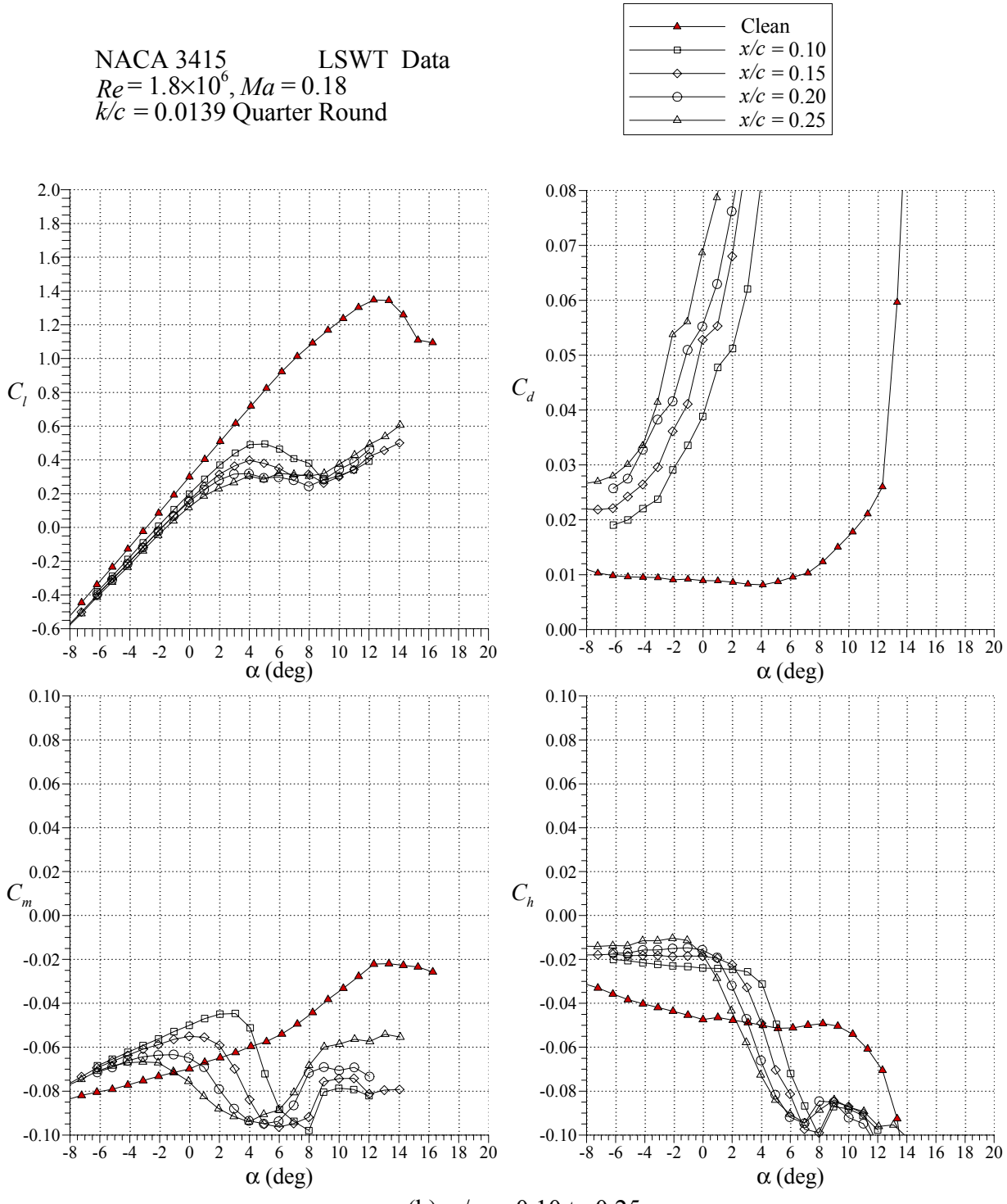

(b) x/c = 0.10 to 0.25

FIGURE 24. EFFECT OF k/c = 0.0139 QUARTER-ROUND ICE SHAPE LOCATION ON NACA 3415 AIRFOIL PERFORMANCE (Continued)

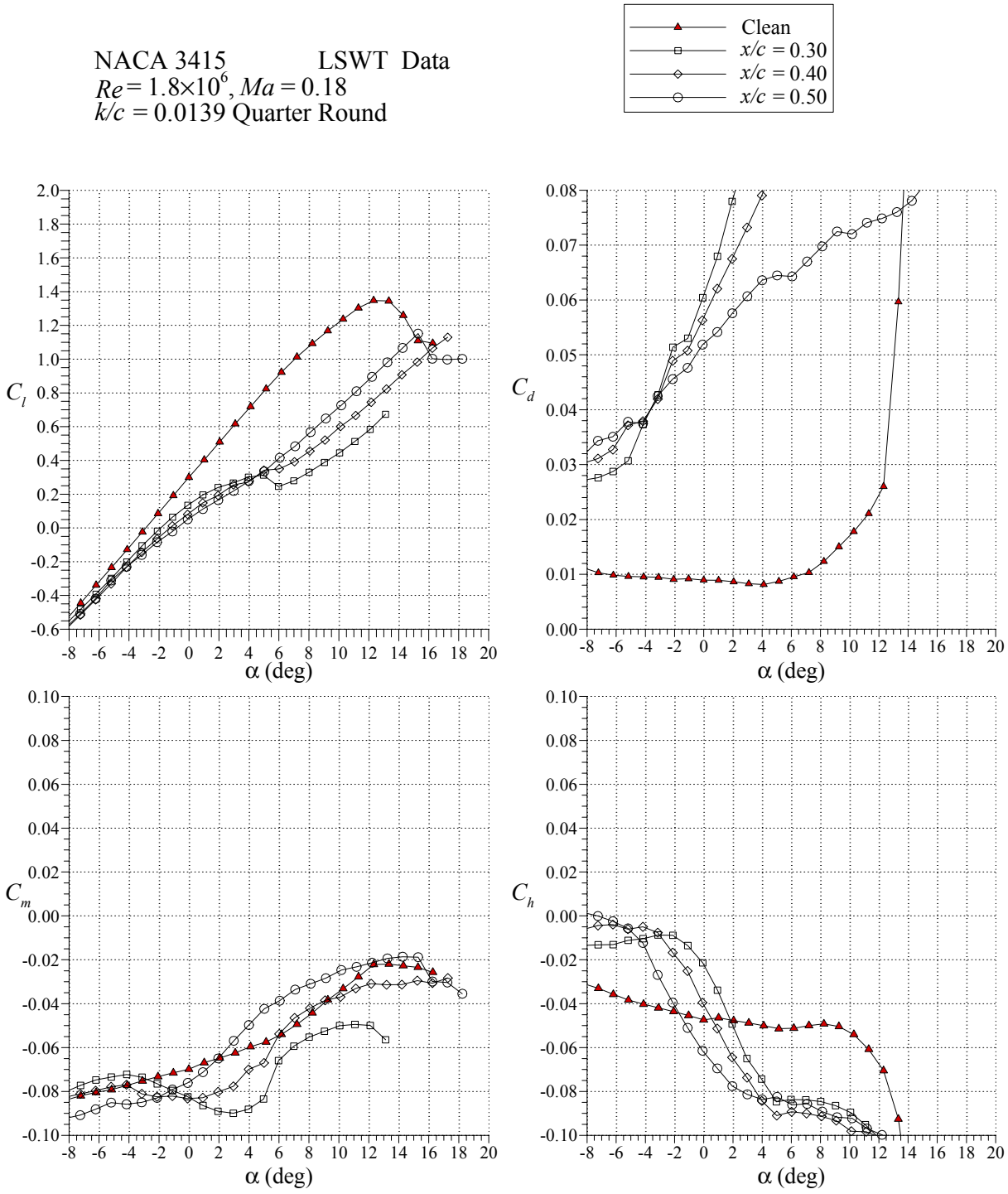

(c) x/c = 0.30 to 0.50

FIGURE 24. EFFECT OF k/c = 0.0139 QUARTER-ROUND ICE SHAPE LOCATION ON NACA 3415 AIRFOIL PERFORMANCE (Continued)

Figures 25 and 26 show pressure distributions with the k/c = 0.0139 quarter round at various chordwise locations for $\alpha = 0°$ and $\alpha = 4°$. Before the iced airfoil pressure distribution is discussed, it is important to understand the basic features. Figure 25(b) shows the pressure distribution on the NACA 3415 with the quarter round at x/c = 0.15. On the upper surface, the C_p decreased as the flow initially accelerated from the leading edge to x/c = 0.08, where it started to decelerate as it encountered an adverse pressure gradient due to the quarter-round ice shape. The flow then accelerated again over the ice shape and separated, resulting in a region of relatively constant C_p between x/c = 0.18 and 0.26. The C_p then increased as the reattachment process began. The reattachment occurred where the iced C_p value approached the clean value and started to take on similar form at x/c = 0.44.

These figures (25 and 26) show that as the ice shape was moved downstream, the separation bubble that formed downstream of it lengthened. When the ice shape was at the leading edge, the separation bubble was so small that it was almost imperceptible through pressure distribution comparisons. In fact, the clean and iced pressure distributions appeared nearly identical. When the ice shape was located at x/c = 0.02 ($\alpha = 0°$, figure 25(a)), the bubble reattached at x/c = 0.12, resulting in a separation length of 10% chord. When the ice shape was located at x/c = 0.10 (figure 25(b)), the bubble length grew to 22% chord. When the ice shape was located at x/c = 0.30, the bubble length grew further to 40% chord. Similar results were observed at $\alpha = 4°$ (figure 26). The lengthening of the bubble was due to the increasingly severe adverse pressure gradient the separation bubble encountered as the ice shape was moved downstream from the leading edge. When the ice shape was located at the leading edge, the bubble formed over a very favorable pressure gradient and was quickly able to reattach. However, as the ice shape was moved downstream, the pressure gradient became less favorable. At $\alpha = 0°$ (figure 25), the pressure gradient started to become adverse at x/c = 0.20. Because of this, as the ice shape was moved downstream from the leading edge, the separation bubble grew, and there was a larger loss in lift.

Figure 27 shows the integrated coefficients on the NACA 3415 with the k/c = 0.0056 quarter round at various chordwise locations. The Reynolds number was 1.8×10^6 and the Mach number was 0.18. The results were quite different from that of the k/c = 0.0139 ice shape shown in figure 24. When the ice shape location was varied between the leading edge and the mid-chord, there was very little difference in the $C_{l,max}$. When the ice shape was at the leading edge, the $C_{l,max}$ was 1.05. When the ice shape was located at mid-chord, the $C_{l,max}$ was 1.0, a difference of only 5%. However, the stall characteristics varied significantly with the ice shape location. When the ice shape was located at the leading edge, there was a very gradual stall, with the lift achieving a maximum value at $\alpha = 11°$, after which it leveled off and remained nearly constant until $\alpha = 17°$. As the ice shape was moved downstream, the stall became more sudden, with the sharpest stall occurring when the ice shape was located at x/c = 0.20. At this location, the C_l dropped from 1.04 at $\alpha = 11°$ to 0.54 at $\alpha = 12°$, a loss in lift of almost 50% with only 1 degree change in angle of attack. As the ice shape was moved further downstream from this location, the lift curve at stall became more rounded, and the stall became more gradual.

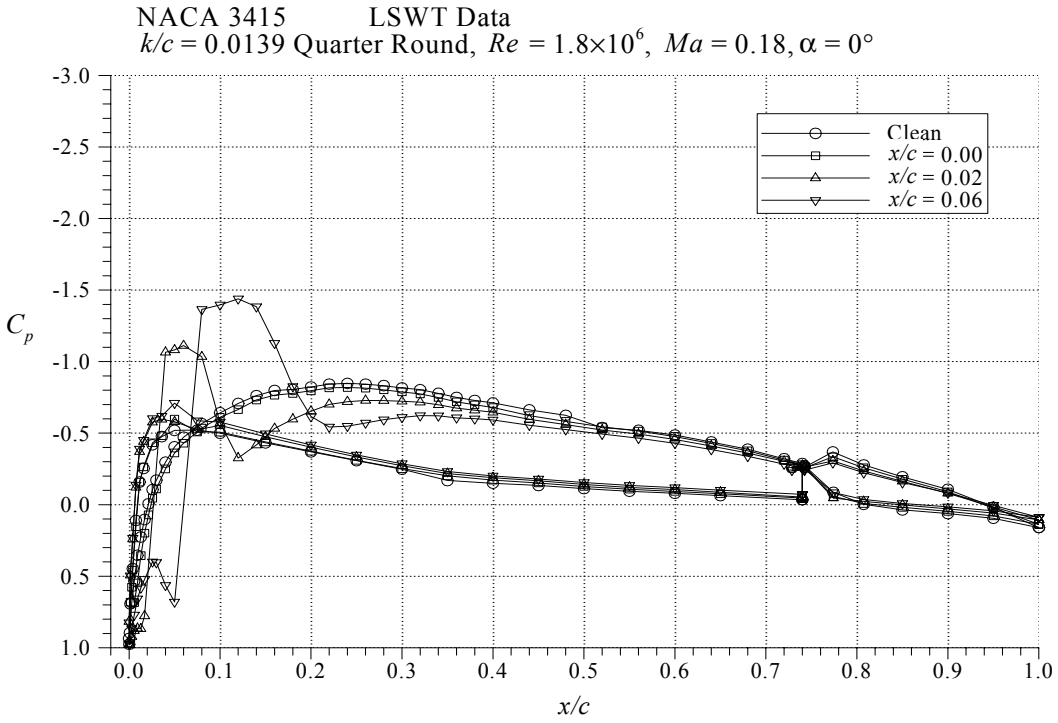

(a) x/c = 0.00 to 0.06

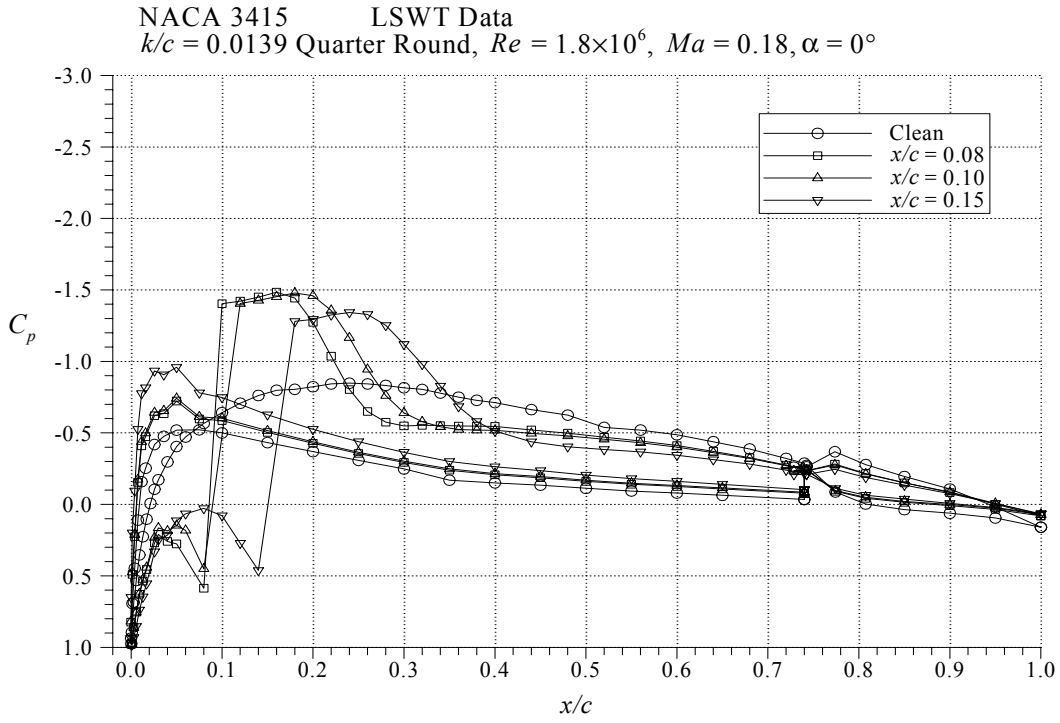

(b) x/c = 0.08 to 0.15

FIGURE 25. EFFECT OF k/c = 0.0139 QUARTER-ROUND ICE SHAPE LOCATION ON NACA 3415 AIRFOIL PRESSURE DISTRIBUTION AT $\alpha = 0°$

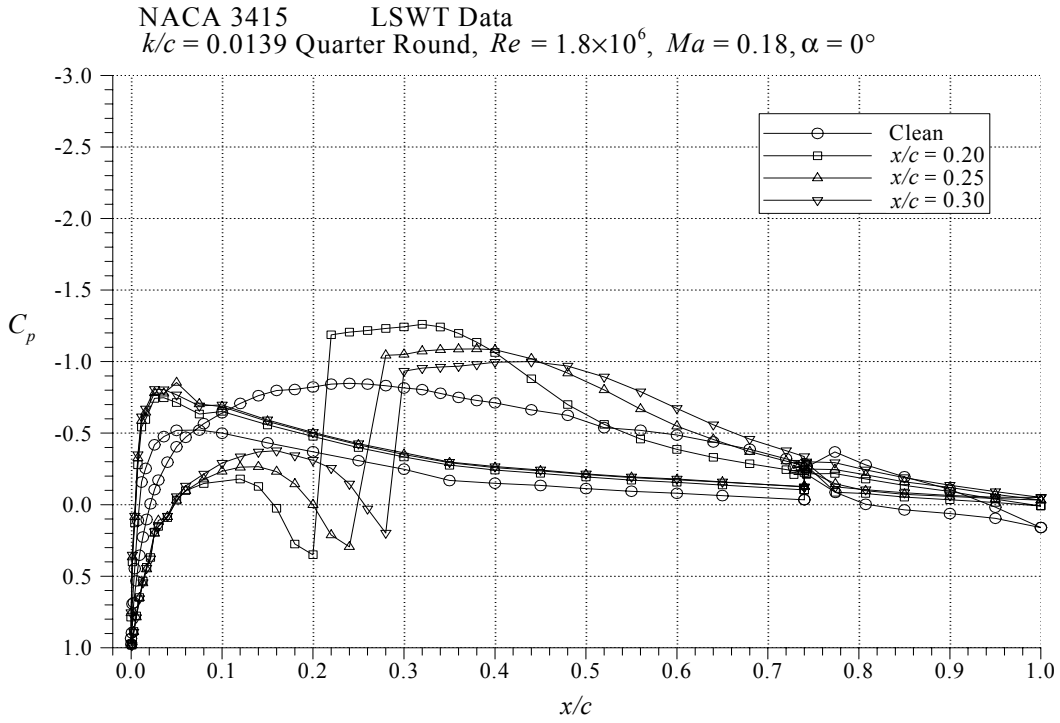

(c) x/c = 0.20 to 0.30

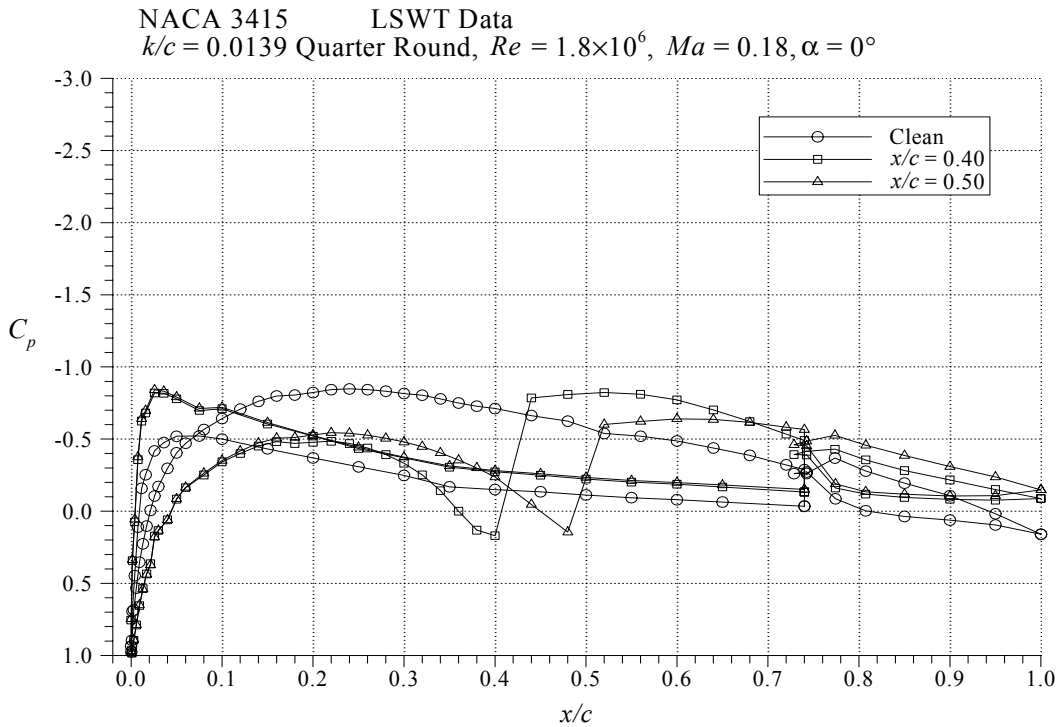

(d) x/c = 0.40 to 0.50

FIGURE 25. EFFECT OF k/c = 0.0139 QUARTER-ROUND ICE SHAPE LOCATION ON NACA 3415 AIRFOIL PRESSURE DISTRIBUTION AT α = 0° (Continued)

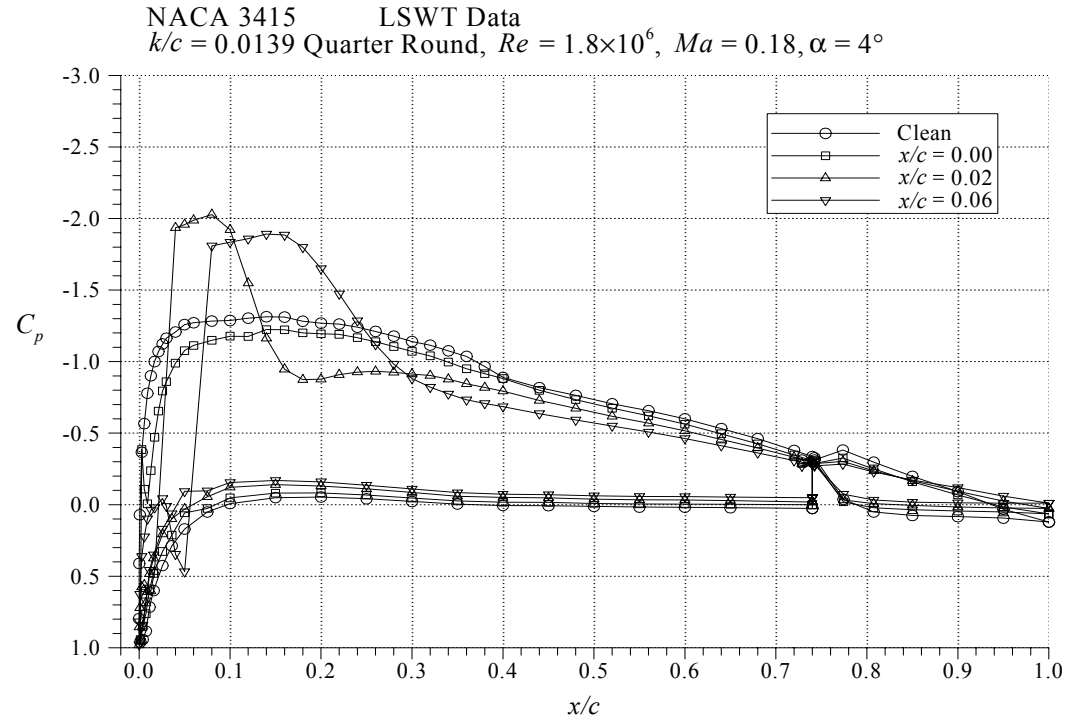

(a) x/c = 0.00 to 0.06

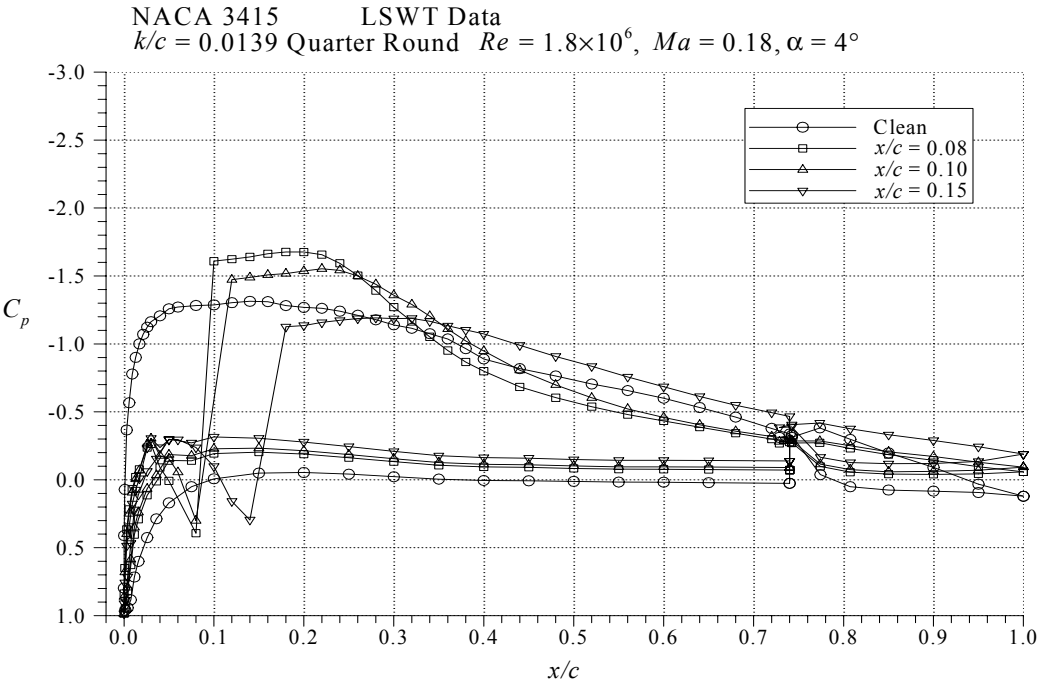

(b) x/c = 0.08 to 0.15

FIGURE 26. EFFECT OF k/c = 0.0139 QUARTER-ROUND ICE SHAPE LOCATION ON NACA 3415 AIRFOIL PRESSURE DISTRIBUTION AT $\alpha = 4°$

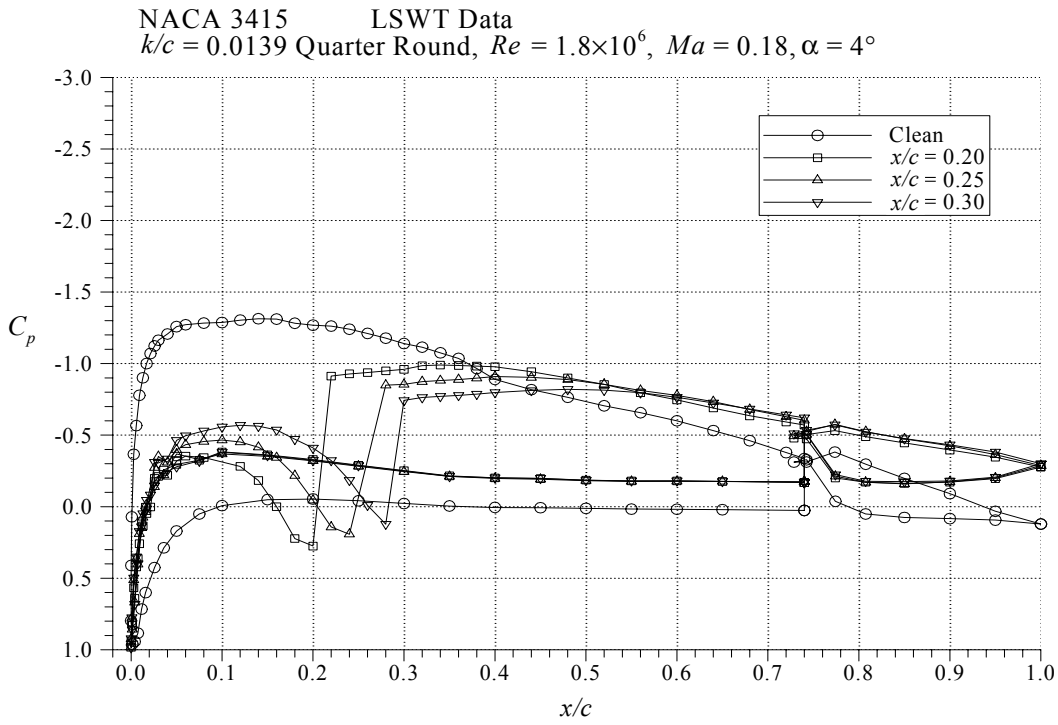

(c) x/c = 0.20 to 0.30

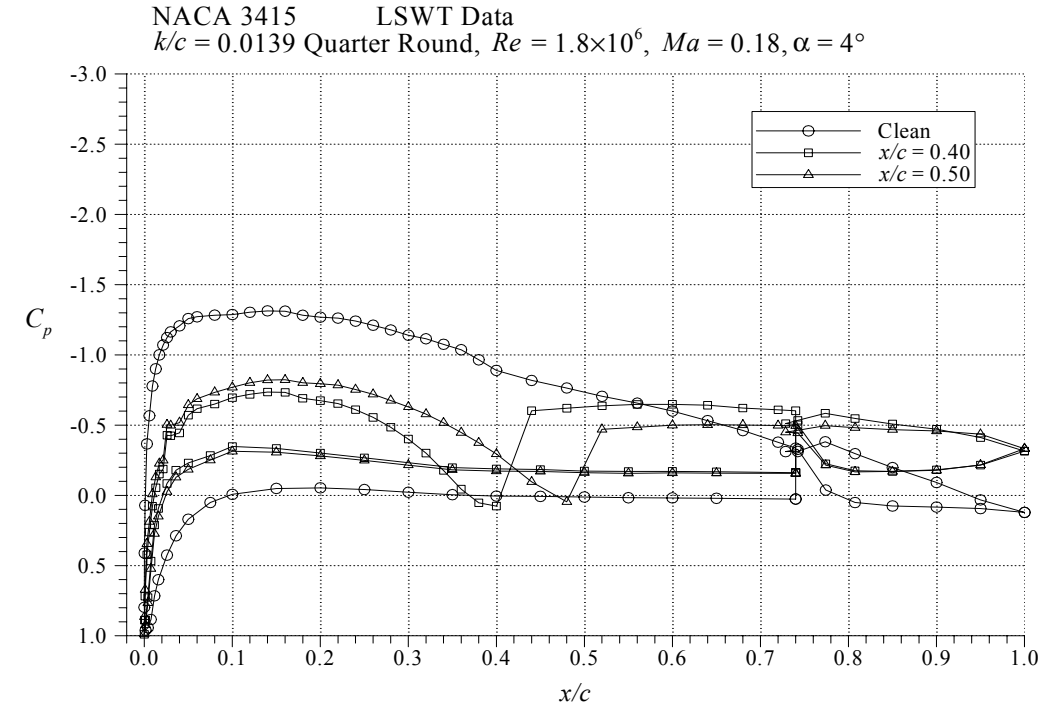

(d) x/c = 0.40 to 0.50

FIGURE 26. EFFECT OF k/c = 0.0139 QUARTER-ROUND ICE SHAPE LOCATION ON NACA 3415 AIRFOIL PRESSURE DISTRIBUTION AT α = 4° (Continued)

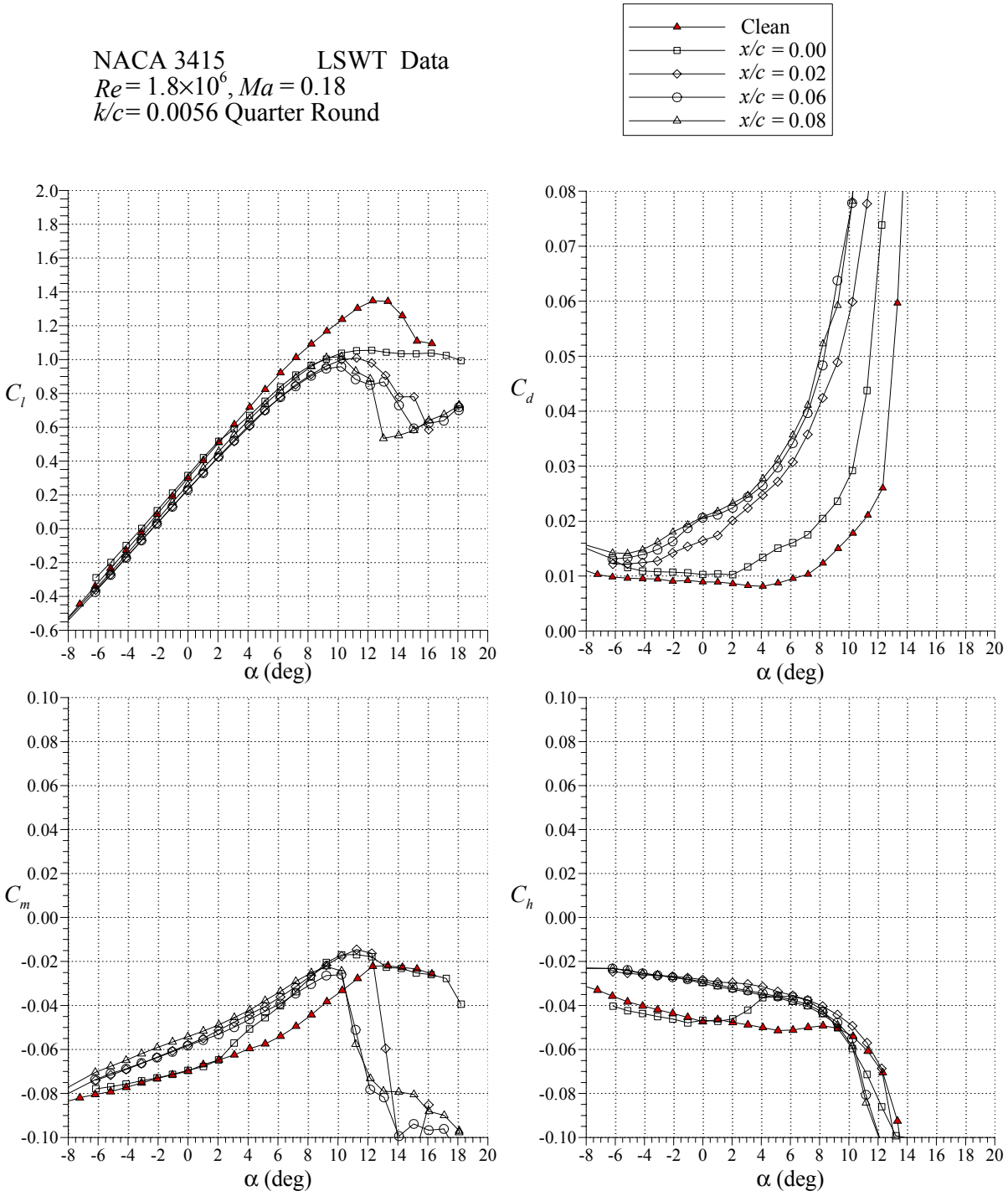

(a) x/c = 0.00 to 0.08

FIGURE 27. EFFECT OF k/c = 0.0056 QUARTER-ROUND ICE SHAPE LOCATION ON NACA 3415 AIRFOIL PERFORMANCE

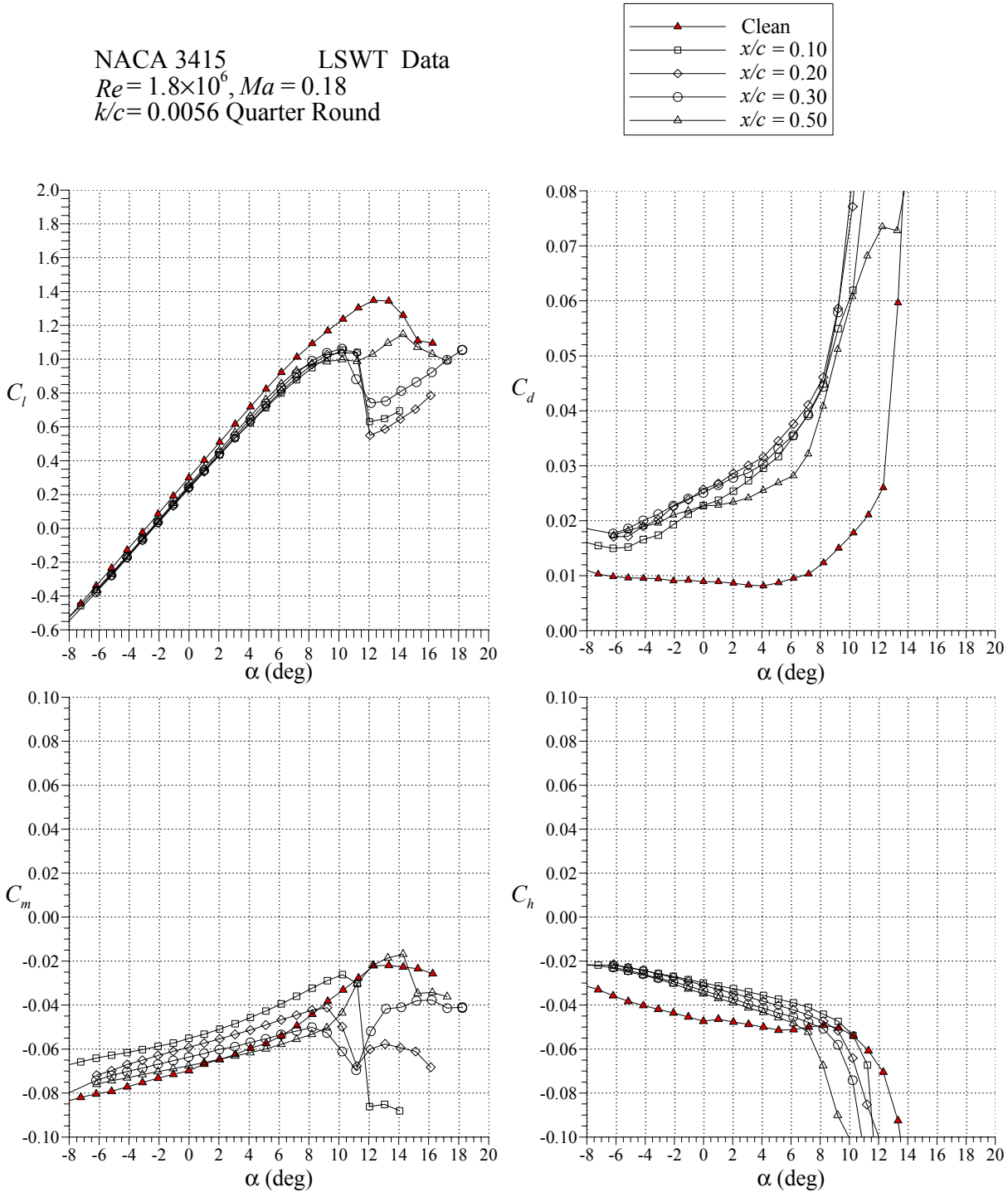

(b) x/c = 0.10 to 0.50

FIGURE 27. EFFECT OF k/c = 0.0056 QUARTER-ROUND ICE SHAPE LOCATION ON NACA 3415 AIRFOIL PERFORMANCE (Continued)

As the ice shape was moved downstream from the leading edge to x/c = 0.20, the drag increased as well. However, as it was moved further downstream, the drag values at positive angles of attack decreased. The ice shape location where the largest drag occurred coincided with the location that resulted in the sharpest stall. The pitching moment results showed that as the ice shape location was moved from x/c = 0.02 to 0.30, there was not a large change in the angle of attack at which there was a negative break in the C_m. In this range of ice shape location, the angle of attack at which the break in the C_m occurred changed by only 4°. For the larger k/c = 0.0139 ice shape, the angle of attack changed by 12°. Similar results were observed for the flap hinge moments. As the ice shape location was varied between x/c = 0.02 and 0.50, the angle of attack at which the break in the C_h curve occurred changed from 9° to 7°. For the k/c = 0.0139 ice shape, the angle of attack changed from 6° to -6°.

The results described above with the two ice shape heights are summarized in figure 28, the $C_{l,max}$ with varying ice shape locations. When the k/c = 0.0139 ice shape was tested on the NACA 3415, there was a rapid drop in the $C_{l,max}$ as the ice shape was moved downstream from the leading edge to x/c = 0.20. As the ice shape location was varied from x/c = 0.20 to 0.40, there was little further decrease in the $C_{l,max}$. As stated before, the $C_{l,max}$ = 0.20 value shown for the x/c = 0.50 location was not a $C_{l,max}$ value in the traditional sense but the lift value when the flow downstream of the ice shape became completely separated. The $C_{l,max}$ value, when the k/c = 0.0056 quarter round was tested, was relatively insensitive to the ice shape location. When the ice shape location was varied between x/c = 0.00 to 0.50, there was less than 10% variation in the $C_{l,max}$ values.

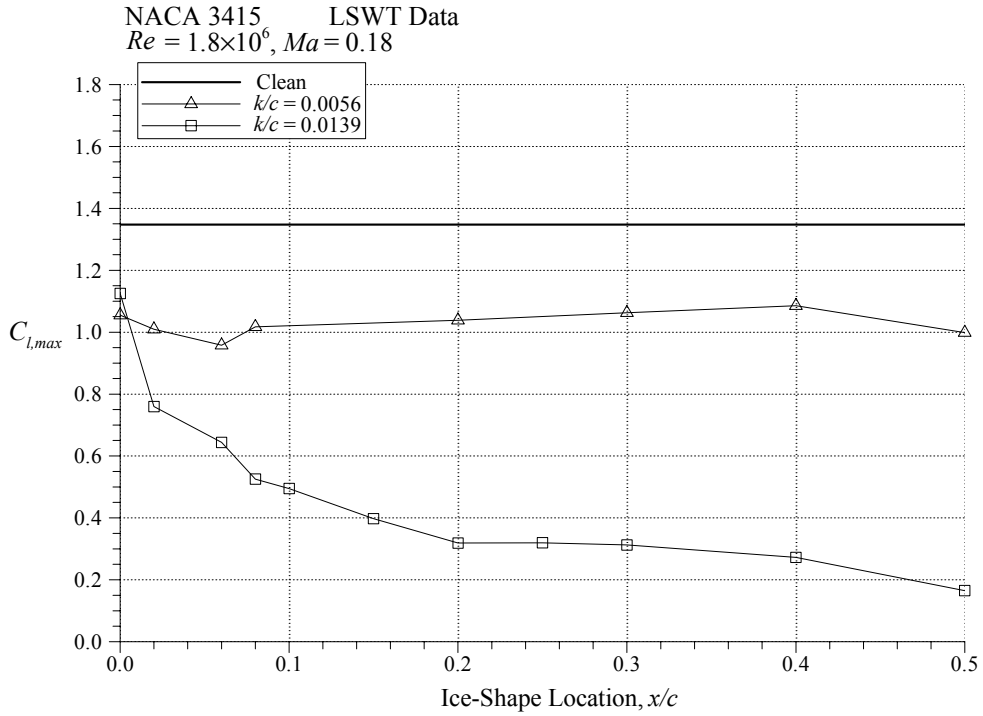

FIGURE 28. EFFECT OF QUARTER-ROUND ICE SHAPE LOCATION ON NACA 3415 AIRFOIL $C_{l,max}$

The large differences in the performance between the two ice shape heights tested were due to the differences in the separation bubble lengths. Figure 29 shows the pressure distributions with the two quarter-round heights at various chordwise locations. When the quarter round was located at the leading edge, the difference in the ice shape height had little effect on the pressure distribution because the bubble that formed downstream of the ice shapes were able to attach quickly in the very favorable pressure gradient. This explained the similar $C_{l,max}$ shown when the two ice shapes were located at the leading edge. In fact, the separation bubbles were so small that the overall pressure distributions of the iced airfoil were nearly identical to that of the clean airfoil.

Larger differences were observed when the ice shape was located at $x/c = 0.02$, as shown in figure 29(b). The separation bubble that formed downstream of the $k/c = 0.0056$ ice shape reattached at $x/c = 0.10$, while the $k/c = 0.0139$ ice shape reattached at $x/c = 0.18$. This made the separation bubble that formed downstream of the larger ice shape twice as long. However, the bubble lengths were still relatively small and the effect on the pressure distribution over the entire length of the chord was similar. Figures 29(c) and 29(d) show that as the ice shape was moved further downstream to $x/c = 0.10$ and 0.20, the differences in the ice shape height had a progressively larger effect. When the ice shape was located at $x/c = 0.10$, the bubble that formed downstream of the larger ice shape was three times longer than the bubble that formed downstream of the smaller shape. When the ice shape was located at $x/c = 0.20$, the separation bubble that formed downstream of the larger ice shape appeared to have completely separated off the surface. However, the bubble from the smaller shape reattached at $x/c = 0.34$.

The pressure distribution plots of figure 29 show that for the larger ice shape, the separation bubble became progressively larger as the ice shape was moved downstream from the leading edge. This resulted in a decreasing $C_{l,max}$ as the ice shape was moved downstream. However, for the smaller ice shape, the separation bubble length did not vary significantly as the ice shape was moved downstream, resulting in nearly constant $C_{l,max}$, as shown in figure 28.

Figure 30 shows the effect of the Reynolds and Mach numbers on the integrated aerodynamic coefficients for the $k/c = 0.0139$ quarter round on the NACA 3415. It is very important to note that in the LSWT, increasing the Reynolds number also resulted in the increase in the free-stream Mach number as well. Thus, any differences observed at different Reynolds number could have been the result of Mach number variations. When the ice shape was located at the leading edge, increasing the Reynolds number from 1.0×10^6 to 1.8×10^6 (and the free-stream Mach number from 0.10 to 0.18) had little effect on the integrated aerodynamic coefficients. However, as the ice shape was moved downstream, the differences became progressively larger. Increasing the Reynolds and Mach numbers decreased $C_{l,max}$, increased drag, and caused the negative slope breaks in the C_m and C_h to occur at lower angles of attack. Again, because the Reynolds and Mach numbers could not independently be changed, it was not known what these differences were attributed to. However, results from the LTPT tests indicated that it was likely due to Mach number differences (cf. section 4.2.2).

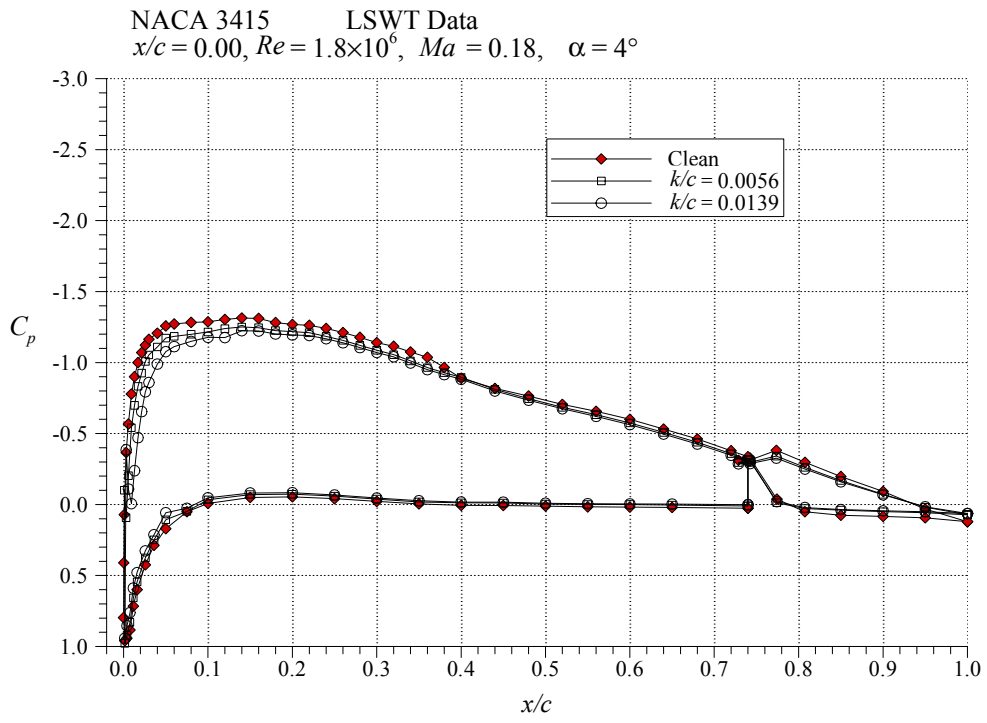

(a) $x/c = 0.00$

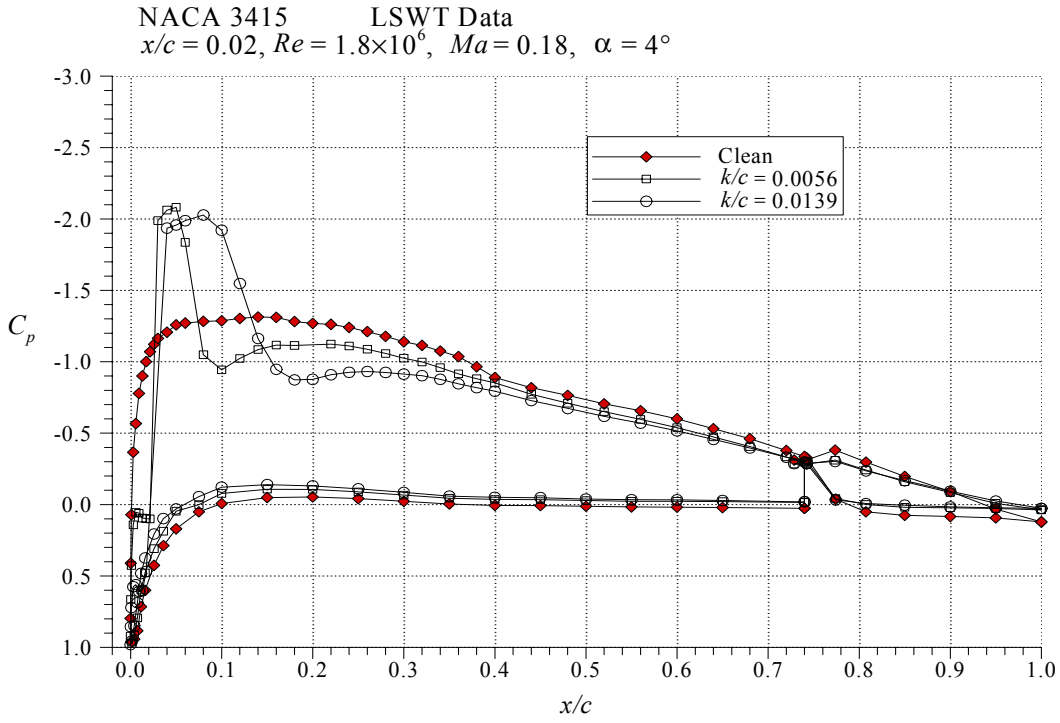

(b) $x/c = 0.02$

FIGURE 29. EFFECT OF QUARTER-ROUND ICE SHAPE HEIGHT ON NACA 3415 AIRFOIL PRESSURE DISTRIBUTION

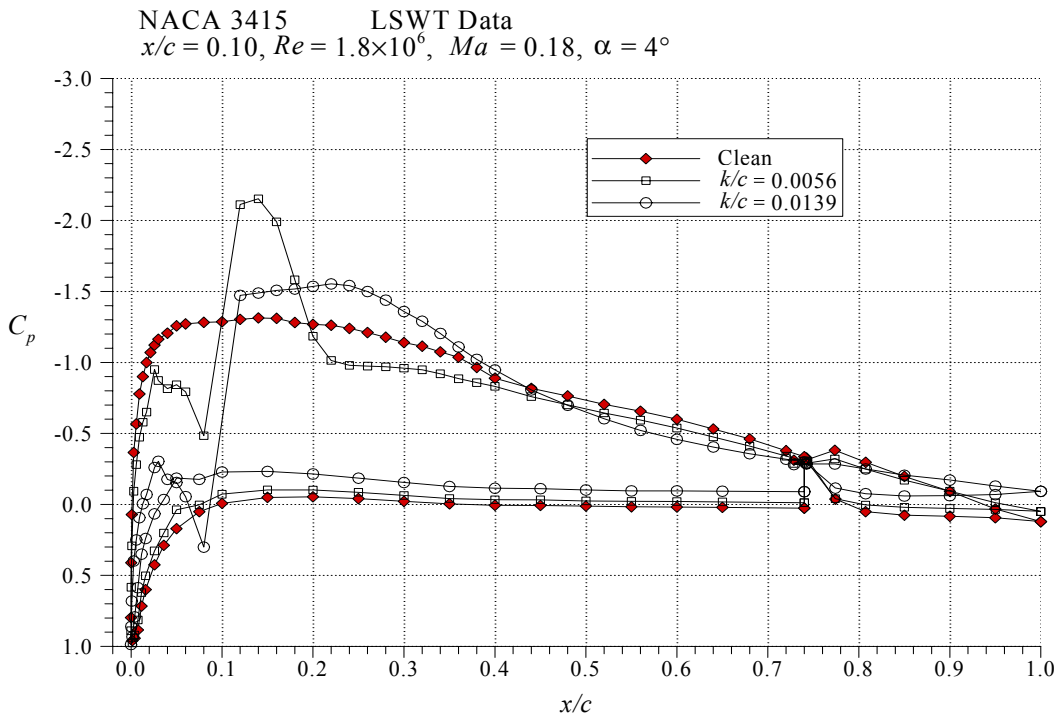

(c) $x/c = 0.10$

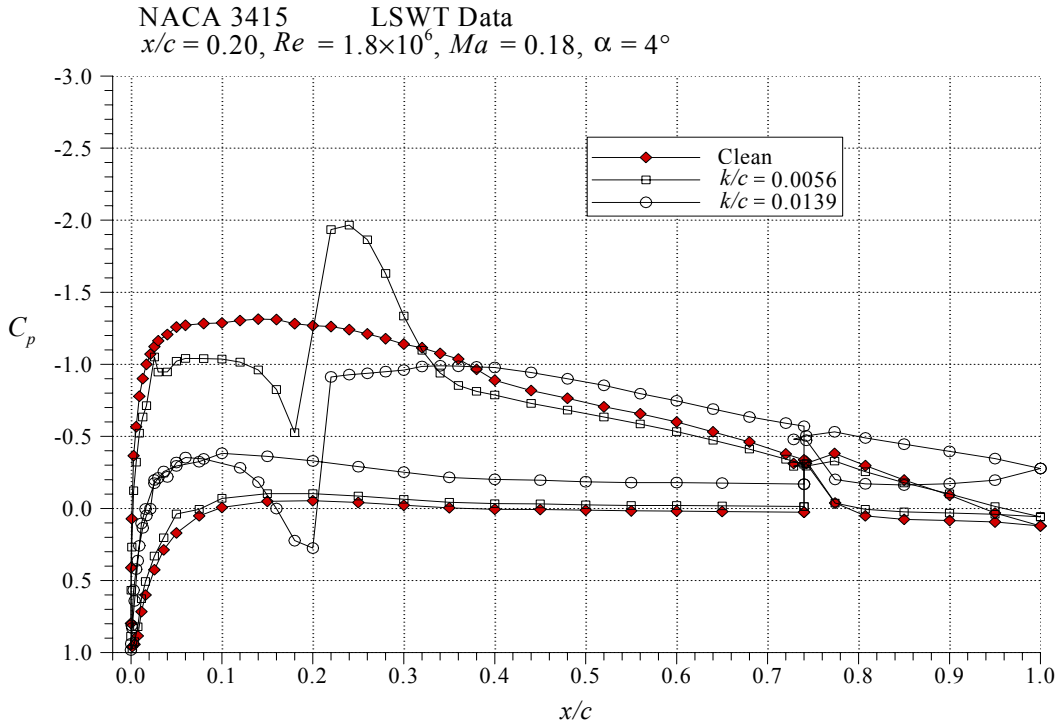

(d) $x/c = 0.20$

FIGURE 29. EFFECT OF QUARTER-ROUND ICE SHAPE HEIGHT ON NACA 3415 AIRFOIL PRESSURE DISTRIBUTION (Continued)

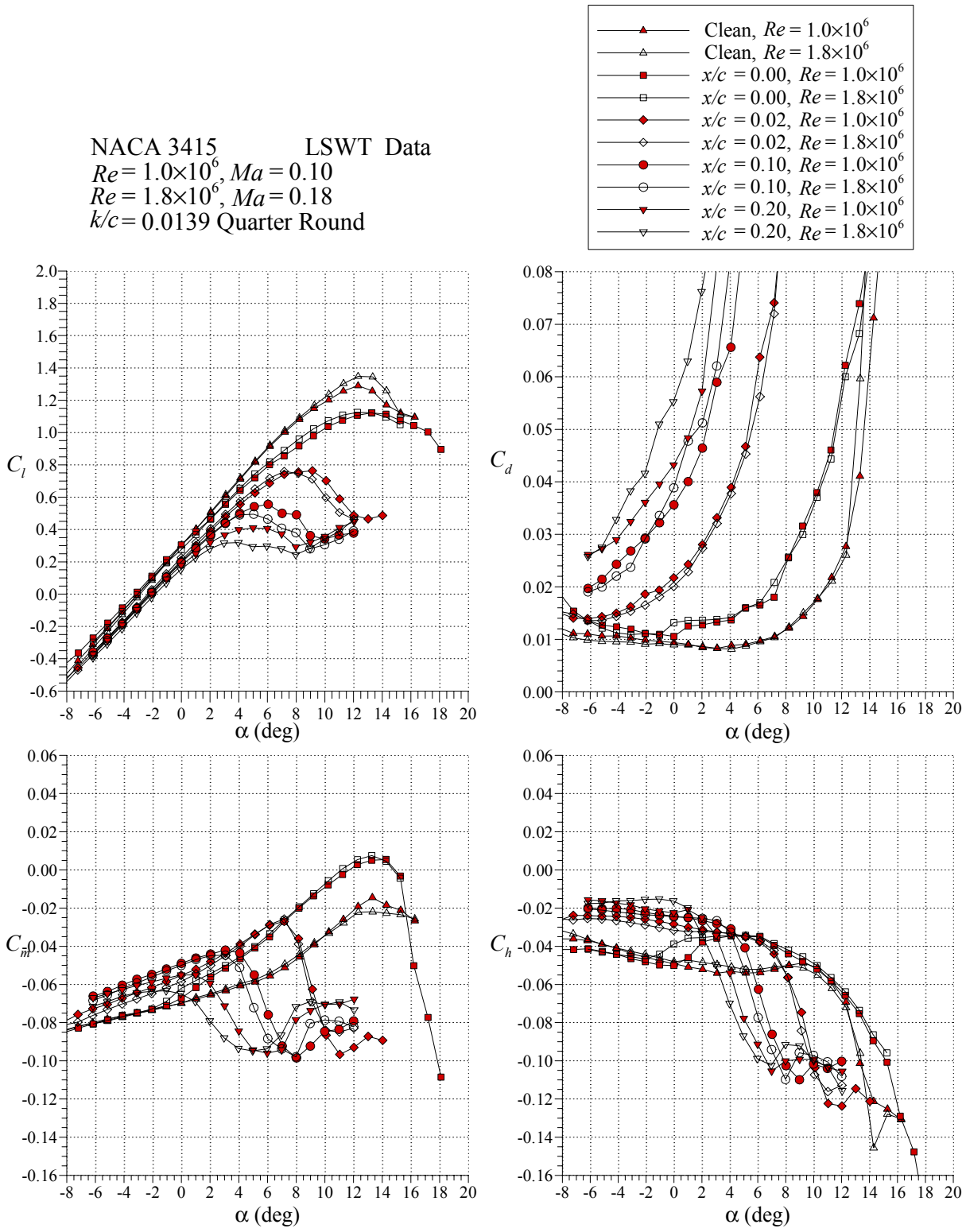

FIGURE 30. EFFECT OF REYNOLDS AND MACH NUMBERS ON ICED NACA 3415 AIRFOIL PERFORMANCE

Figure 31 shows the effect of Reynolds and Mach numbers on the iced airfoil pressure distribution. It shows that as the ice shape was moved downstream, the separation bubbles at higher Reynolds and Mach numbers became progressively longer. The C_p in the constant pressure region immediately downstream of the ice shape was more positive, and the C_p at the trailing edge was more negative, indicating increased loss in momentum at higher Reynolds and Mach numbers. This resulted in lower lift, higher drag, and earlier occurrence of the break in C_m and C_h. As indicated above, these results were determined to be consistent with trends for differences in Mach number, as described in section 4.2.2.

The effect of airfoil geometry is shown in figure 32. Figure 32(a) shows that on the NACA 23102m, moving the ice shape downstream from the leading edge to $x/c = 0.10$ resulted in both decreased $C_{l,max}$ and α_{stall}. However, when the ice shape was located at $x/c = 0.20$, a traditionally defined $C_{l,max}$ was not observed. There was a break in the lift curve slope at $\alpha = 2°$ as the flow downstream of the ice shape became completely separated. However, lift continued to be generated upstream of the ice shape because the flow was still attached in this region. Because of this, increasing the angle of attack further increased lift, but at a much lower rate. The lift values, when the ice shape was located at $x/c = 0.20$, were higher than that of $x/c = 0.10$ location at all angles of attack. The drag at positive angles of attack was also lower when the ice shape was located at $x/c = 0.20$, when compared to $x/c = 0.10$.

On the NACA 3415 (figure 32(b)), moving the ice shape location downstream from the leading edge to $x/c = 0.20$ resulted in progressively lower $C_{l,max}$ and higher drag. On the NLF 0414 (figure 32c), moving the ice shape location from the leading edge to $x/c = 0.02$ resulted in $C_{l,max}$ dropping from 1.04 to 0.73. Moving the ice shape farther downstream had little effect on $C_{l,max}$.

Figure 33 shows a summary of $C_{l,max}$ as a function of the quarter-round location for the three airfoils tested at the LSWT. The airfoil models were tested with ice shapes located as far downstream as mid-chord. However, only the data points for which a clear $C_{l,max}$ existed are shown. As stated previously, on the NACA 23012m, a $C_{l,max}$ in the traditional sense was not observed when the ridge ice was located between $x/c = 0.14$ and 0.30. Figure 33 shows that generally moving the ridge ice downstream resulted in larger degradations of maximum lift (the exception being the NACA 23012m). For all three airfoil models, the highest $C_{l,max}$ was observed when the ridge ice was located at the leading edge. The NACA 23012m was most sensitive to the ridge ice location in the first 20% chord, followed by the NACA 3415 and the NLF 0414. There was little variation in $C_{l,max}$ when the quarter-round location was varied between $x/c = 0.02$ and 0.20 on the NLF 0414. However, on the NACA 23012m and the NACA 3415, moving the ridge ice from $x/c = 0.02$ to 0.20 caused significant reductions in the maximum lift.

The reason for the differences in the sensitivity of the airfoils to the ridge ice location was attributed to the differences in the clean model pressure distributions. Generally, the severity of the effect of ridge ice is directly related to the length of the separation bubble that forms downstream of the ice shape. This in turn is determined primarily by the severity of the adverse pressure gradient downstream of the ice shape, over which the bubble is forced to reattach. More severe adverse gradient typically results in a longer separation bubble.

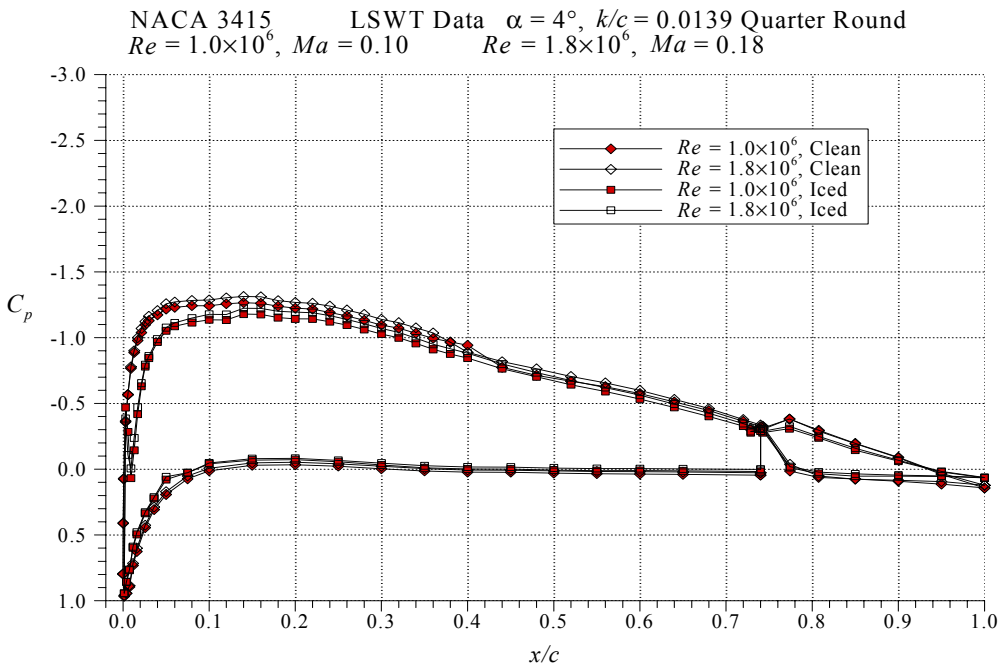

(a) $x/c = 0.00$

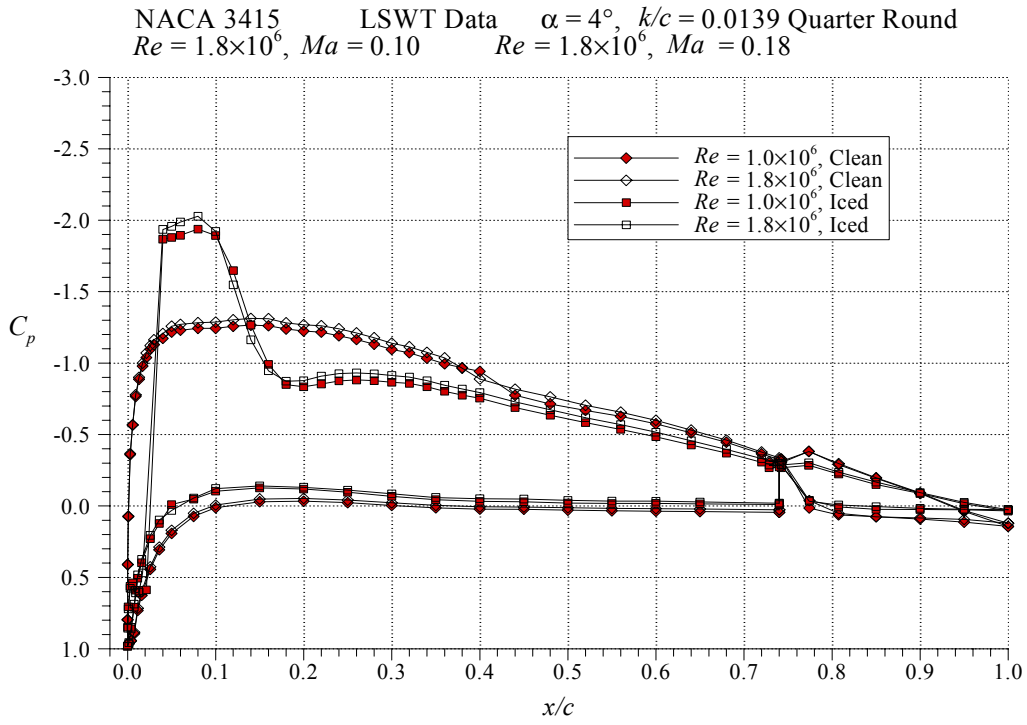

(b) $x/c = 0.02$

FIGURE 31. EFFECT OF REYNOLDS AND MACH NUMBERS ON ICED NACA 3415 AIRFOIL PRESSURE DISTRIBUTION

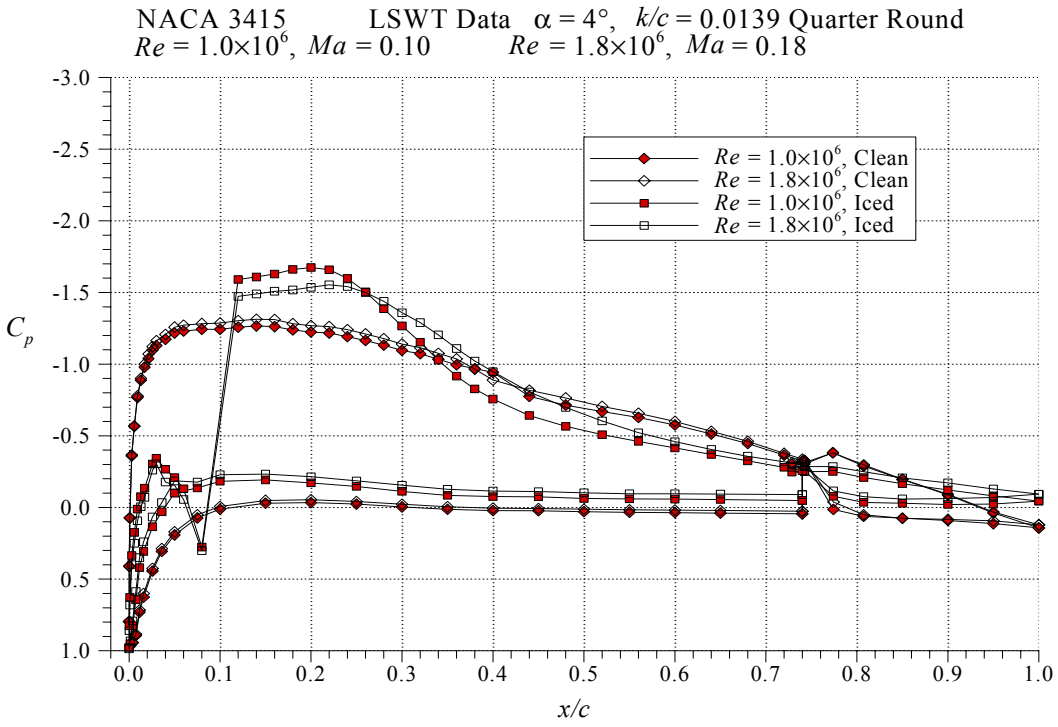

(c) $x/c = 0.10$

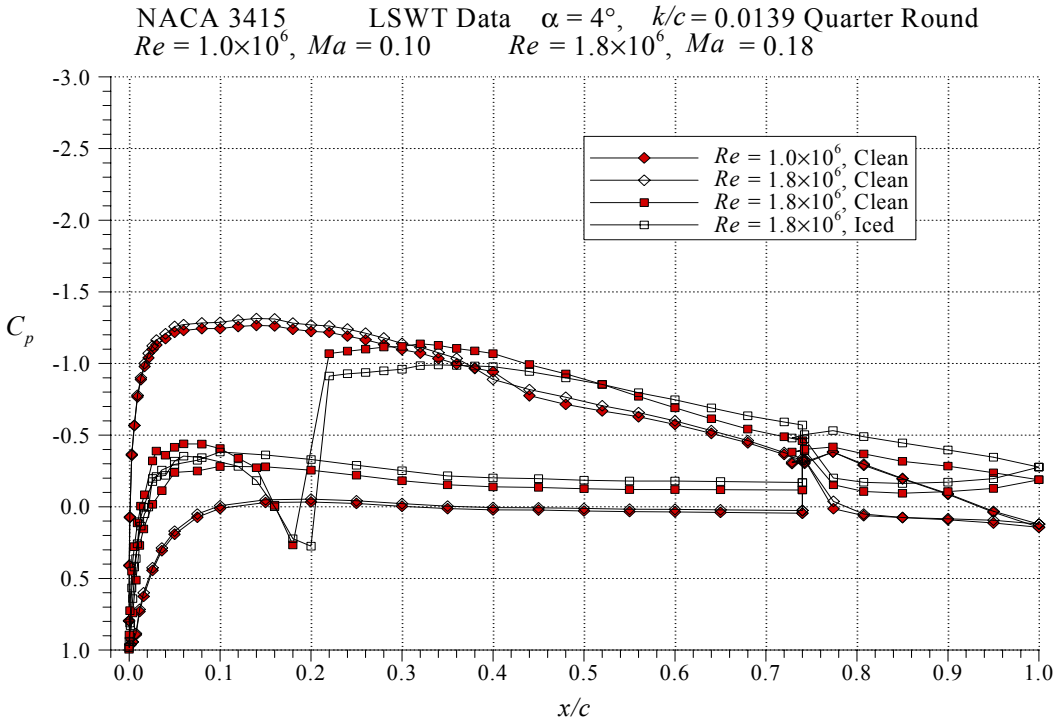

(d) $x/c = 0.20$

FIGURE 31. EFFECT OF REYNOLDS AND MACH NUMBERS ON ICED NACA 3415 AIRFOIL PRESSURE DISTRIBUTION (Continued)

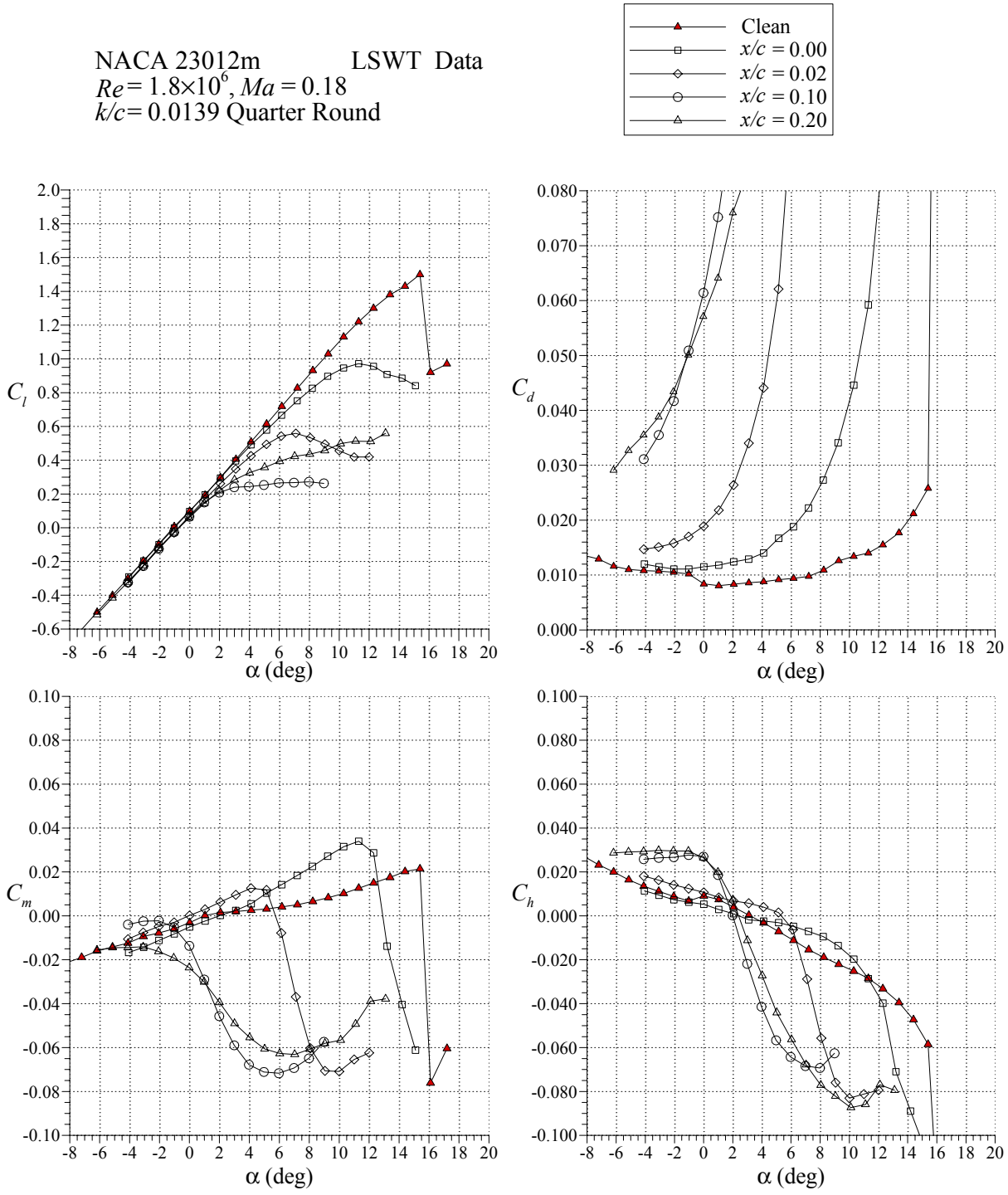

(a) NACA 23012M

FIGURE 32. EFFECT OF QUARTER-ROUND ICE SHAPE LOCATION ON THE THREE AIRFOILS TESTED AT LSWT

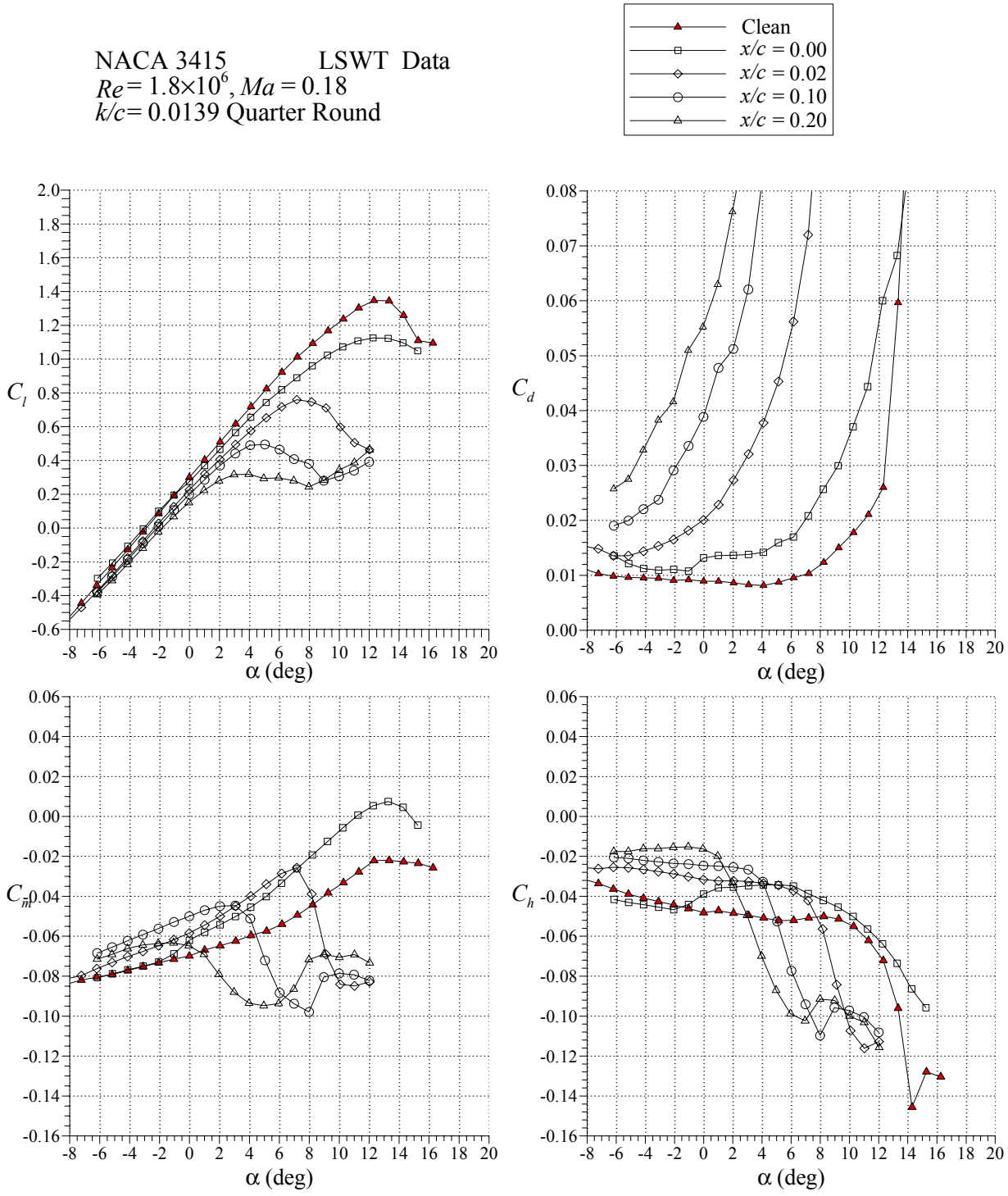

(b) NACA 3415

FIGURE 32. EFFECT OF QUARTER-ROUND ICE SHAPE LOCATION ON THE THREE AIRFOILS TESTED AT LSWT (Continued)

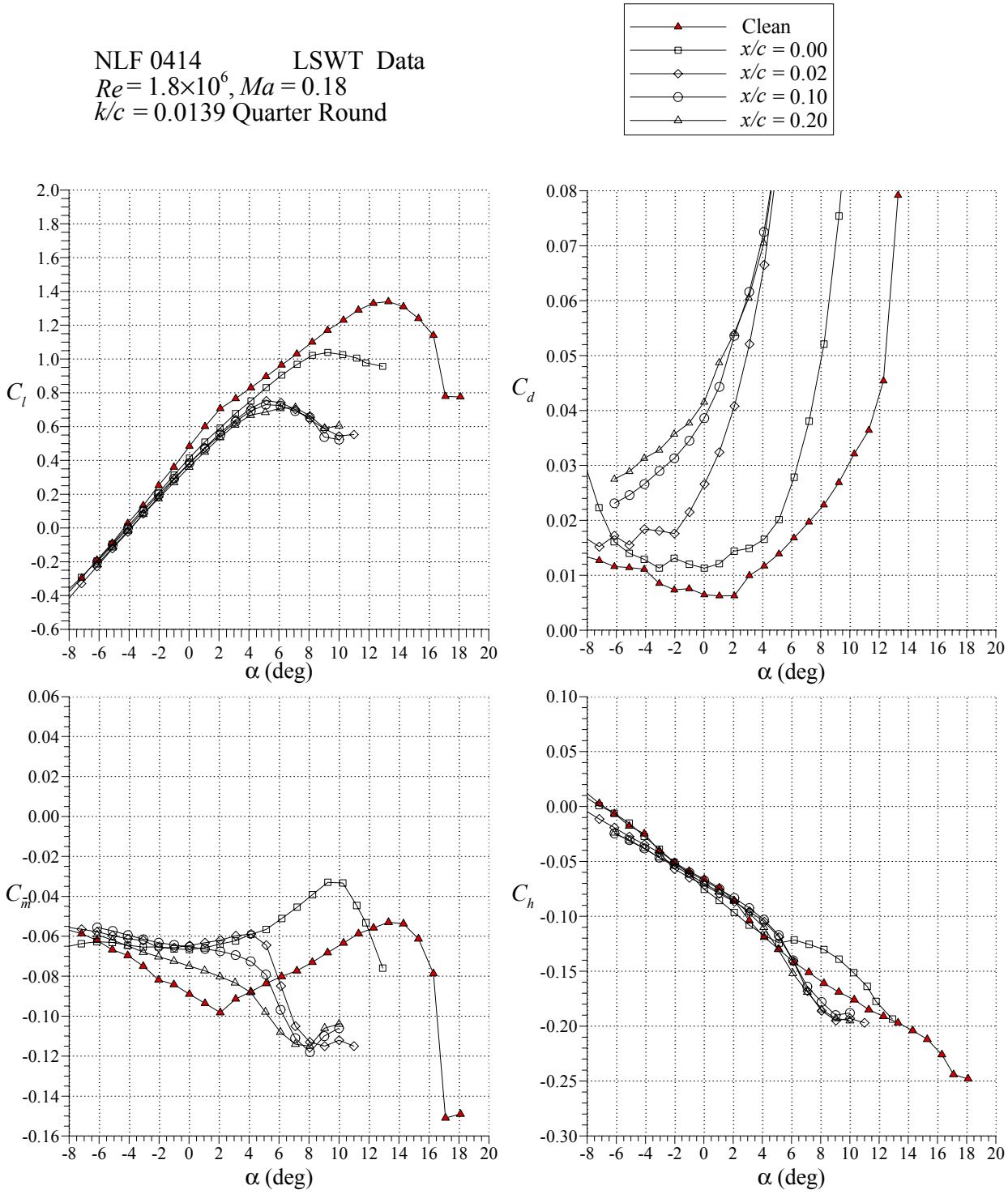

(c) NLF 0414

FIGURE 32. EFFECT OF QUARTER-ROUND ICE SHAPE LOCATION ON THE THREE AIRFOILS TESTED AT LSWT (Continued)

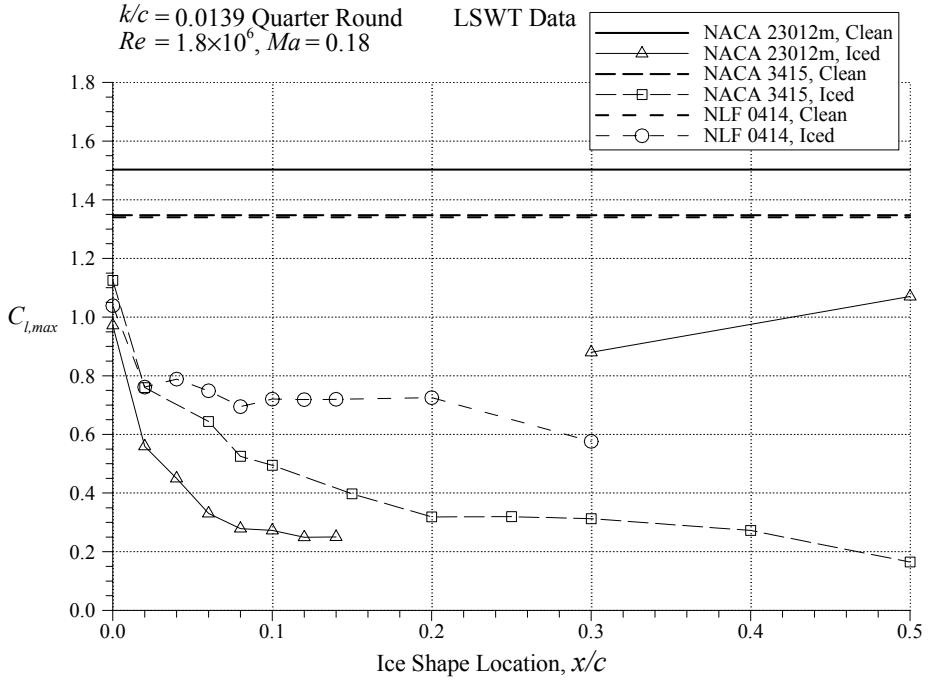

FIGURE 33. EFFECT OF QUARTER-ROUND ICE SHAPE LOCATION ON $C_{l,max}$ FOR THE THREE AIRFOILS TESTED AT LSWT

The effect of ridge ice on surface pressure distribution is shown in figure 34. All the clean models are at $C_l = 0.5$, which explains the various angles of attack. Figure 34(a) shows why the NACA 23012m was the most sensitive airfoil when the ridge ice was located in the first 20% chord. Because the NACA 23012m had a large suction peak near the leading edge, it also had a very severe pressure recovery region that extended from $x/c = 0.10$ to 0.20. If an ice shape was located upstream of $x/c = 0.20$, the resulting separation bubble would be located in this region of very adverse pressure gradient. The bubble cannot easily reattach in this region, resulting in a long bubble. This is shown in figure 34(a), where the ridge ice was located at $x/c = 0.10$. The pressure distribution on the upper surface of the iced airfoil did not approach the clean case after the initial separation over the ice shape. This indicated that the bubble failed to reattach on the airfoil (which was confirmed by flow visualization).

The adverse gradient on the NACA 3415 was not as severe as the NACA 23012m. Thus, the separation bubble that formed downstream of the ice shapes was not as large, resulting in less lift degradation, as shown in figure 34(b). The bubble appeared to have reattached at $x/c = 0.40$. The pressure gradient on the NLF 0414 is shown in figure 34(c). On the clean model, the adverse gradient (where the recovery took place) on the NLF 0414 did not begin until $x/c = 0.74$. Ahead of the recovery region, the pressure gradient was nearly zero. Because of this, the lift was relatively insensitive to the ice shape location near the leading edge, as the bubble did not encounter an adverse pressure gradient. As the ridge ice was moved downstream, it was not until the ridge ice was located at $x/c = 0.30$ that the bubble encountered the adverse gradient and the maximum lift started to experience additional penalty. When the ridge ice was located at $x/c = 0.10$, the bubble reattached at $x/c = 0.35$.

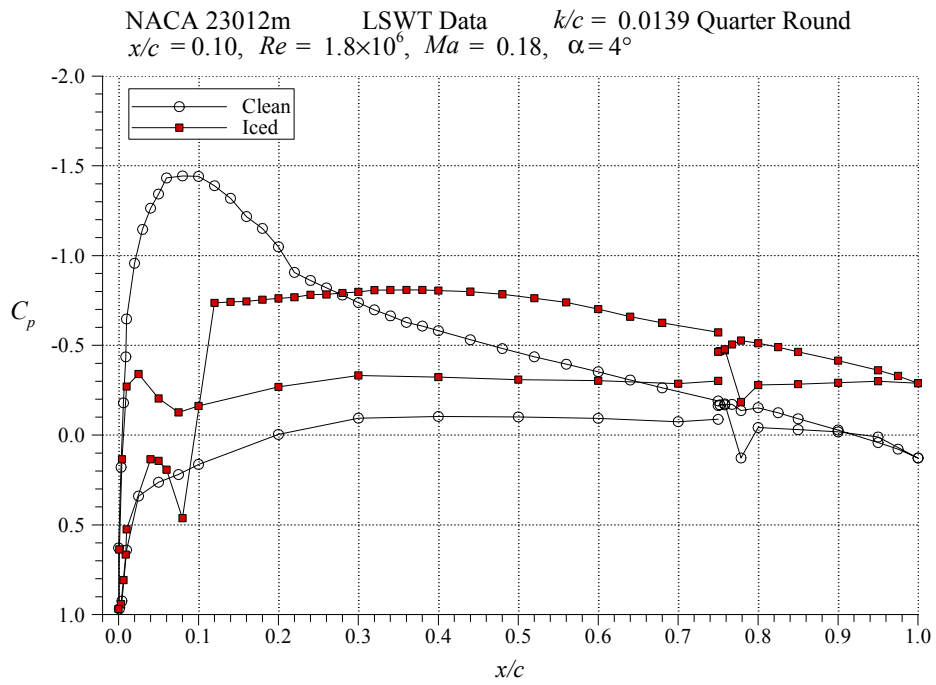

(a) NACA 23012M

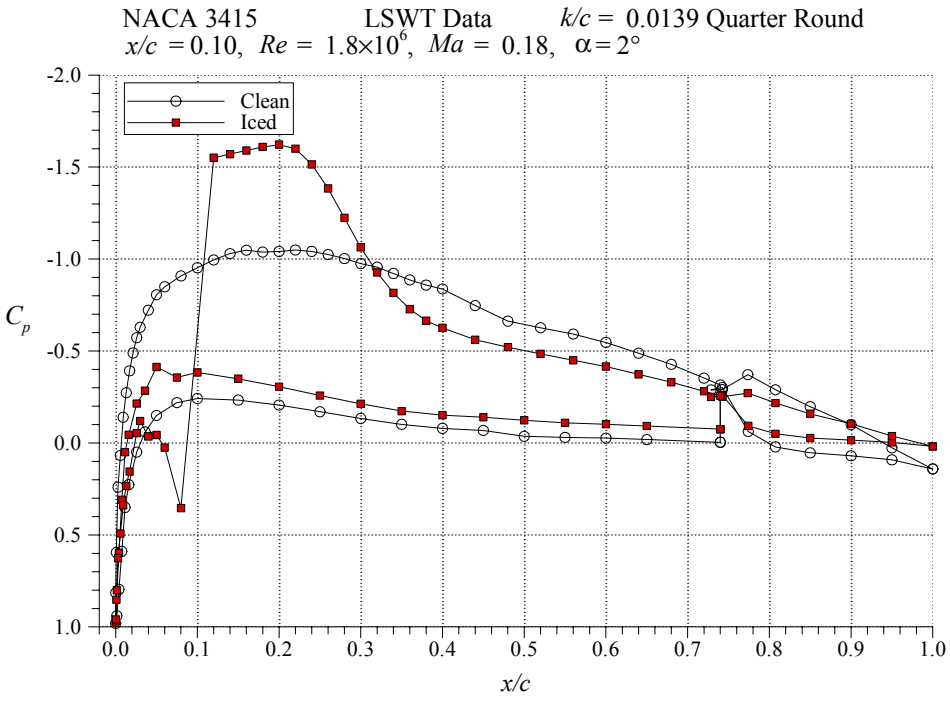

(b) NACA 3415

FIGURE 34. EFFECT OF QUARTER-ROUND ICE SHAPE LOCATION ON PRESSURE DISTRIBUTION FOR THE THREE AIRFOILS TESTED AT LSWT

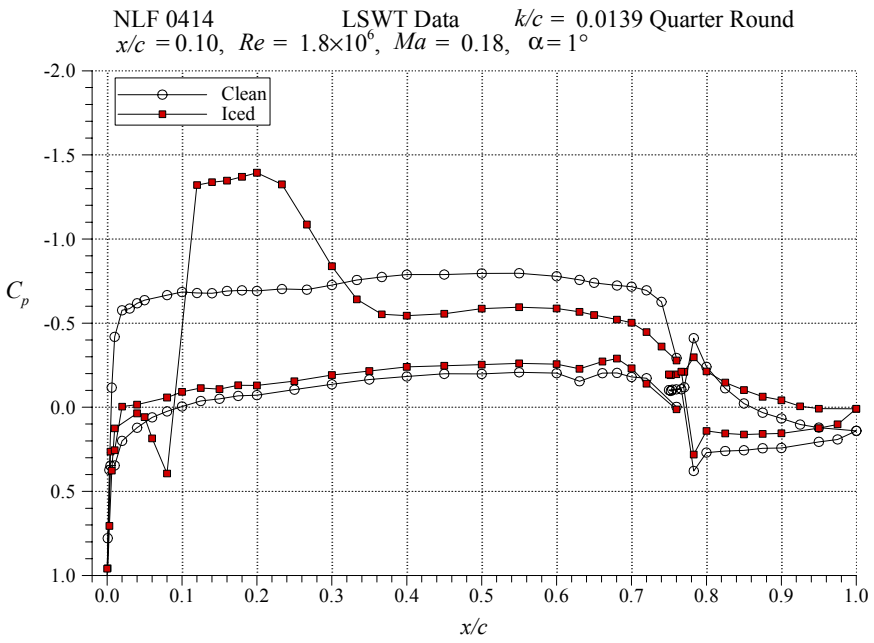

(c) NLF 0414

FIGURE 34. EFFECT OF QUARTER-ROUND ICE SHAPE LOCATION ON PRESSURE DISTRIBUTION FOR THE THREE AIRFOILS TESTED AT LSWT (Continued)

The results shown above indicated that generally the more front-loaded the airfoil was (with large leading-edge suction peak), the more sensitive it was to SLD-type ridge ice accretion. Of the three airfoils tested, the NACA 23012m was the most front-loaded, with the largest suction peak. It had the largest performance degradation due to ridge ice accretion, especially in the 10%-20% chord range where it is likely to occur. The NLF 0414, which was the most aft-loaded of the airfoils tested, was the most insensitive to SLD ridge ice accretion. The NACA 3415 fell in between the NACA 23012m and the NLF 0414 in terms of being front-loaded. The performance degradations on the NACA 3415 also fell in between the NACA 23012m and the NLF 0414.

4.2.2 Reynolds and Mach Numbers Effects.

A limited number of ridge-type ice simulations were tested on the NACA 23012 airfoil over a large Reynolds and Mach numbers range in the LTPT. It should be noted that this section was written with the intent of highlighting the differences caused by Reynolds and Mach numbers. However, it is important to retain a proper perspective because these differences are much smaller than the change in performance due to the ice shape simulation itself. Figure 35 shows the effect of Reynolds number at constant Mach number for the k/c = 0.0139 quarter round located at x/c = 0.10. The lift coefficient data exhibit virtually no dependence on Reynolds numbers over the range shown. The effects were small in the pitching moment and drag. Behavior of the drag coefficients was consistent with clean airfoil behavior, where the values were slightly lower for the higher Reynolds numbers. The effect of Reynolds number (or lack thereof) on lift coefficient for the quarter round located at x/c = 0.02 is shown in figure 36 and

was very similar to the $x/c = 0.10$ case. More typical Reynolds numbers effects were observed with the quarter round located at $x/c = 0.20$. As shown in figure 37, there was a noticeable increase in $C_{l,max}$ from $Re = 3.5\times10^6$ to 10.5×10^6. It is unclear whether this change in trends was due to the quarter-round location. Locations downstream of $x/c = 0.20$ were not tested at the LTPT.

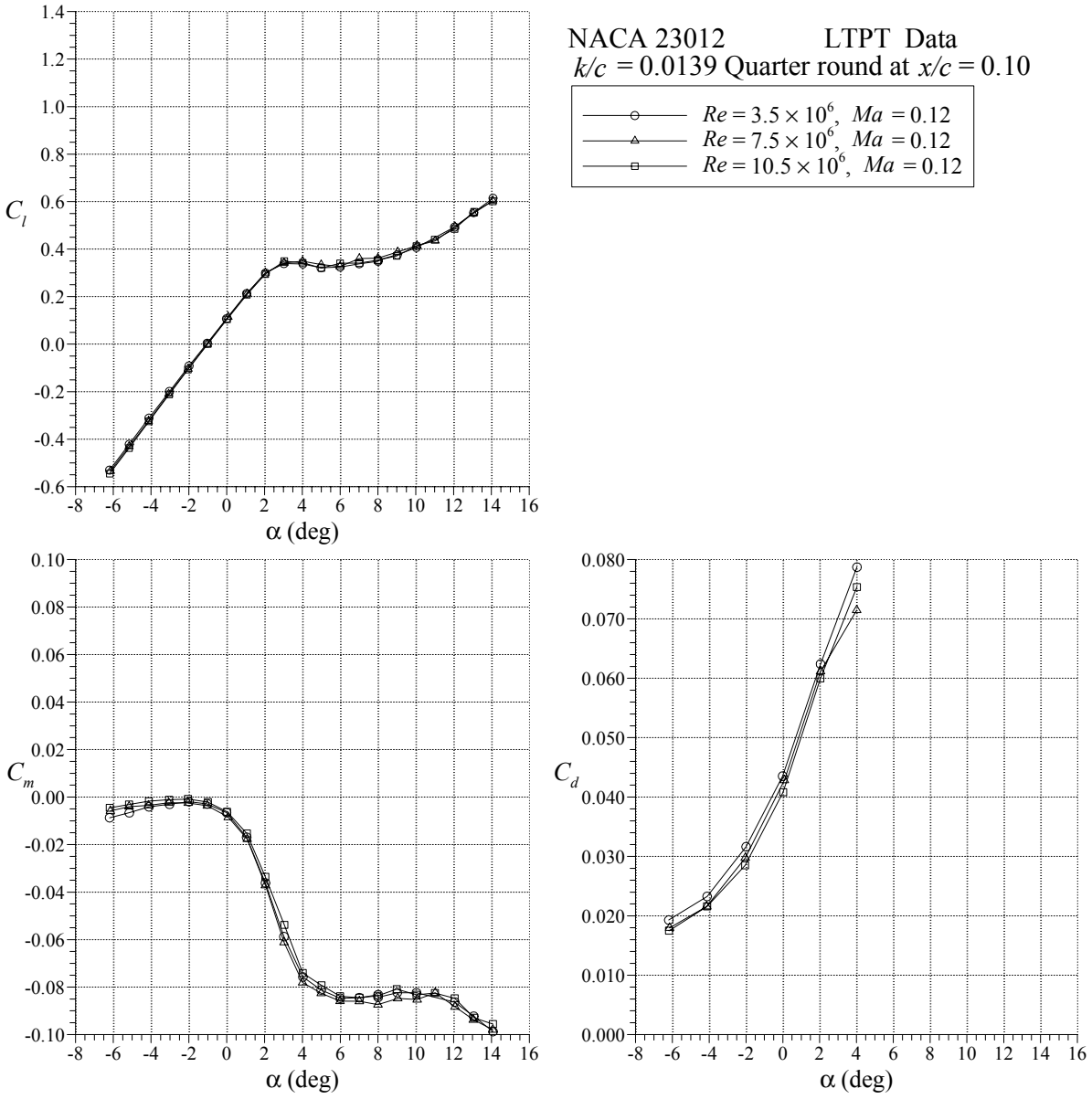

FIGURE 35. EFFECT OF REYNOLDS NUMBER ON NACA 23012 AIRFOIL PERFORMANCE WITH $k/c = 0.0139$ QUARTER ROUND AT $x/c = 0.10$

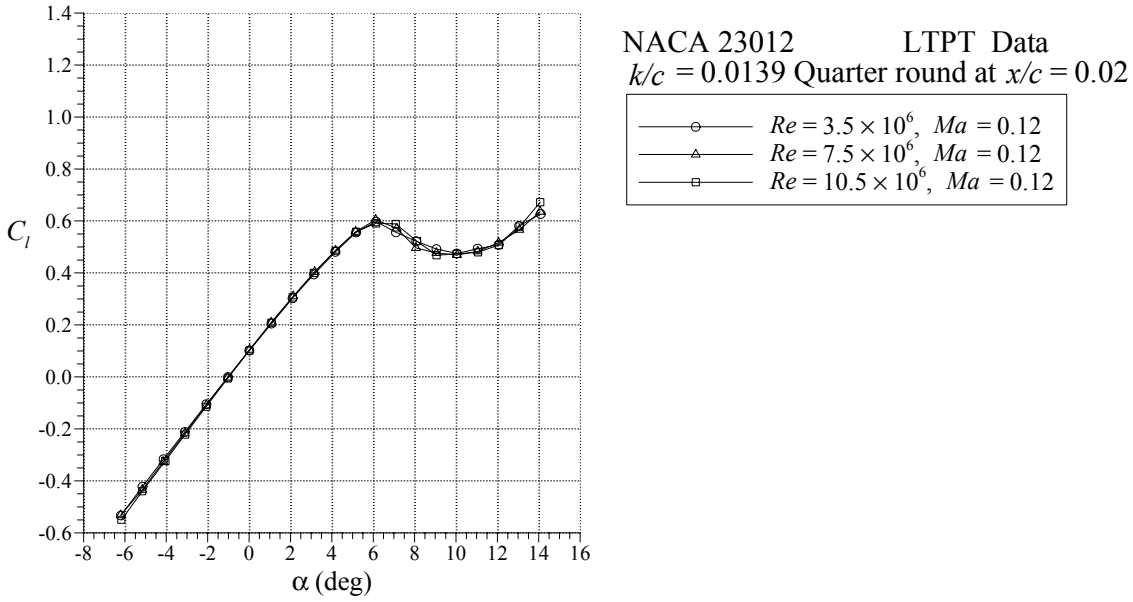

FIGURE 36. EFFECT OF REYNOLDS NUMBER ON NACA 23012 AIRFOIL PERFORMANCE WITH k/c = 0.0139 QUARTER ROUND AT x/c = 0.02

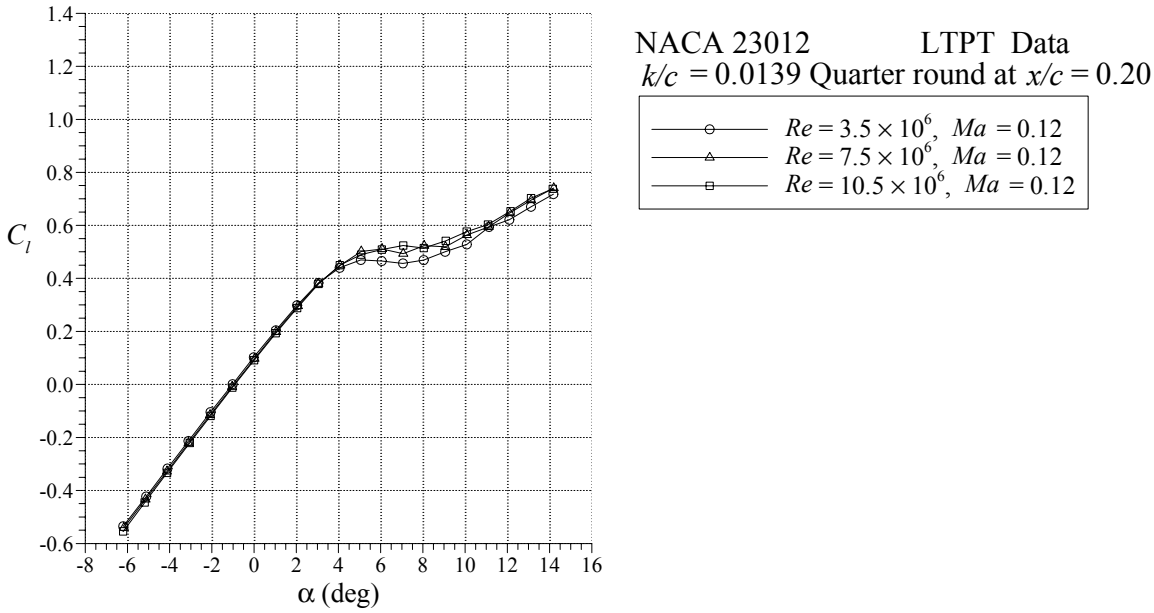

FIGURE 37. EFFECT OF REYNOLDS NUMBER ON NACA 23012 AIRFOIL PERFORMANCE WITH k/c = 0.0139 QUARTER ROUND AT x/c = 0.20

The stalling characteristics of the NACA 23012 airfoil with the simulated SLD ridge-type ice simulations were effected more by changes in Mach number at constant Reynolds number. This is illustrated in figure 38 for the k/c = 0.0139 quarter round located at x/c = 0.10. The general change in stall behavior was similar to the clean case, where the lift coefficients tended to decrease with increasing Mach number. A key difference is that in the iced case, there was a

change from Ma = 0.12 to Ma = 0.21, unlike the clean case (cf. figures 20 and 21). Also in contrast to the clean case, the drag coefficients increased slightly between Ma = 0.12 to 0.21. Similar trends in the stalling behavior were observed for the quarter round located at x/c = 0.02 and 0.20, as shown in figures 39 and 40. The Mach number effects were largest for the x/c = 0.20 location.

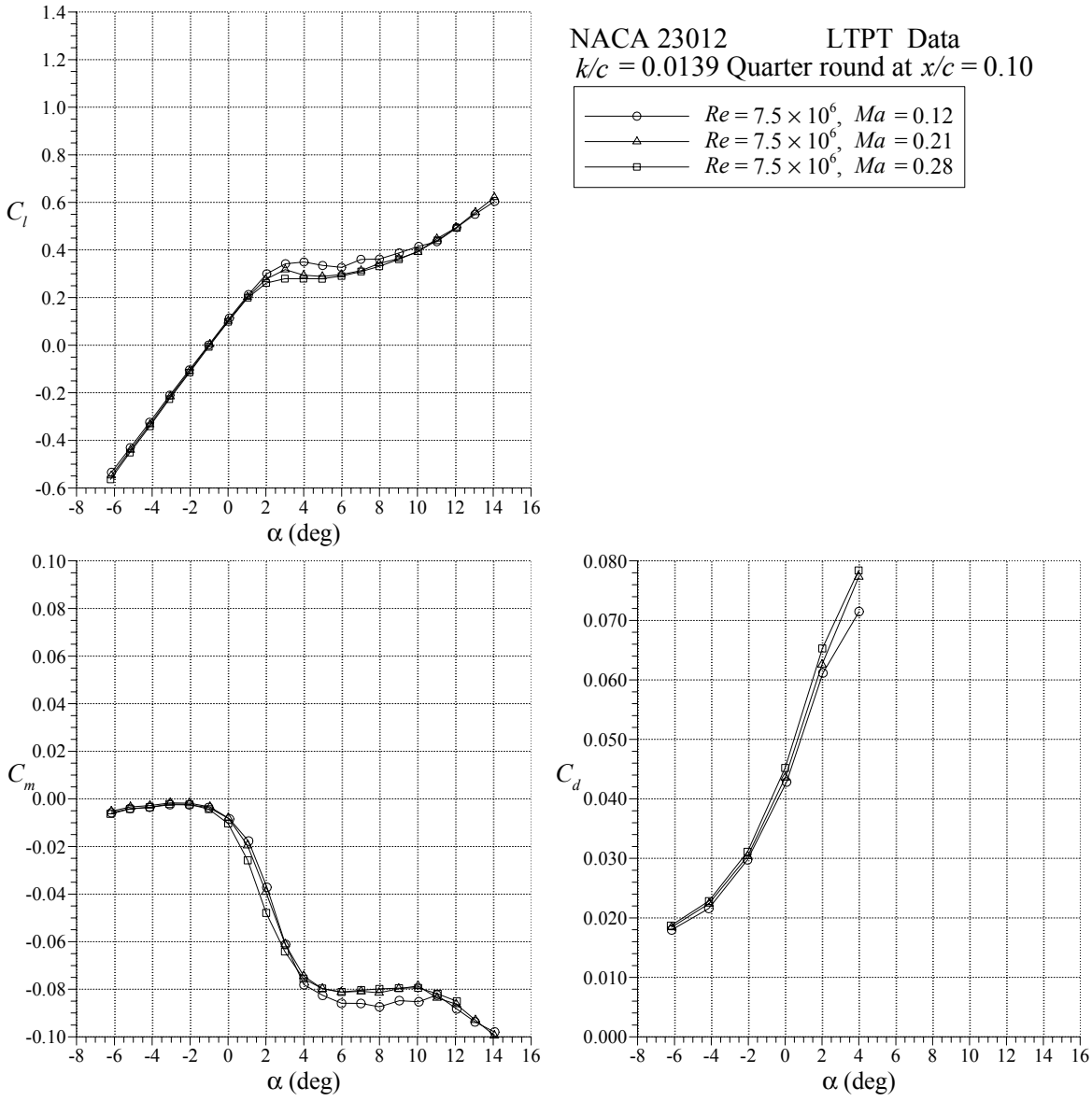

FIGURE 38. EFFECT OF MACH NUMBER ON NACA 23012 AIRFOIL PERFORMANCE WITH k/c = 0.0139 QUARTER ROUND AT x/c = 0.10

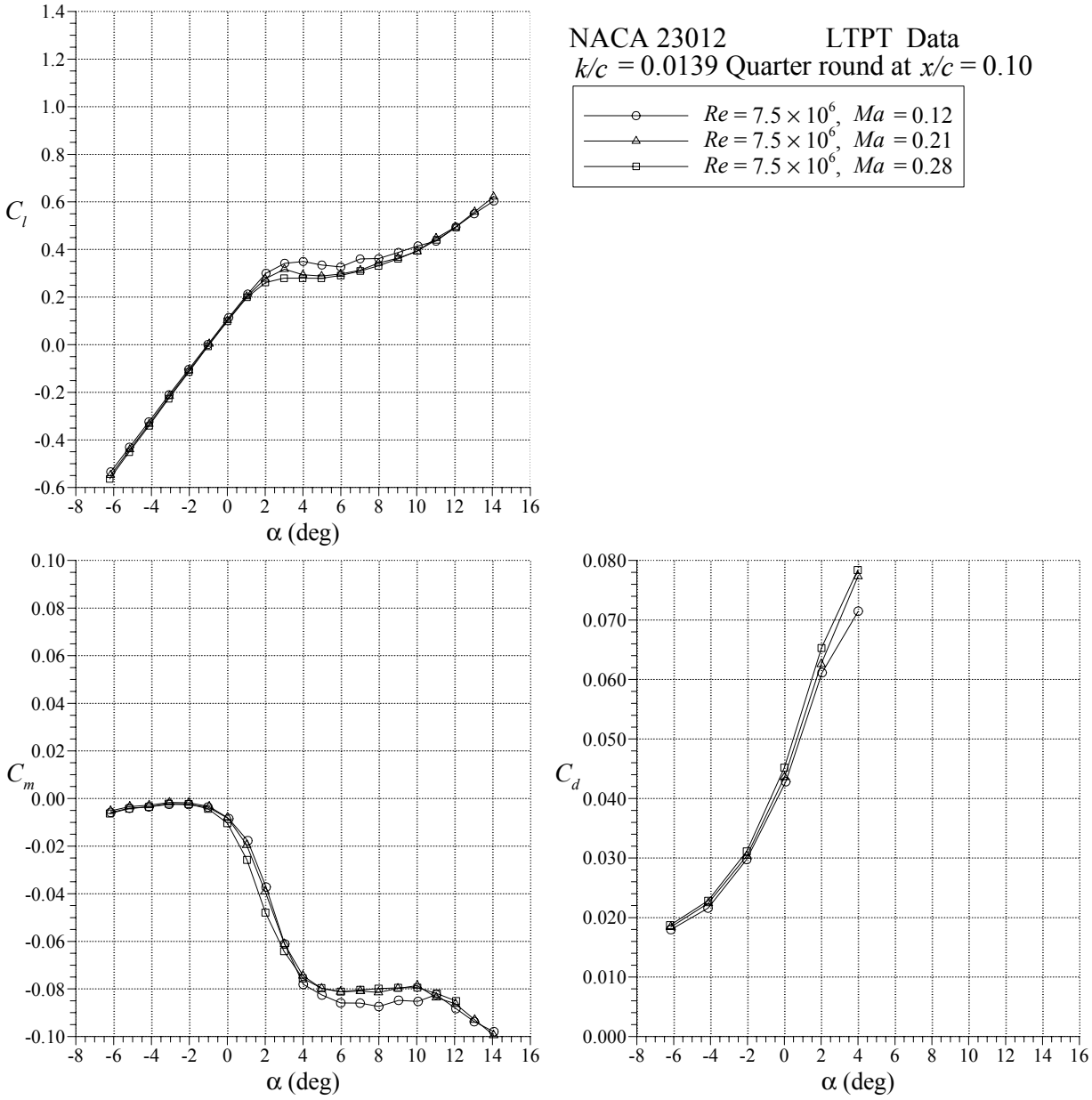

FIGURE 38. EFFECT OF MACH NUMBER ON NACA 23012 AIRFOIL PERFORMANCE WITH k/c = 0.0139 QUARTER ROUND AT x/c = 0.10 (Continued)

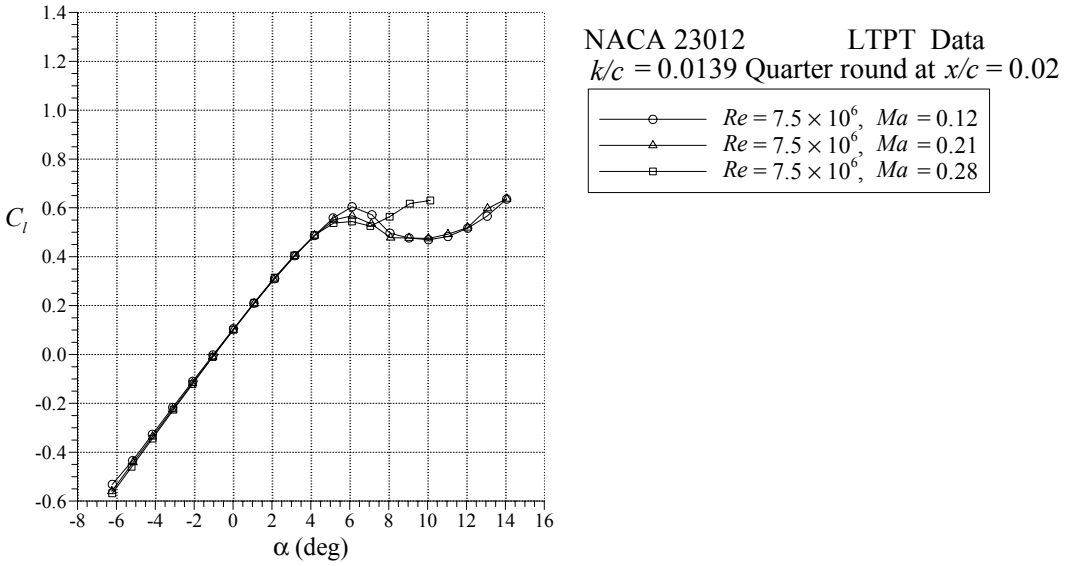

FIGURE 39. EFFECT OF MACH NUMBER ON NACA 23012 AIRFOIL PERFORMANCE WITH k/c = 0.0139 QUARTER ROUND AT x/c = 0.02

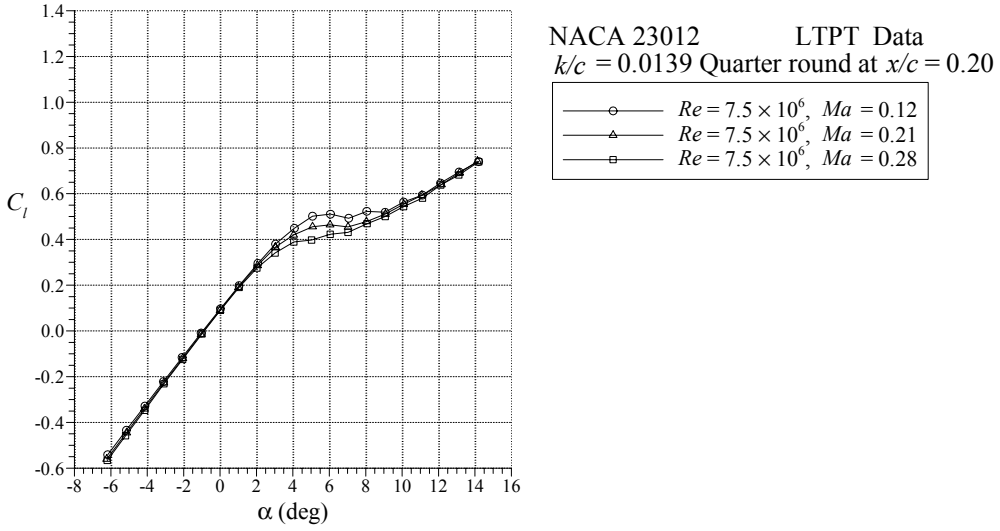

FIGURE 40. EFFECT OF MACH NUMBER ON NACA 23012 AIRFOIL PERFORMANCE WITH k/c = 0.0139 QUARTER ROUND AT x/c = 0.20

The relative importance of Mach number over Reynolds number in the stalling behavior of airfoils with ice shapes has been observed in previous studies. Trends very similar to these were reported by Broeren and Bragg [7] and Broeren, et al. [8] for the intercycle ice shape casting simulations tested on the NACA 23012 airfoil. Addy and Chung [24] tested glaze horn-type ice accretion simulations on an NLF-0414 airfoil and documented similar results. For three of the four iced airfoil configurations tested, there was virtually no variation in $C_{l,max}$ for $Re = 4.6\times10^6$ to 10.5×10^6 at a constant Mach number of 0.21. Likewise, the authors reported slight decreases in $C_{l,max}$ and α_{stall} with increasing Mach number (at $Re = 6.4\times10^6$) for all configurations tested.

Morgan, et al. [25] carried out iced airfoil performance measurements on a multielement supercritical airfoil. A large glaze ice simulation was tested on the airfoil in the cruise configuration (all elements nested) at a constant Mach number of 0.20 with $Re = 3.0\times10^6$ to 12×10^6. The results showed very minor changes in maximum lift over this range.

Determining the origins of this behavior is difficult, but some insight can be gained from the pressure distributions. Figure 41 shows the effect of Reynolds number on the pressure distribution for the NACA 23012 airfoil with the $k/c = 0.0139$ quarter round located at $x/c = 0.10$ and $\alpha = 2°$. The C_p's show the typical discontinuity at the quarter-round location, followed by the pressure plateau on the upper surface indicative of the separation bubble. The only minor difference is the pressure recovery region where the recovery was slightly longer for $Re = 3.5\times10^6$, perhaps indicative of a larger separation bubble. In contrast, figure 42 shows the Mach number dependence of analogous pressure distributions. The differences were much more discernible, particularly along the lower surface. In the pressure plateau region aft of the quarter round, the suction pressures were lower at the higher Mach number and the recovery extended farther downstream. These features in the pressure distributions were also similar to the LSWT results for the NACA 3415 airfoil presented in figure 31. These effects all contributed to the lower lift values observed at higher angles of attack, as the airfoil stalls. The reasons for this behavior are not clear from the present data.

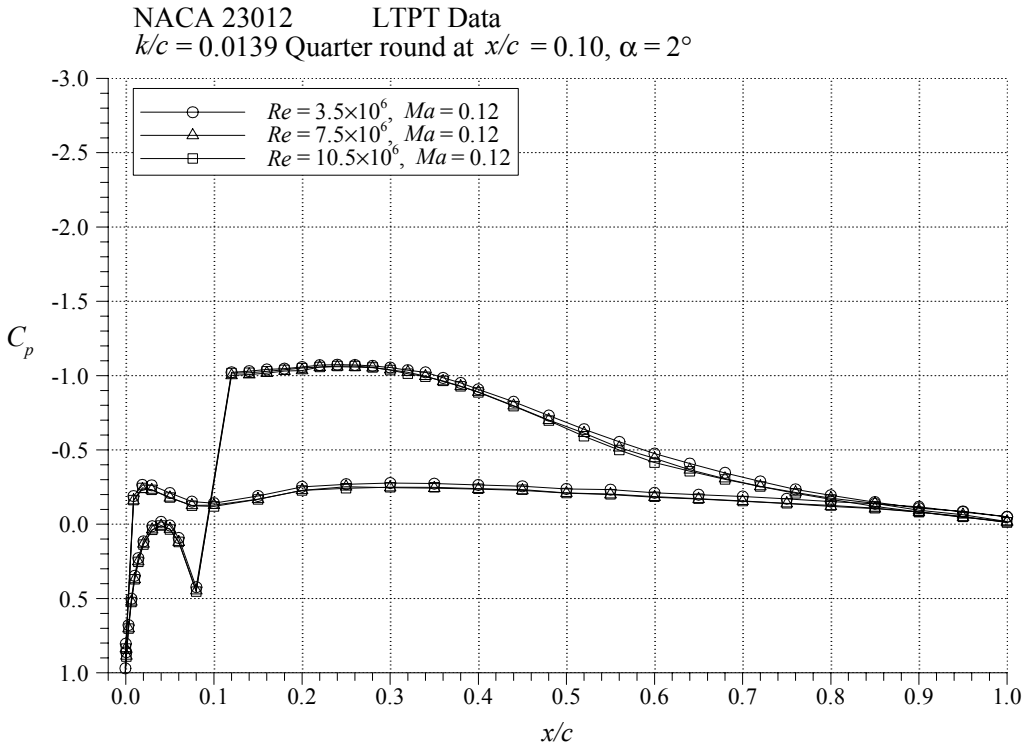

FIGURE 41. EFFECT OF REYNOLDS NUMBER ON NACA 23012 AIRFOIL PRESSURE DISTRIBUTION WITH $k/c = 0.0139$ QUARTER ROUND AT $x/c = 0.10$

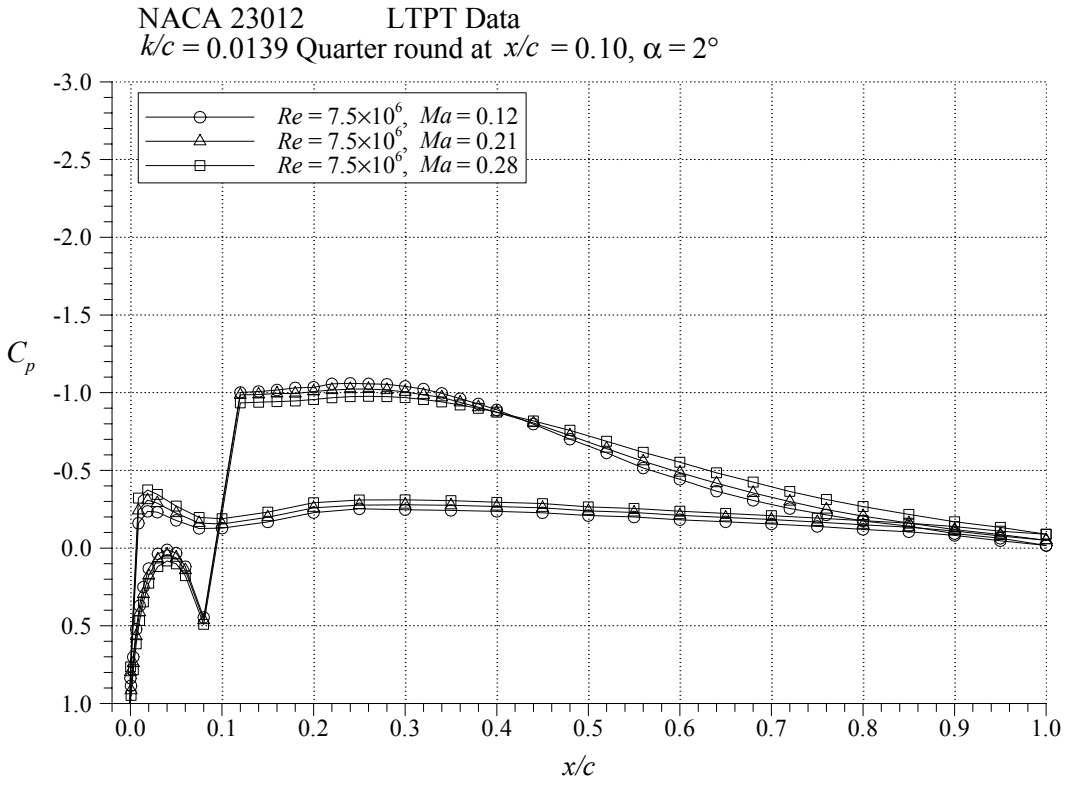

FIGURE 42. EFFECT OF MACH NUMBER ON NACA 23012 AIRFOIL PRESSURE DISTRIBUTION WITH k/c = 0.0139 QUARTER ROUND AT x/c = 0.10

These Reynolds and Mach numbers effects on the iced airfoil data become important when considering cross-facility comparisons. Given the data shown above, it is probably more important to closely match the Mach number instead of the Reynolds number, particularly in terms of lift characteristics at stall. This is illustrated in figures 43 and 44. The data in figure 43 exhibited Mach number trends in the lift (at stall), pitching moment, and drag coefficient that were identical to those described above for higher Reynolds numbers. The corresponding data from the Illinois LSWT are plotted in figure 44. Since this is an atmospheric tunnel, the Reynolds number and Mach number were controlled in proportion to one another. Here, the $C_{l,max}$ was higher for the lower Reynolds number. This seems like an apparent anomaly; however, given the data of figure 43, this was also an appropriate Mach number trend. Similar behavior was observed in the pitching moment. It is only in the drag where the lower Reynolds number tended to offset the Mach number effects.

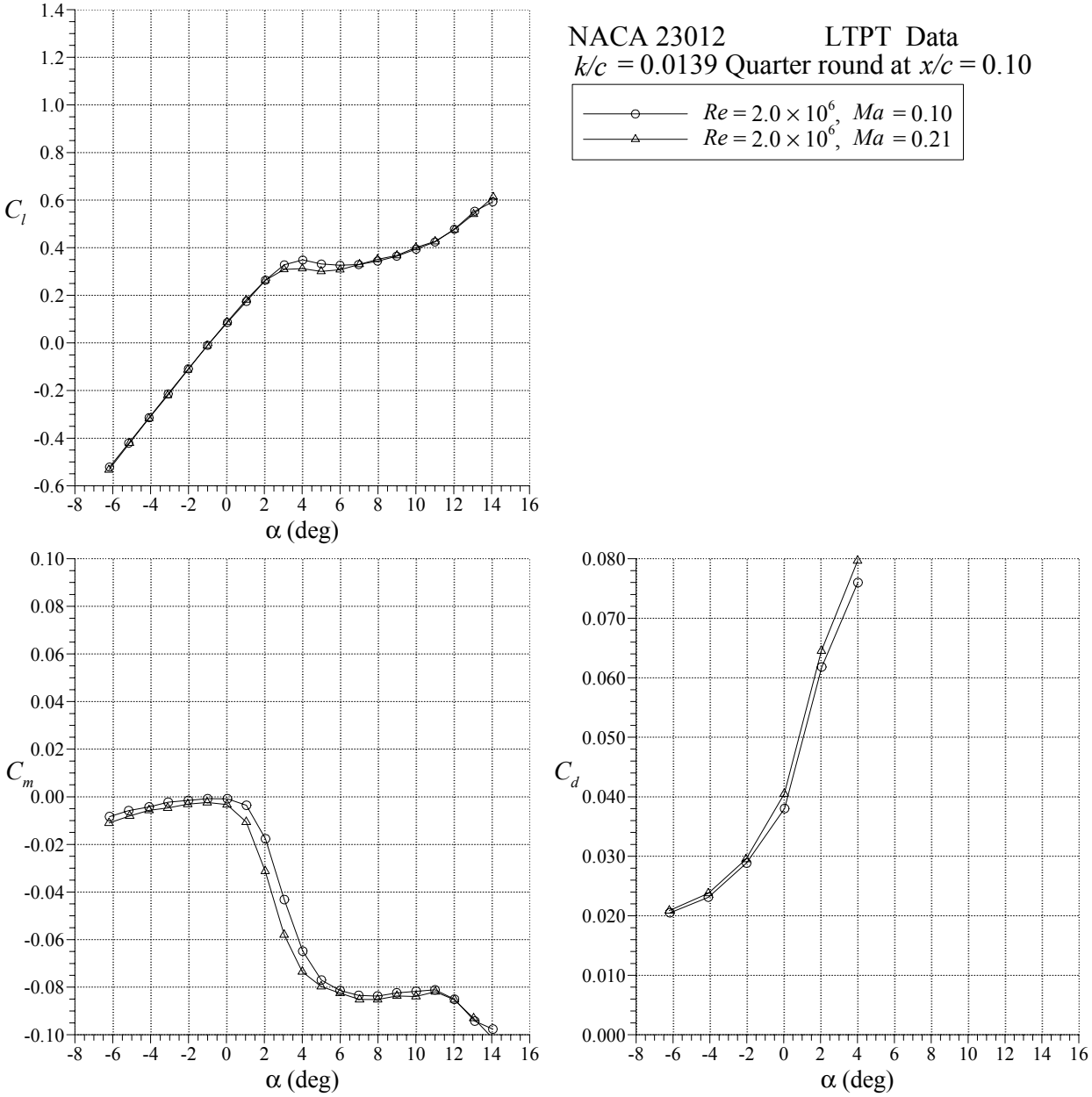

FIGURE 43. EFFECT OF MACH NUMBER (WITH $Re = 2.0 \times 10^6$) ON NACA 23012 AIRFOIL PERFORMANCE WITH $k/c = 0.0139$ QUARTER ROUND

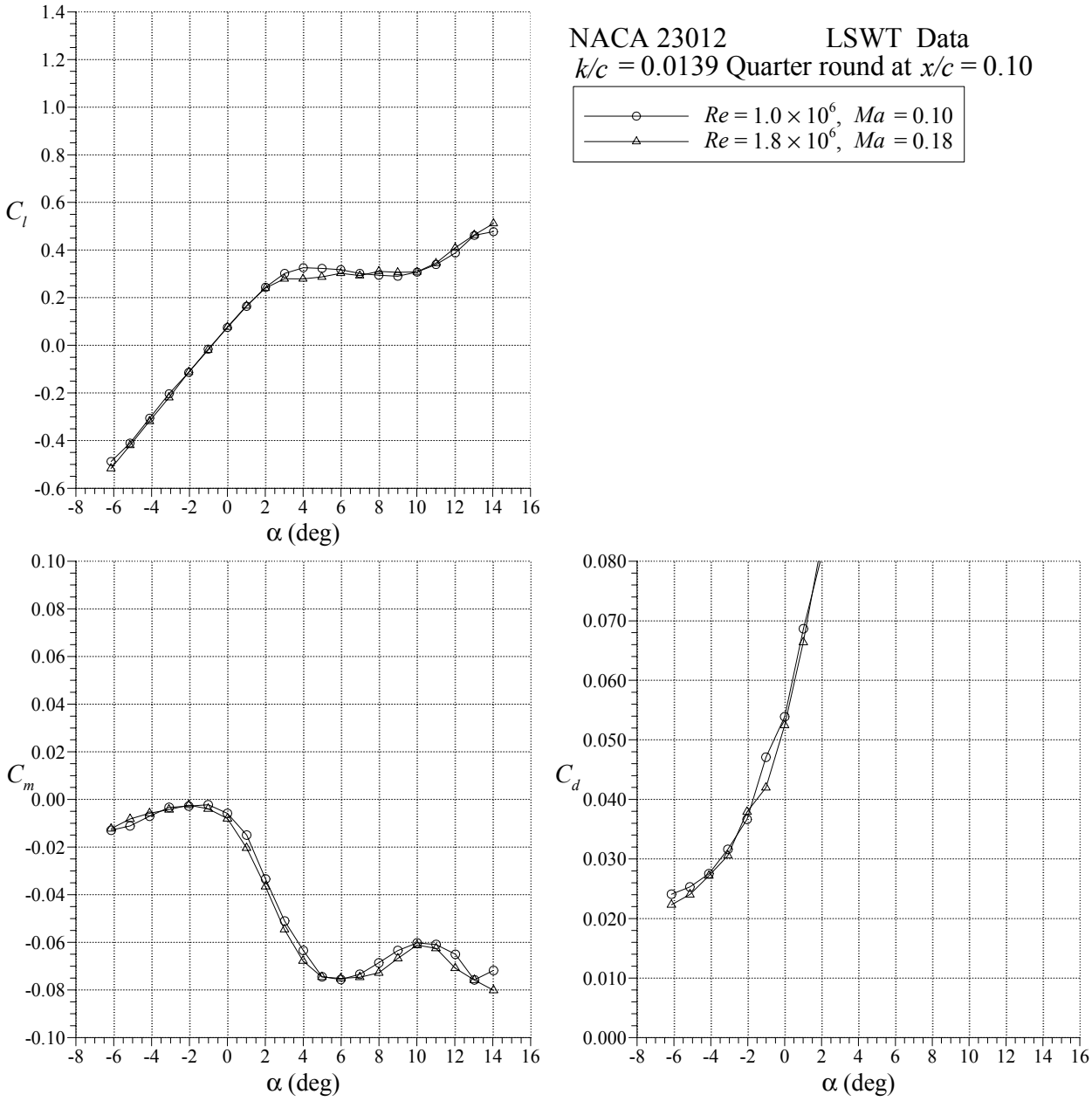

FIGURE 44. EFFECT OF REYNOLDS AND MACH NUMBERS ON NACA 23012 AIRFOIL PERFORMANCE WITH k/c = 0.0139 QUARTER ROUND

Direct comparisons of the LTPT and the LSWT results are shown in figures 45 to 47 for the SLD ridge-type ice simulations. Agreement between the facilities was probably the least favorable for the x/c = 0.10 location. As indicated in figure 45, the difference in $C_{l,max}$ was on the order of 0.05 or less in C_l. Also, the drag coefficients measured at the LSWT were much higher than at the LTPT. Much better cross-facility agreement in maximum lift coefficient was observed for the x/c = 0.02 and 0.20 locations, see figures 46 and 47, respectively. Better cross-facility agreement was also observed in the drag data.

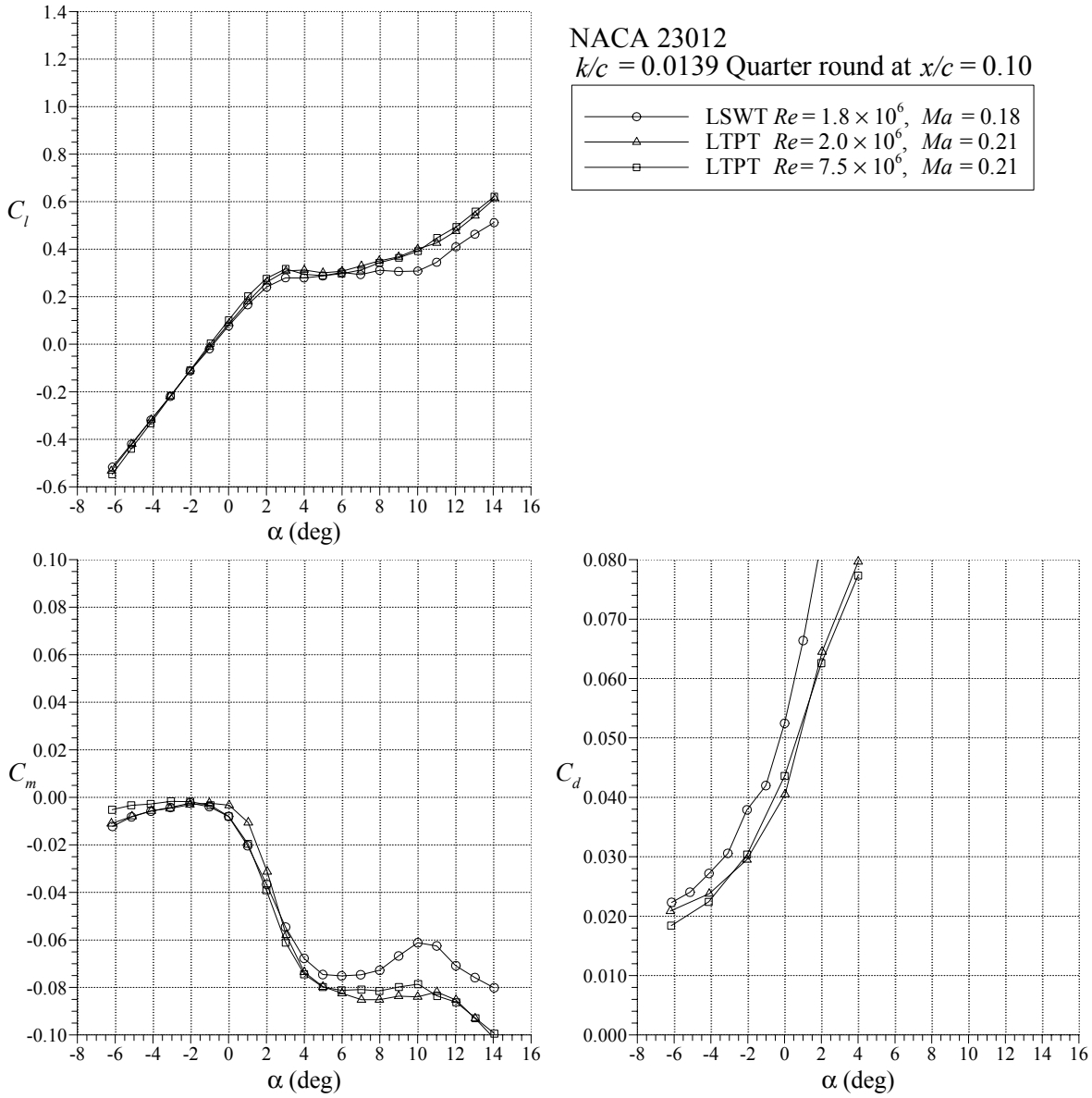

FIGURE 45. COMPARISON OF LTPT AND LSWT DATA FOR THE NACA 23012 AIRFOIL WITH k/c = 0.0139 QUARTER ROUND AT x/c = 0.10

The Reynolds and Mach numbers behavior of iced airfoils is significant in making detailed comparisons of the performance data. This has implications for understanding these effects in data from atmospheric tunnels. However, it is important to gauge these small differences against the much larger degradations in performance due to the presence of the ice shape itself. Given the reductions in maximum lift shown here, the changes due to Reynolds and Mach numbers on the iced airfoil are surely of secondary (or lower) importance. For example, in figure 45 the variation in $C_{l,max}$ measured in two different facilities over a large Reynolds number difference was about 0.05. However, the overall decrease in $C_{l,max}$ from the clean value (of 1.5 for $Re = 2.0\times10^6$ and $Ma = 0.21$) was about 1.2.

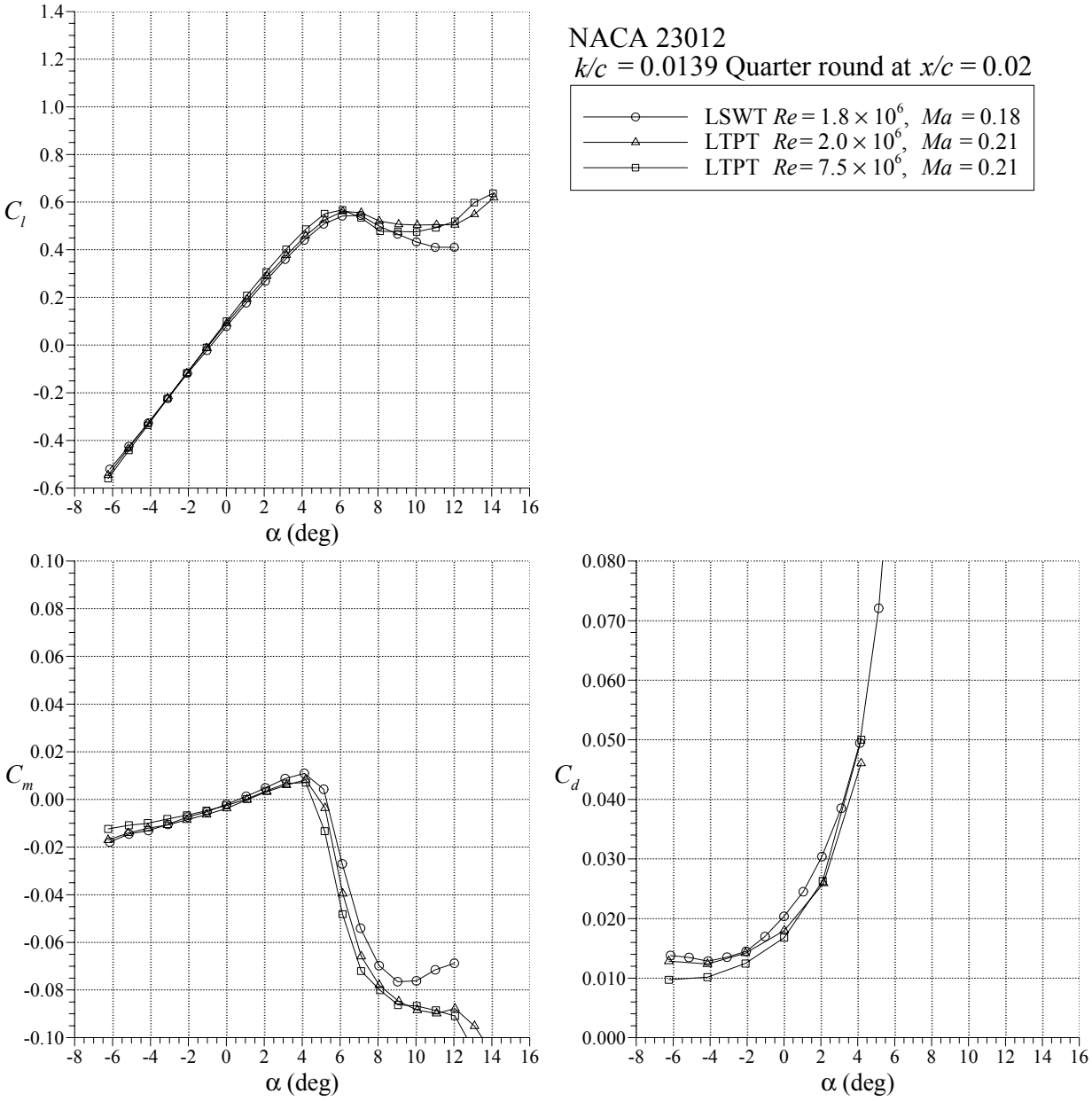

FIGURE 46. COMPARISON OF LTPT AND LSWT DATA FOR THE NACA 23012 AIRFOIL WITH k/c = 0.0139 QUARTER ROUND AT x/c = 0.02

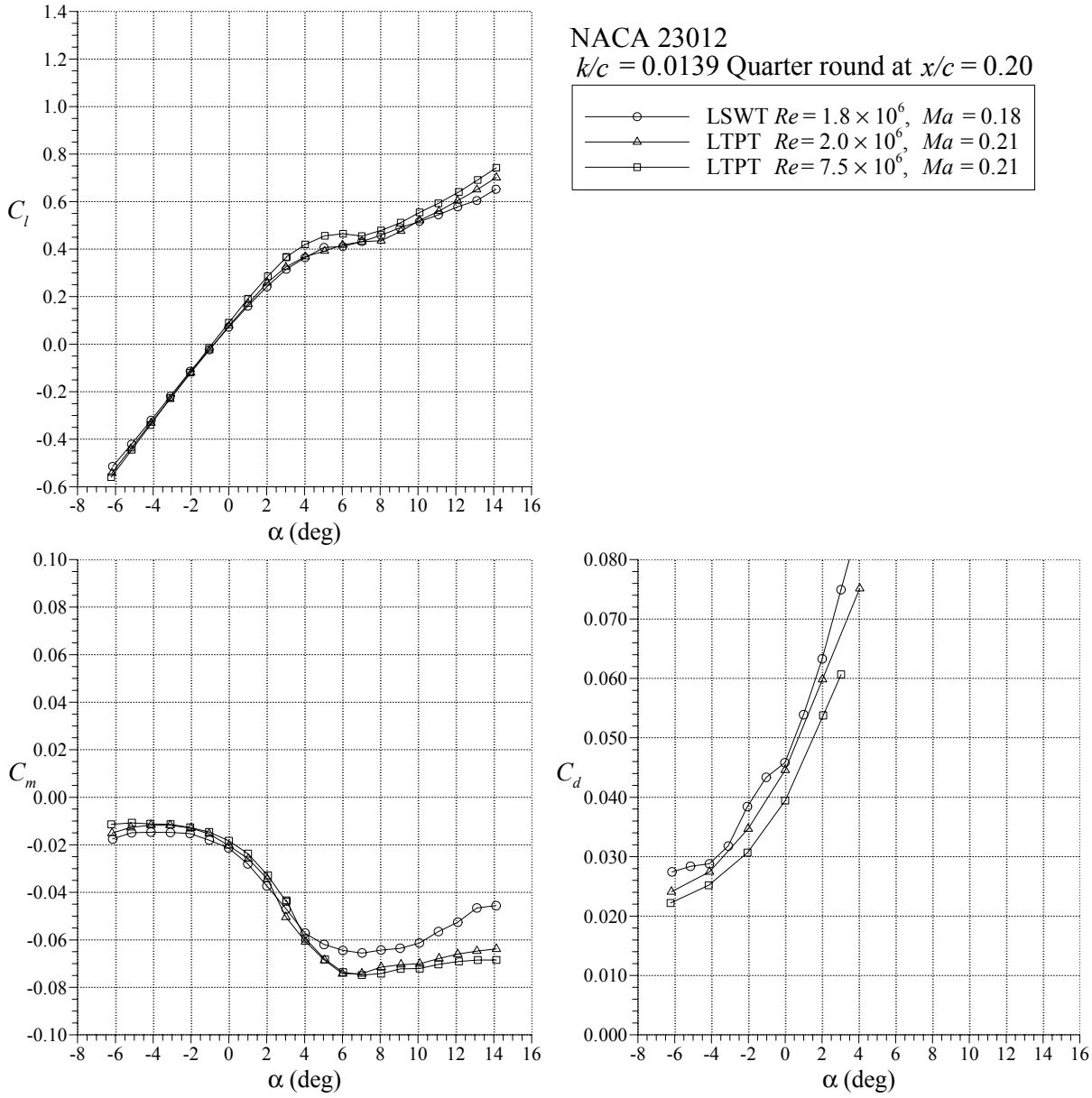

FIGURE 47. COMPARISON OF LTPT AND LSWT DATA FOR THE NACA 23012 AIRFOIL WITH k/c = 0.0139 QUARTER ROUND AT x/c = 0.20

4.3 INTERCYCLE ICE ACCRETIONS.

4.3.1 Comparison of LTPT and LSWT Results.

The LTPT experiments with intercycle ice shape castings on the NACA 23012 served as a benchmark for the roughness simulations used at the LSWT. The ice shape castings were considered the highest-fidelity simulation feasible for aerodynamic testing in a dry tunnel. On the other hand, the scaled-down, built-up roughness simulations were low fidelity by this standard. The results, however, were promising.

The effect of intercycle ice on the NACA 23012 airfoil performance, taken from Broeren and Bragg [7] and Broeren, et al. [8], is shown in figure 48. Ice shape castings 290, 296, and 312 lowered the $C_{l,max}$ to about 0.70 (0.65 to 0.75), which caused significant changes in the pitching moment dependence upon angle of attack and caused large increases in drag. Ice shape 322, which was smoother and smaller than the others, still lowered the maximum lift coefficient to about 0.90. The built-up roughness simulations of the intercycle ice shapes tested on the 18-inch chord NACA 23012 airfoil resulted in similar performance effects. These data are summarized in figure 49 and show that the built-up roughness method was acceptable in terms of replicating the performance of the ice shape casting method, at least for the purposes of this investigation. The most significant differences between figures 48 and 49 were in the clean data, which were due to Reynolds number effects (note that the Mach number is closely matched). The $C_{l,max}$ and α_{stall} data for the ice shape cases were very similar between the experiments. A detailed comparison for ice shape 296 is shown in figure 50. Data from the LTPT is shown for two different conditions, one that closely matches the LSWT Reynolds number of 1.8×10^6, the other that closely matches the LSWT Mach number of 0.18. The lift coefficient data shows that the LSWT data matched the higher Mach number LTPT data better, in spite of the large Reynolds number difference. This agreement is particularly evident in the range of $0.50 \le C_l \le 0.70$. While this is consistent with the previous discussion of Reynolds and Mach numbers effects, it may be merely coincidental because of the differences in the simulation methods. Comparison plots for the other three intercycle ice shapes showed a similar level of agreement between the LSWT and the LTPT results.

Uniformly distributed roughness in the form of 40- and 80-grit sandpaper was also tested on the 36-inch chord LTPT model. These results (in figure 51) show that while this roughness did have a significant effect on the performance, it was much less severe than for the intercycle ice. The maximum lift values were lowered to about 1.2 (1.15 to 1.25) by the sandpaper. Equivalent sized sandpaper roughness was tested on the 18-inch chord airfoil model in the LSWT. As mentioned in section 3.3.2, 80- and 150-grit sizes were the approximate scale equivalent of 40- and 80-grit paper. These data (in figure 52) show a similar trend, where the sandpaper caused the maximum lift to be reduced to about 1.10 to 1.15. A detailed comparison for the 80- and 40-grit case is shown in figure 53. Data from the LTPT is shown for two different conditions; one that closely matches the LSWT Reynolds number of 1.8×10^6 and the other that closely matches the LSWT Mach number of 0.18. These data show excellent agreement between the LSWT and the LTPT for the lift and pitching moment at closely matched Reynolds numbers. The drag coefficient values were also very close, except for small angles of attack. The data show a larger Reynolds number effect than for the intercycle ice shape cases. These Reynolds and Mach numbers effects on the LTPT data were presented and discussed in references 7 and 8. Similar comparisons were observed for the 150- and 80-grit sandpaper results. These data indicate that the simple chordwise scaling of roughness heights can work fairly well for this type of roughness.

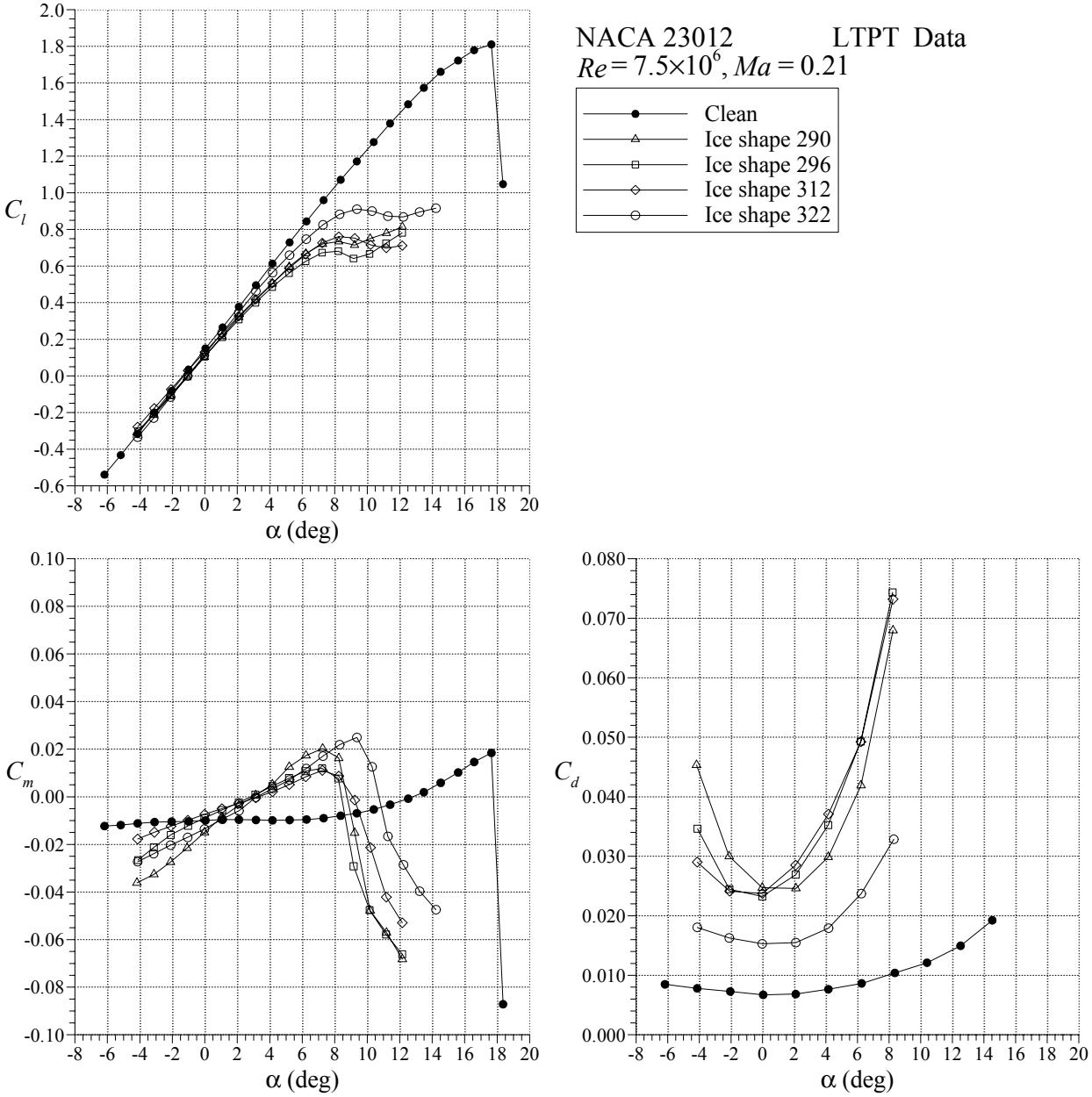

FIGURE 48. EFFECT OF INTERCYCLE ICE CASTING SIMULATIONS ON NACA 23012 AIRFOIL PERFORMANCE

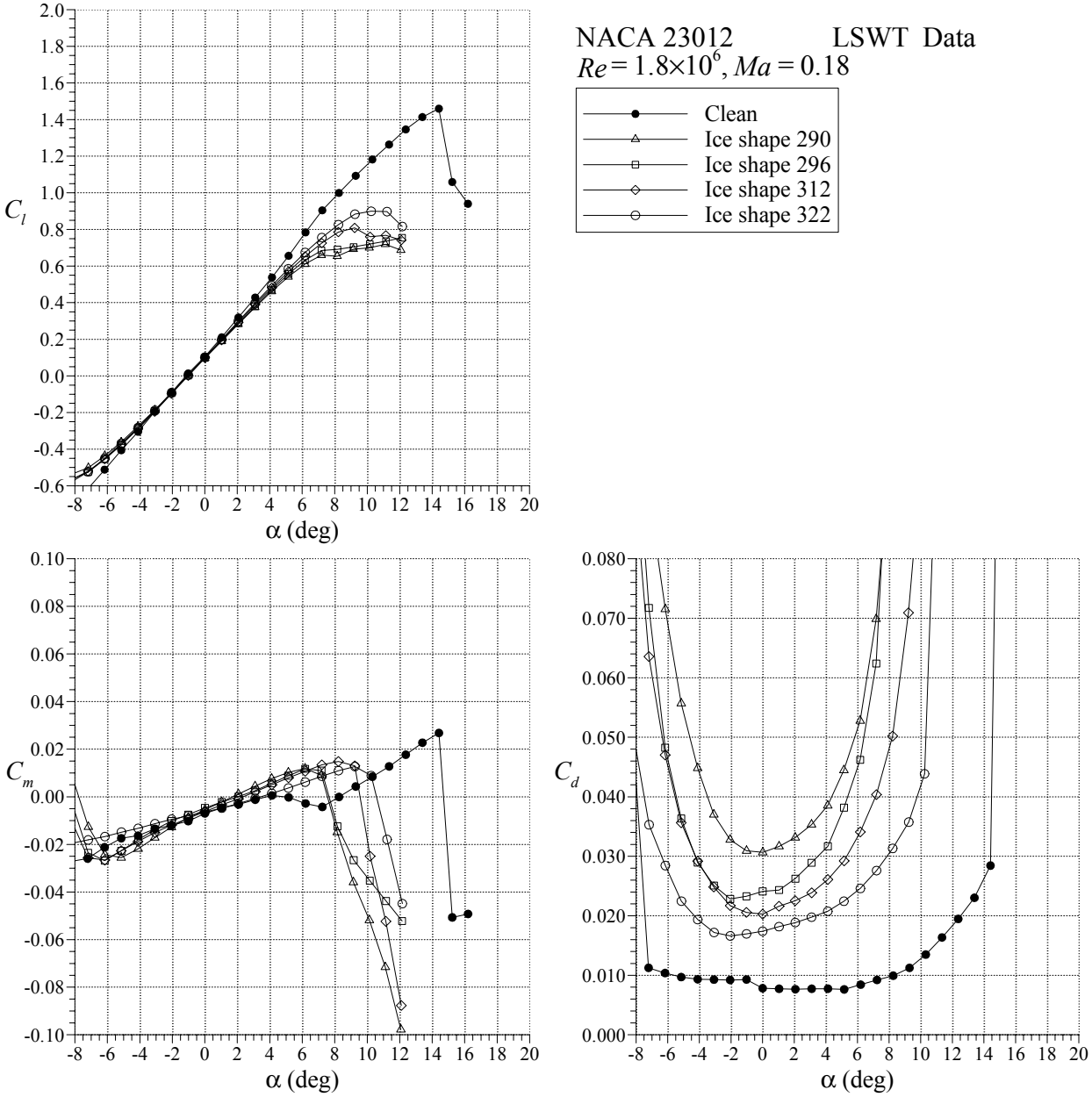

FIGURE 49. EFFECT OF BUILT-UP ROUGHNESS SIMULATIONS OF INTERCYCLE ICE ON NACA 23012 AIRFOIL PERFORMANCE

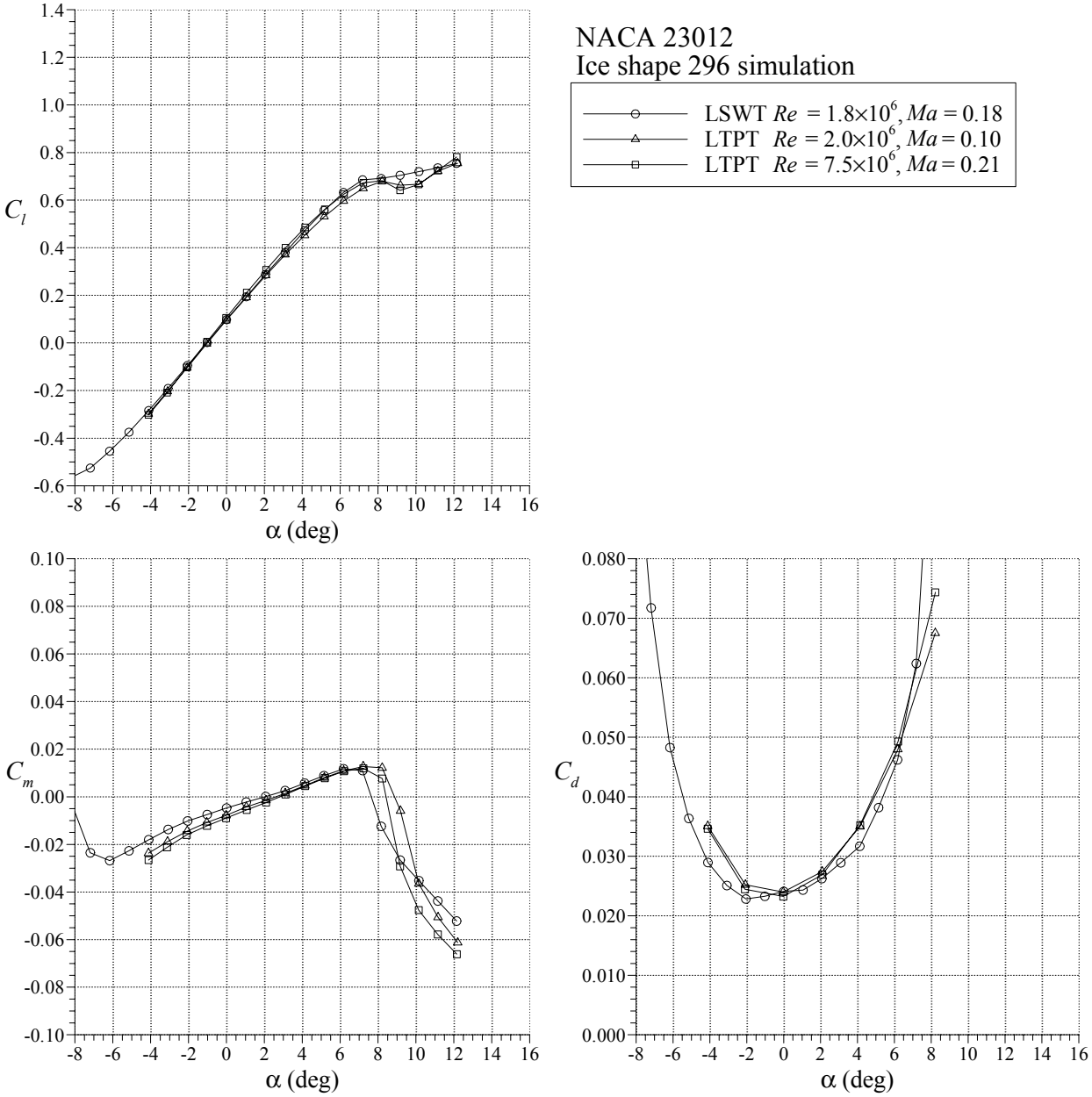

FIGURE 50. COMPARISON OF LTPT AND LSWT DATA FOR THE NACA 23012 AIRFOIL WITH INTERCYCLE ICE SIMULATIONS

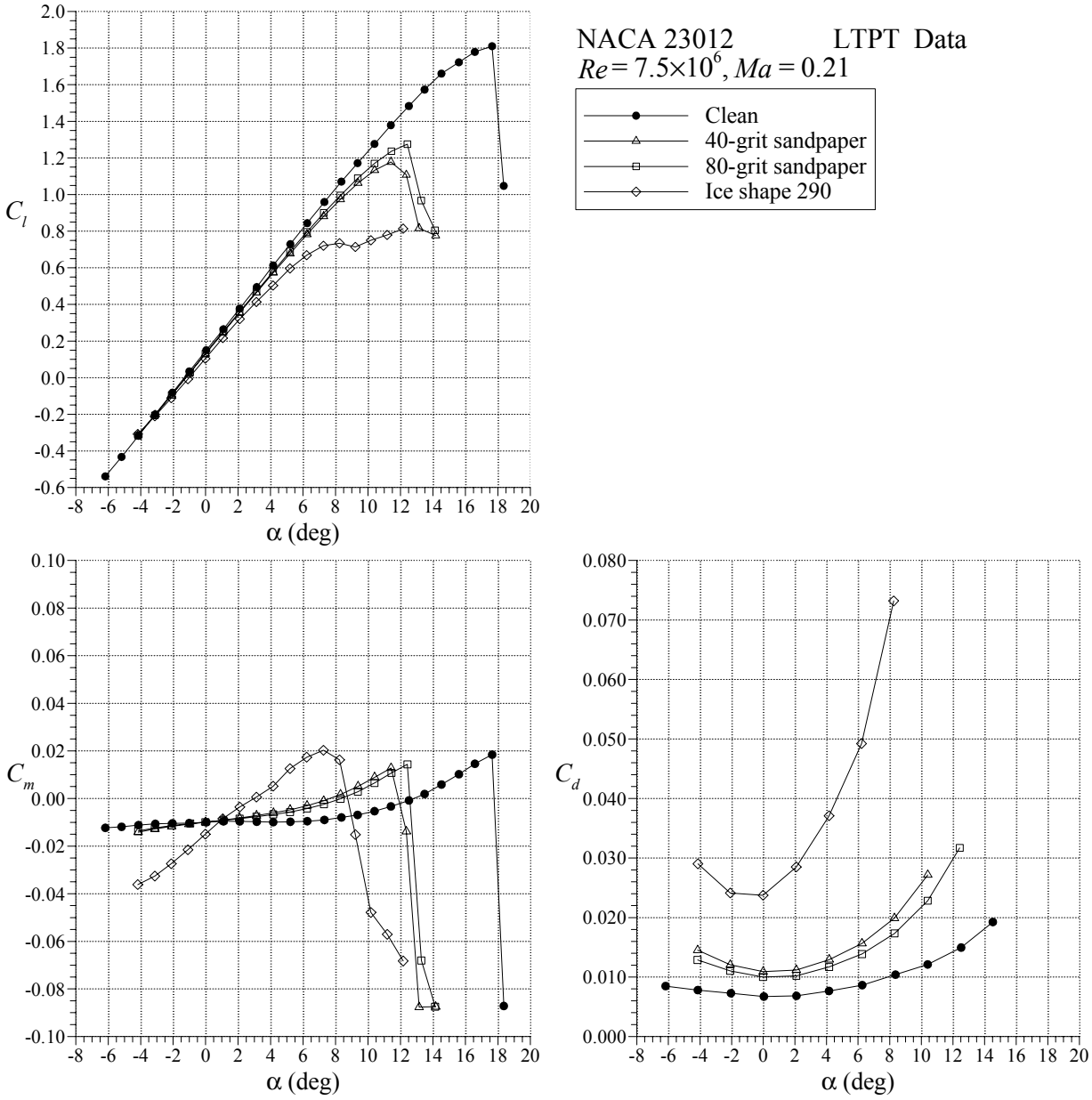

FIGURE 51. EFFECT OF SANDPAPER ROUGHNESS ON NACA 23012 AIRFOIL PERFORMANCE AT LTPT

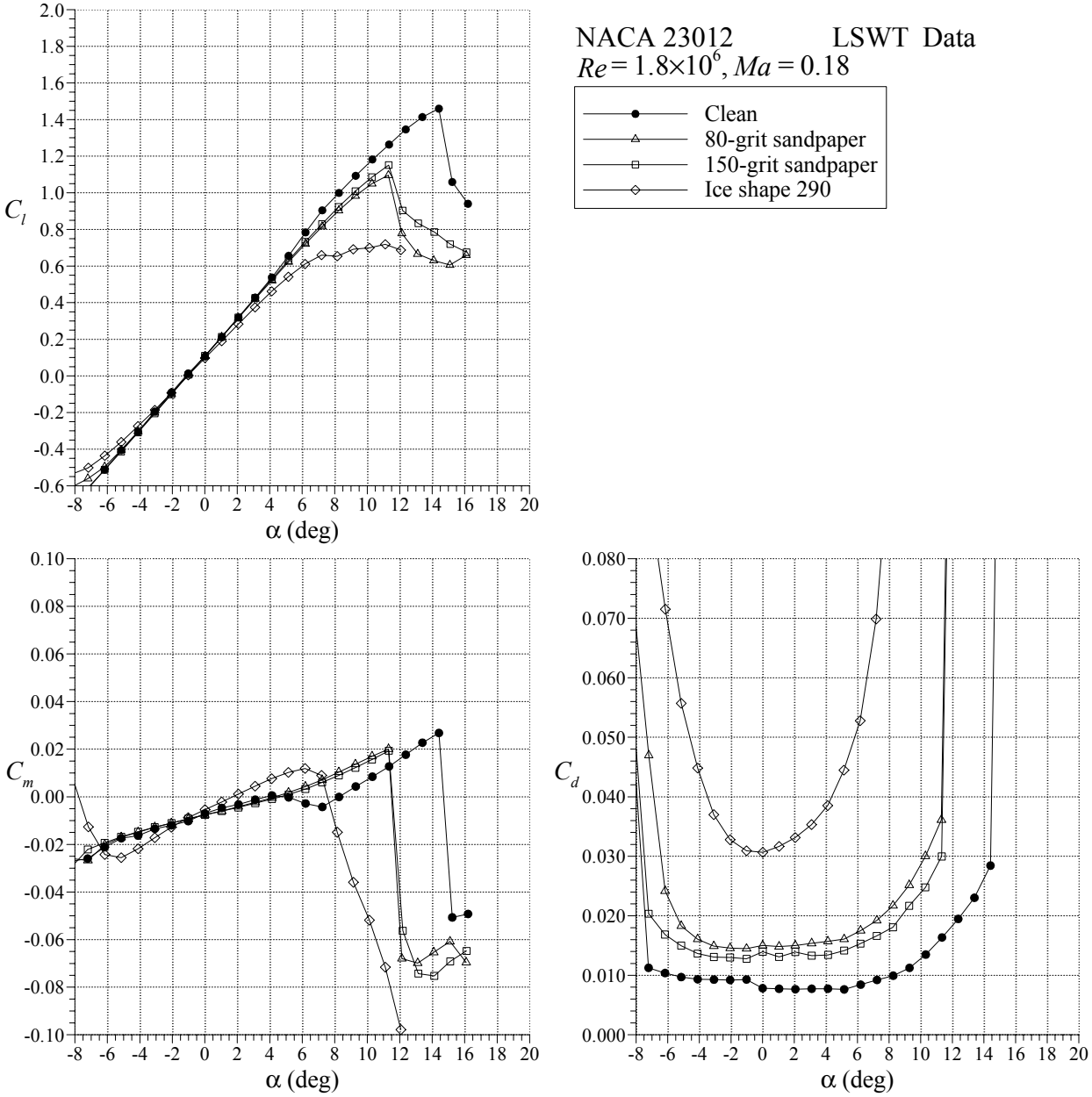

FIGURE 52. EFFECT OF SANDPAPER ROUGHNESS ON NACA 23012 AIRFOIL PERFORMANCE AT LSWT

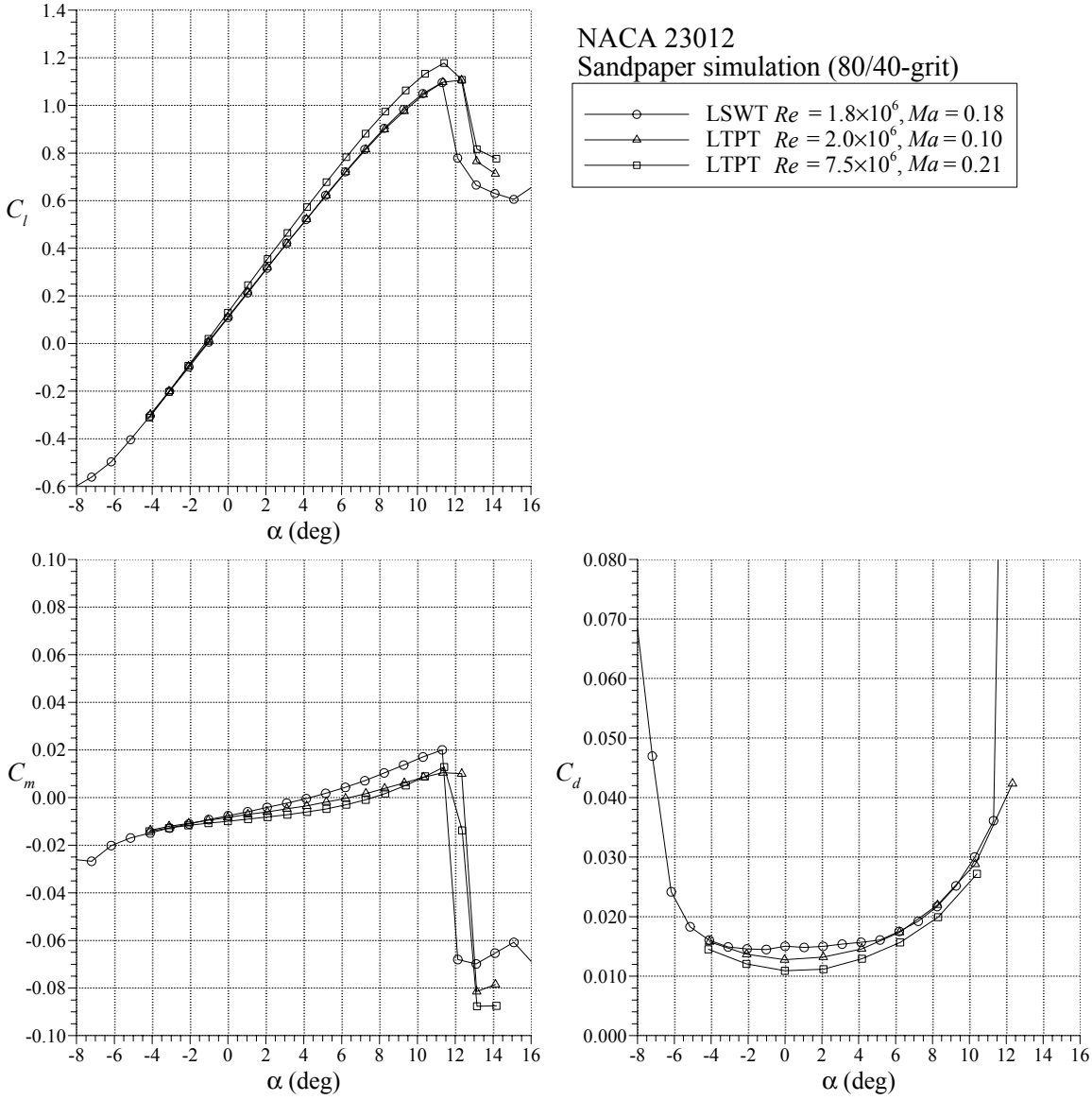

FIGURE 53. COMPARISON OF LTPT AND LSWT DATA FOR THE NACA 23012 AIRFOIL WITH SANDPAPER ROUGHNESS

4.3.2 Airfoil Geometry Effects.

The intercycle ice roughness simulations were tested on the NLF 0414 and NACA 3415 airfoils to gauge their sensitivity to this class of ice shape. Significant changes in performance were also observed. The results for the NLF 0414 airfoil are shown in figure 54. The stall behavior with the ice simulations was similar to the NACA 23012 data (cf. figure 49) in that there was a fairly large range of $C_{l,max}$ from about 0.90 to 1.05. The same ice shape (322) also resulted in the highest $C_{l,max}$. These iced airfoil lift coefficients were significantly higher than the range for the ice shapes on the NACA 23012 airfoil, which was 0.65 to 0.90. A key difference in lift performance with the ice simulations between the two airfoils was observed for coefficients in the range of 0.0 to 0.6, in terms of a reduction in lift curve slope. In this range, the simulated ice

had a more severe effect for the NLF 0414 airfoil than for the NACA 23012 because there were larger differences between the clean and iced lift coefficients. The effects on pitching moment and drag were also similar to the effects on the NACA 23012 airfoil.

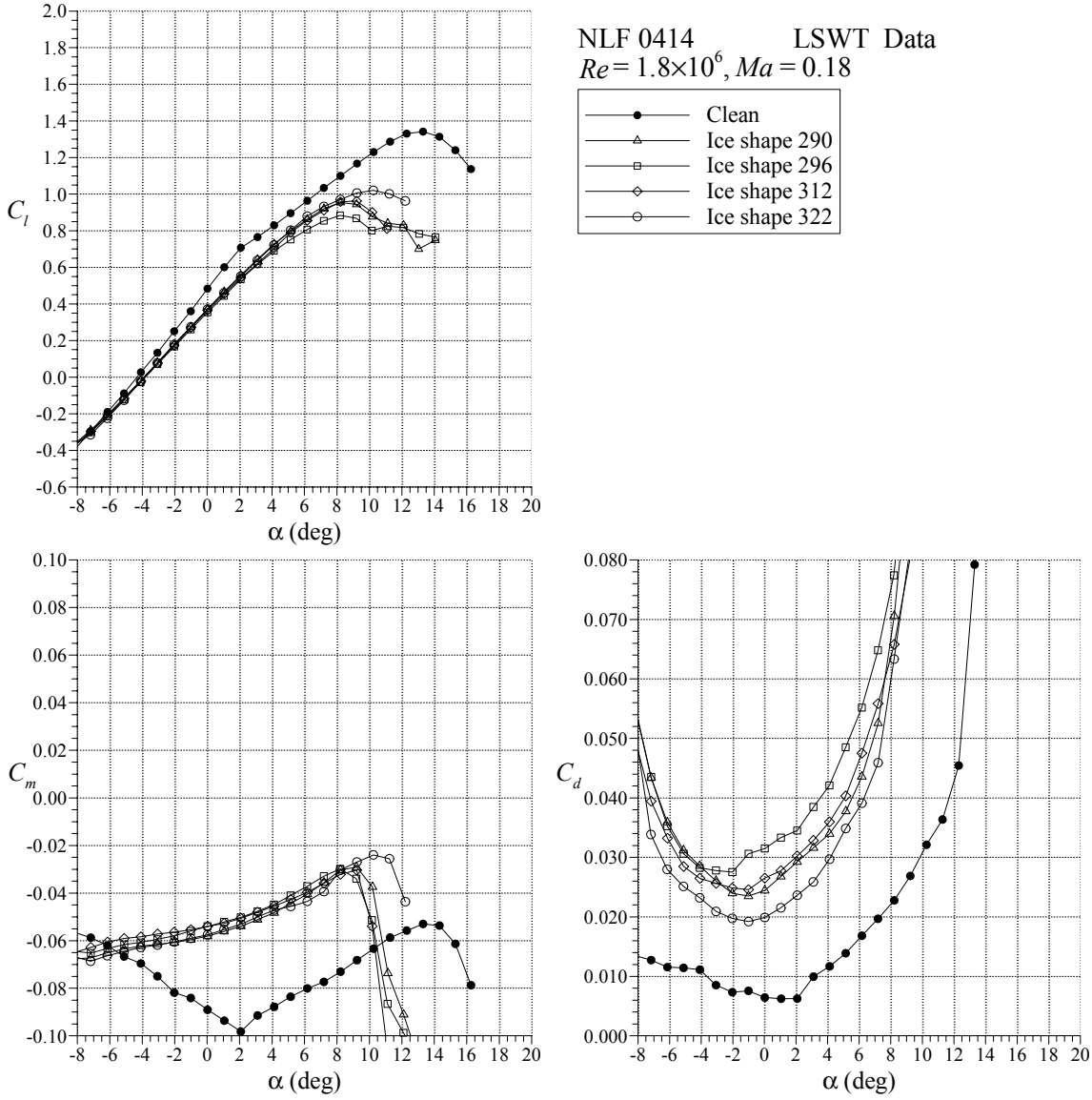

FIGURE 54. EFFECT OF BUILT-UP ROUGHNESS INTERCYCLE ICE SIMULATIONS ON NLF 0414 AIRFOIL PERFORMANCE

The performance of the NACA 3415 airfoil with the intercycle ice simulations (figure 55) was similar to the NLF 0414 airfoil. In this case, there was less variation in maximum lift with the different ice shapes. The $C_{l,max}$ values ranged from about 0.85 to 0.95. These were slightly higher than the NACA 23012 airfoil, but slightly lower than the NLF 0414 airfoil. The lift penalties caused by the ice shapes for the NACA 3415 airfoil were similar to the NLF 0414 airfoil in the range of C_l = 0.0 to 0.6, with the ice resulting in reduced lift curve slope. The effects on pitching moment and drag were also similar to the other airfoils.

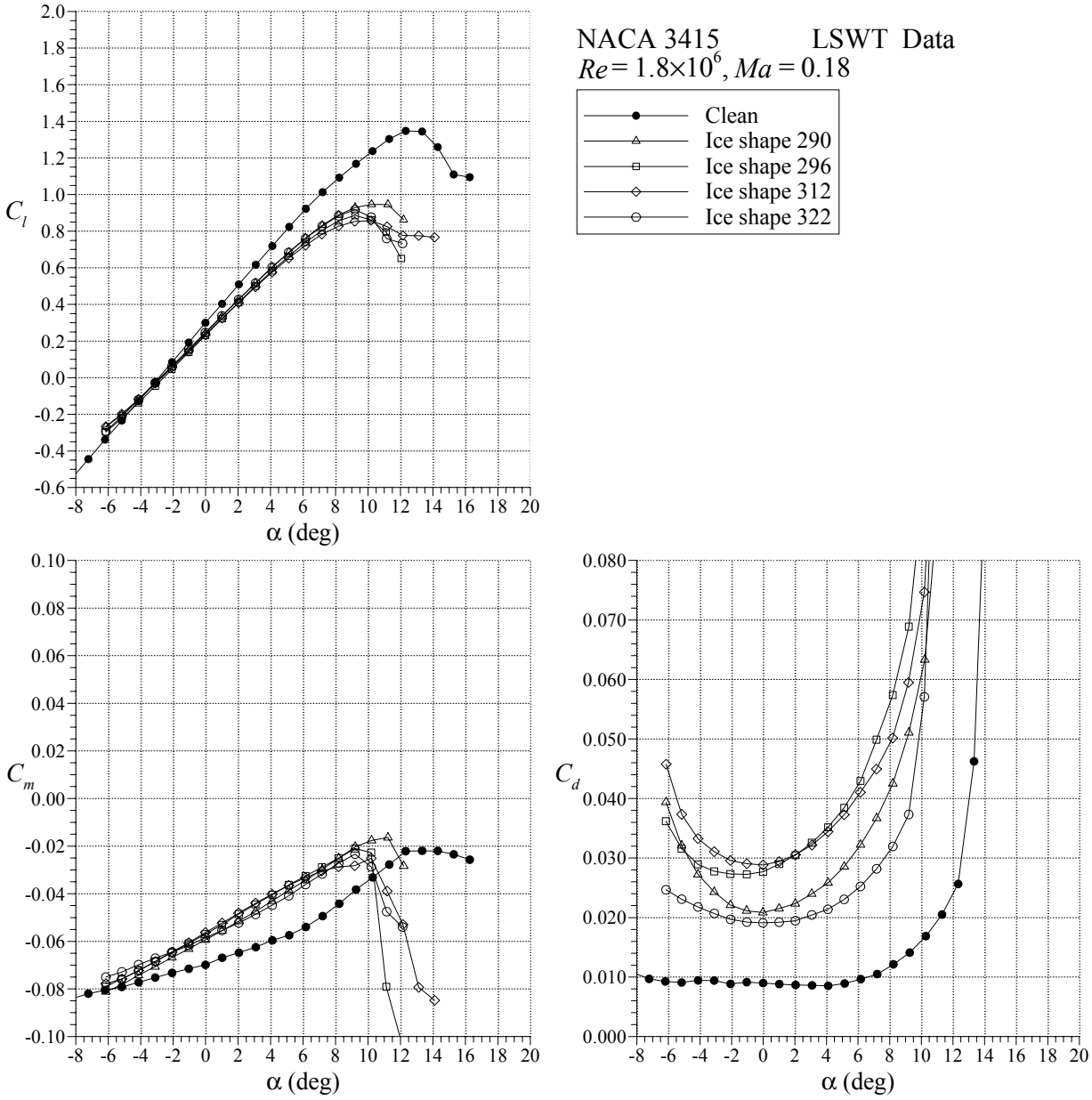

FIGURE 55. EFFECT OF BUILT-UP ROUGHNESS INTERCYCLE ICE SIMULATIONS ON NACA 3415 AIRFOIL PERFORMANCE

The NLF 0414 and the NACA 3415 airfoils were also tested with 80- and 150-grit sandpaper applied to the leading edge. These results are shown figures 56 and 57. The uniform roughness had a very small effect on $C_{l,max}$ for the NLF 0414 airfoil, which was lowered to a value in the range of 1.20 to 1.25. This was higher than the NACA 23012 airfoil, which was lowered to a range of 1.10 to 1.15 (cf. figure 52). The stall characteristics of the NLF 0414 airfoil were also changed by the presence of the sandpaper because there was an abrupt decrease in lift beyond $C_{l,max}$. This change in stall characteristics from the clean case was not observed for the other two airfoils. The $C_{l,max}$ values for the NACA 3415 airfoil with the uniform roughness were 1.05 to 1.10 and were closer to the NACA 23012 airfoil. However, the NACA 23012 had a higher clean

maximum lift coefficient, so the actual degradation for this airfoil was larger. The effect of the sandpaper roughness on the pitching moment and drag for the NLF 0414 and the NACA 3415 airfoils was similar to the NACA 23012.

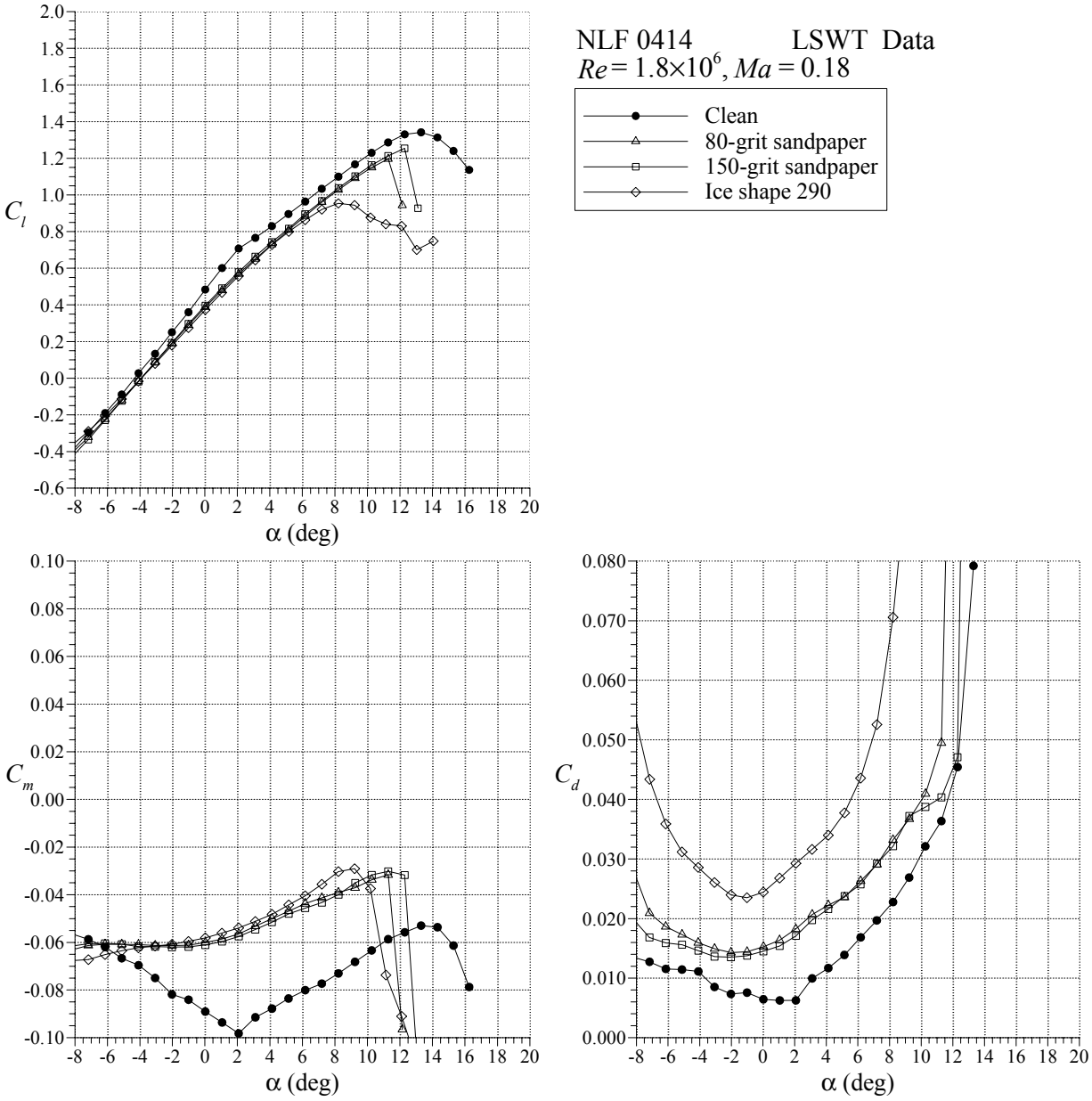

FIGURE 56. EFFECT OF SANDPAPER ROUGHNESS ON NLF 0414 AIRFOIL PERFORMANCE

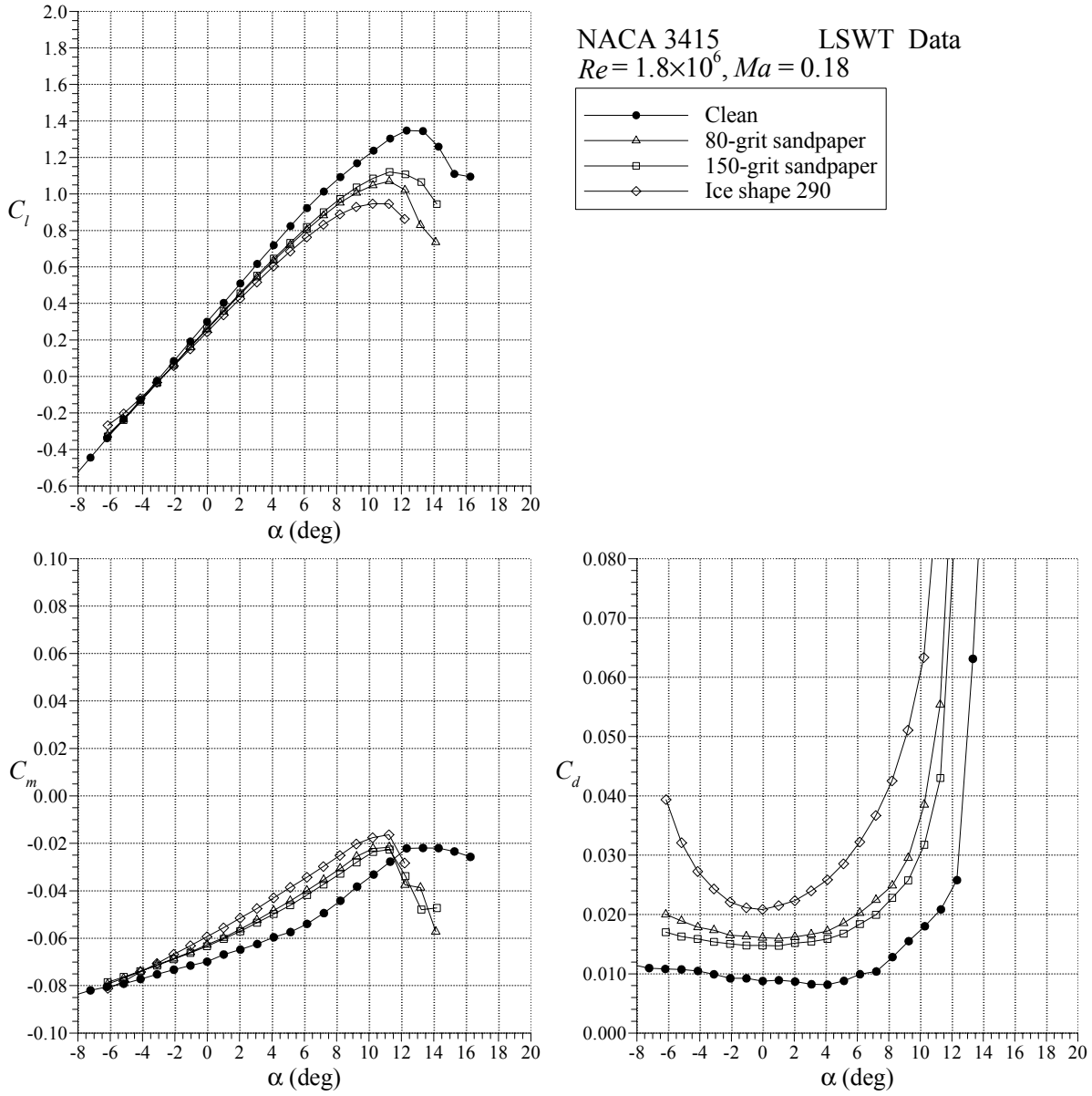

FIGURE 57. EFFECT OF SANDPAPER ROUGHNESS ON NACA 3415 AIRFOIL PERFORMANCE

The effect of the intercycle ice simulations on maximum lift is summarized in figure 58 for the three airfoils tested. The chart illustrates the conclusions stated above, that the intercycle ice simulations had a more severe effect on $C_{l,max}$ for the NACA 23012 airfoil. The effects for the NACA 3415 and the NLF 0414 airfoils were similar and less severe. A key feature of some of the intercycle ice simulations was a large spanwise-running ridge. This ice ridge was similar to the SLD simulation, except that there were spanwise breaks or gaps in the ridge-like features. However, the effect on airfoil performance was analogous to that reported for the quarter-round shapes. Referring to figure 33, quarter-round shapes located at $x/c = 0.0$ to $x/c = 0.06$ resulted in a higher $C_{l,max}$ penalty for the NACA 23012m. These values were in the range of 1.00 to 0.30 compared to 1.05 to 0.75 for the NLF 0414 airfoil and 1.15 to 0.65 for the NACA 3415 airfoil.

This range of x/c also corresponded to the range of locations for large ridge-like roughness features in the intercycle ice accretions. The fact that the $C_{l,max}$ values with the intercycle ice simulations are higher than the quarter-round shape was likely due to the spanwise variation in the ridge-like features of the former. Also, these features were generally smaller than the $k/c = 0.0139$ quarter-round height.

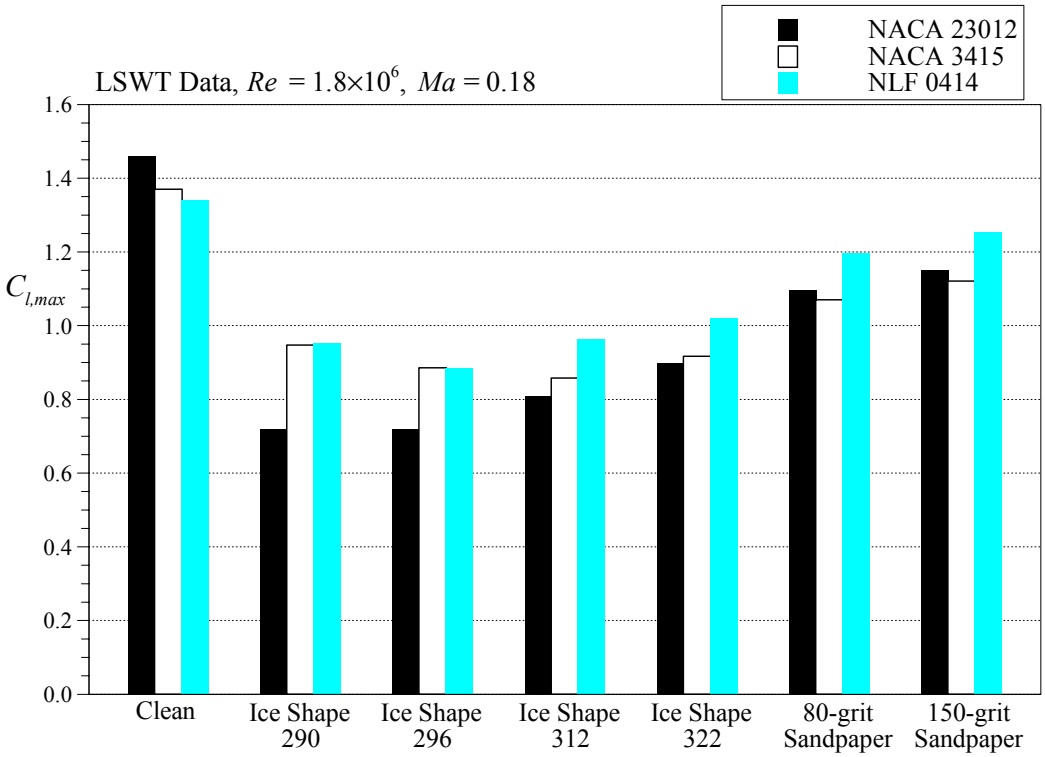

FIGURE 58. EFFECT OF INTERCYCLE ICE SIMULATIONS AND SANDPAPER ROUGHNESS ON $C_{l,max}$ FOR THE THREE AIRFOILS TESTED AT LSWT

It was also noted above that the intercycle ice simulations resulted in more severe lift penalties for the NACA 3415 and the NLF 0414 airfoils in the range of $C_l = 0.0$ to 0.6. This effect is illustrated in the pressure distributions of figures 59 to 61. The pressure distributions are plotted for each of the airfoils at a clean C_l of approximately 0.5, with the ice shape 296 simulation at the same angle of attack. For the NACA 23012 airfoil (figure 59), the ice simulation did not significantly alter the clean pressure distribution. There was a higher suction peak in the iced case owing to the local flow acceleration around the roughness. This was followed by a more severe adverse pressure gradient, up to $x/c \approx 0.25$, where the clean and iced pressure distributions were very similar. There was some divergence of the trailing-edge pressure in the iced case that was perhaps indicative of boundary layer separation. For the NACA 3415 airfoil (figure 60), the local flow acceleration and accompanying suction peak were still present, but the suction pressures aft of the ice shape were substantially lower than in the clean case. This effect was also observed for the NLF 0414 airfoil (figure 61), except that the larger differences in the clean and iced suction pressures were further aft on the airfoil.

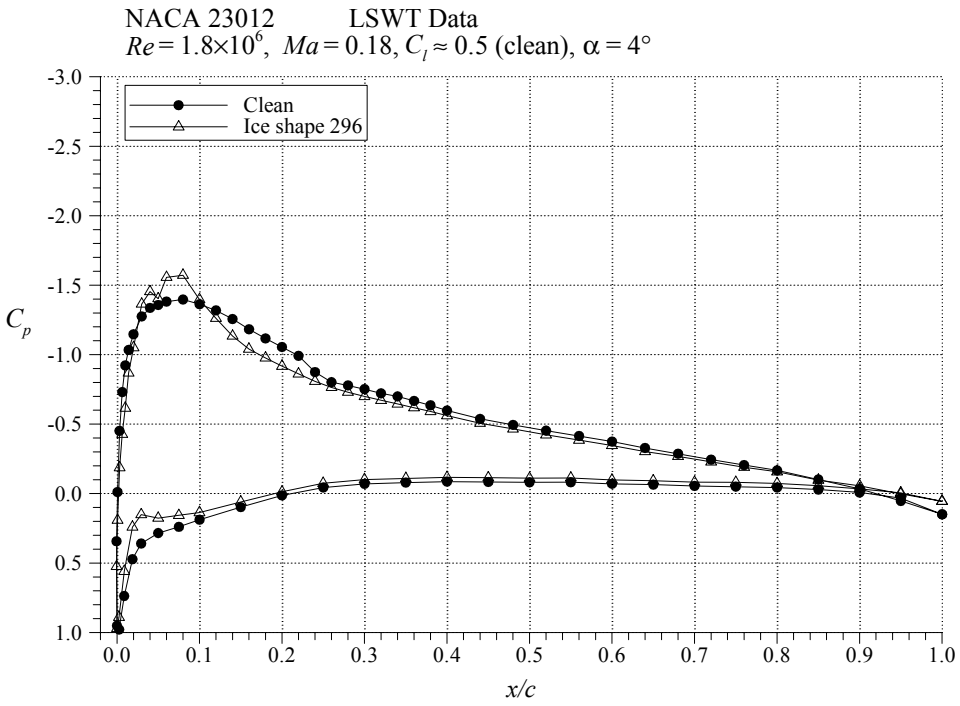

FIGURE 59. EFFECT OF BUILT-UP ROUGHNESS INTERCYCLE ICE SIMULATION ON NACA 23012 AIRFOIL PRESSURE DISTRIBUTION

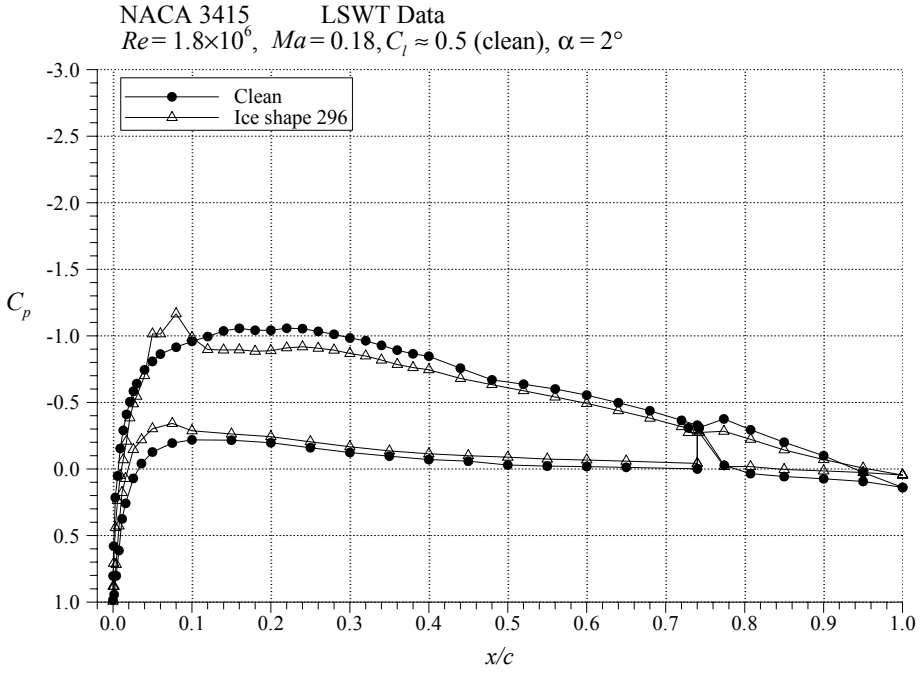

FIGURE 60. EFFECT OF BUILT-UP ROUGHNESS INTERCYCLE ICE SIMULATION ON NACA 3415 AIRFOIL PRESSURE DISTRIBUTION

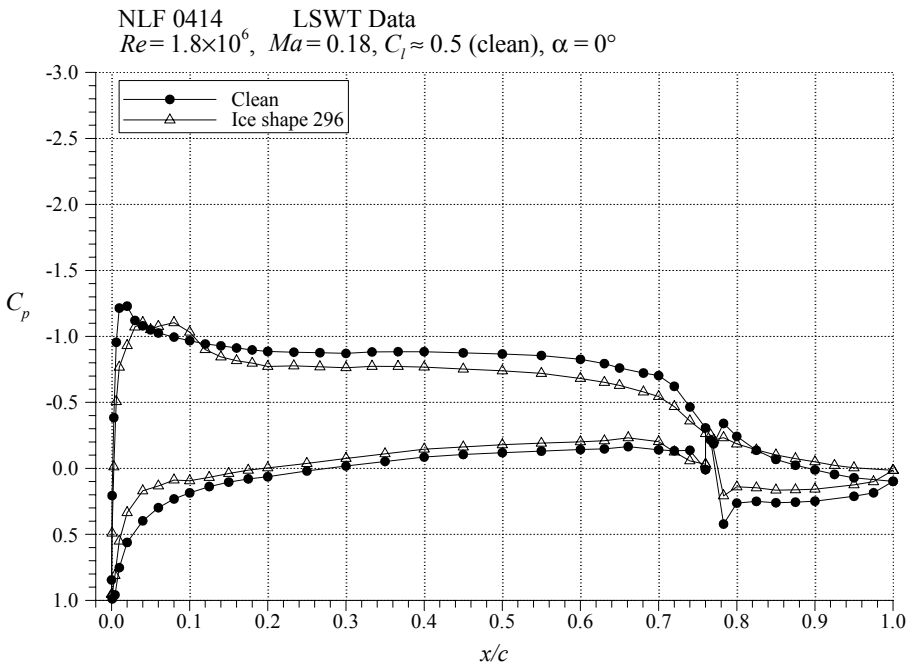

FIGURE 61. EFFECT OF BUILT-UP ROUGHNESS INTERCYCLE ICE SIMULATION ON NLF 0414 AIRFOIL PRESSURE DISTRIBUTION

4.4 GLAZE HORN-TYPE ICE ACCRETIONS.

4.4.1 Airfoil Geometry Effects.

The use of simulated glaze horn-type ice shapes allowed for parametric variation of geometric characteristics such as horn height, radius, and surface position. These effects are presented and discussed here for the NACA 23012 and 3415 airfoils. Kim and Bragg [9] showed that the horn radius had only a small effect on the airfoil performance of the NLF 0414 airfoil. A similar conclusion can be drawn for the NACA 23012 and 3415 airfoils. These data are plotted in figures 62 and 63. The plots show the variation in performance with horn-tip radius for the k/c = 0.0433 horn shape located at s/c = 0.034. For the NACA 23012 (figure 62), the $C_{l,max}$ was reduced to a range of 0.35 to 0.45. The larger radius shapes produced the larger maximum lift values; however, the variation was small relative to the degradation from the clean case. The pitching moment and drag coefficients were also generally affected more by the smallest radius shape. A very similar pattern was observed for the NACA 3415 data (figure 63). What is perhaps more noteworthy is that the $C_{l,max}$ values for this airfoil with the same ice simulations were in the range of 0.60 to 0.70. These values were significantly higher than the NACA 23012 and is consistent with results already presented in this report.

Kim and Bragg [9] also reported on the effects of horn height for different surface locations. They found that the height of shapes located near the leading edge had only a small effect on the lift performance. The present data showed that this also occurred for the NACA 23012 and 3415 airfoils. An example of these effects is shown in figure 64 for the latter airfoil. There was small variation in $C_{l,max}$ with large increases in horn height. Also, this degradation from the clean

airfoil was relatively small. As indicated by Kim and Bragg [9], the ice simulations located at the leading edge can have the effect of lengthening the airfoil chord, which tends to offset the flow disturbance effects of the ice simulation. In contrast to this, the effects on pitching moment and drag coefficient were much more dependent on horn height, with the larger shapes having the greater effect. The hinge moment remained relatively unaffected by the differences in horn height.

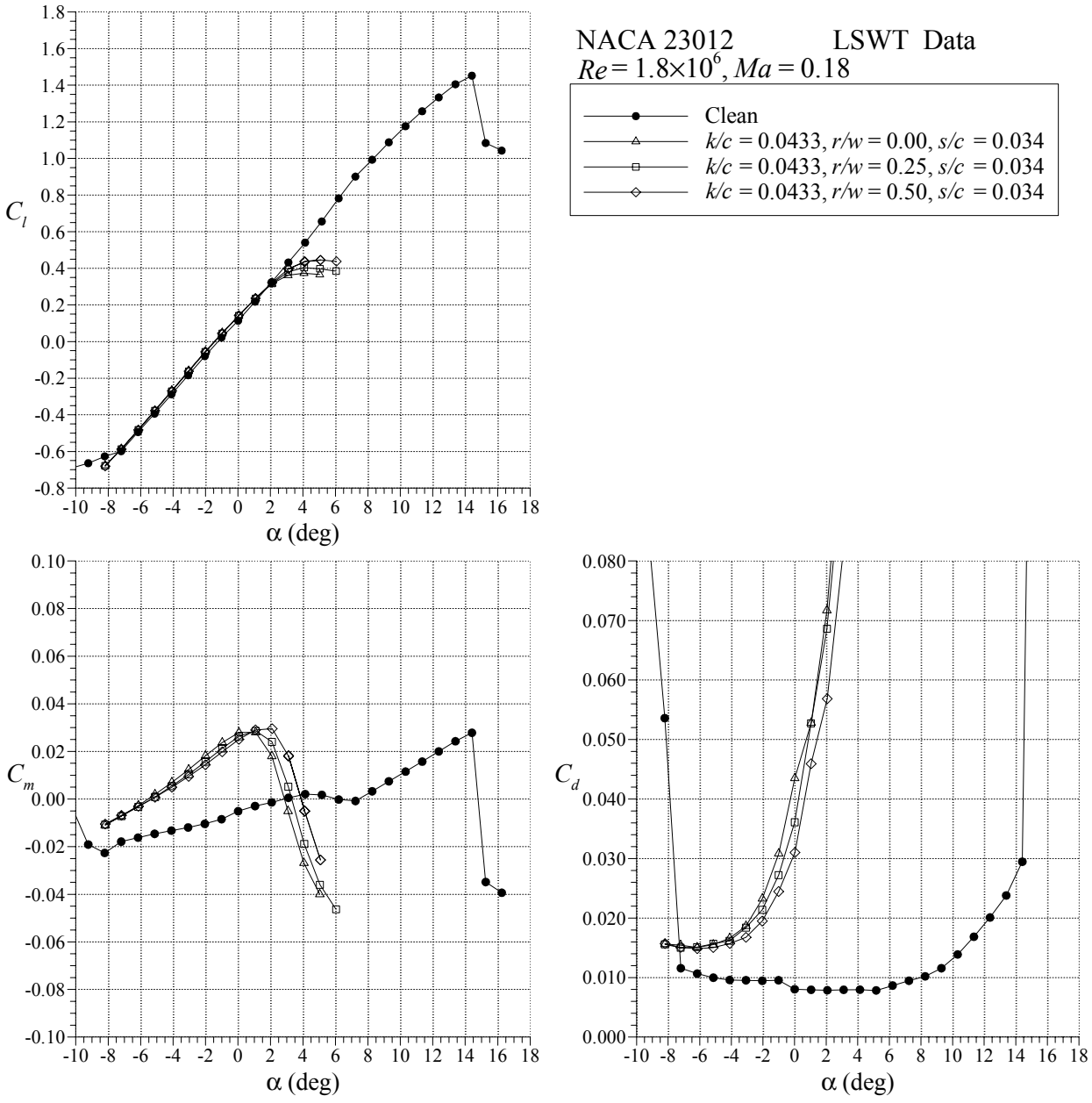

FIGURE 62. EFFECT OF GLAZE HORN TIP RADIUS ON NACA 23012 AIRFOIL PERFORMANCE

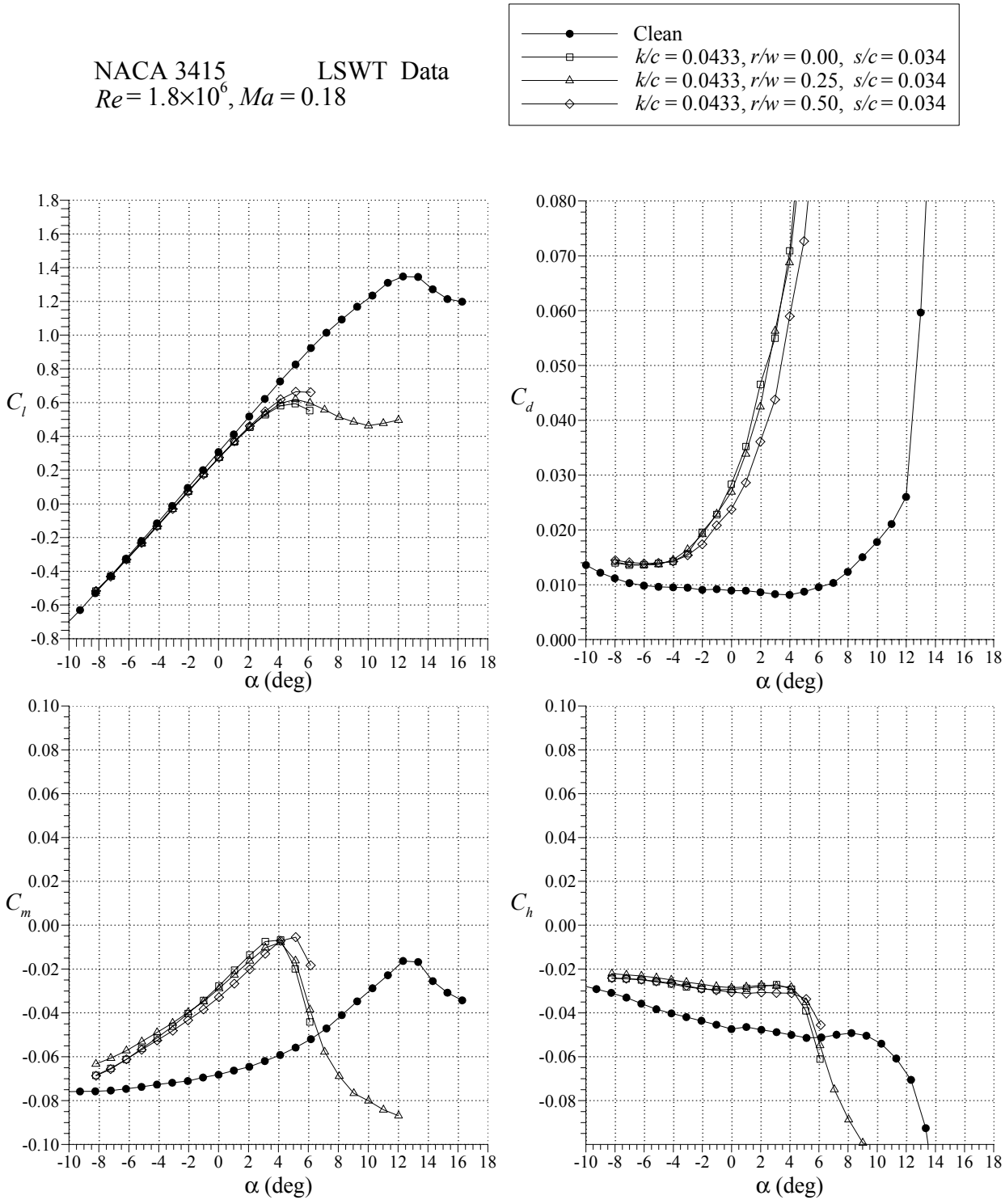

FIGURE 63. EFFECT OF GLAZE HORN TIP RADIUS ON NACA 3415 AIRFOIL PERFORMANCE

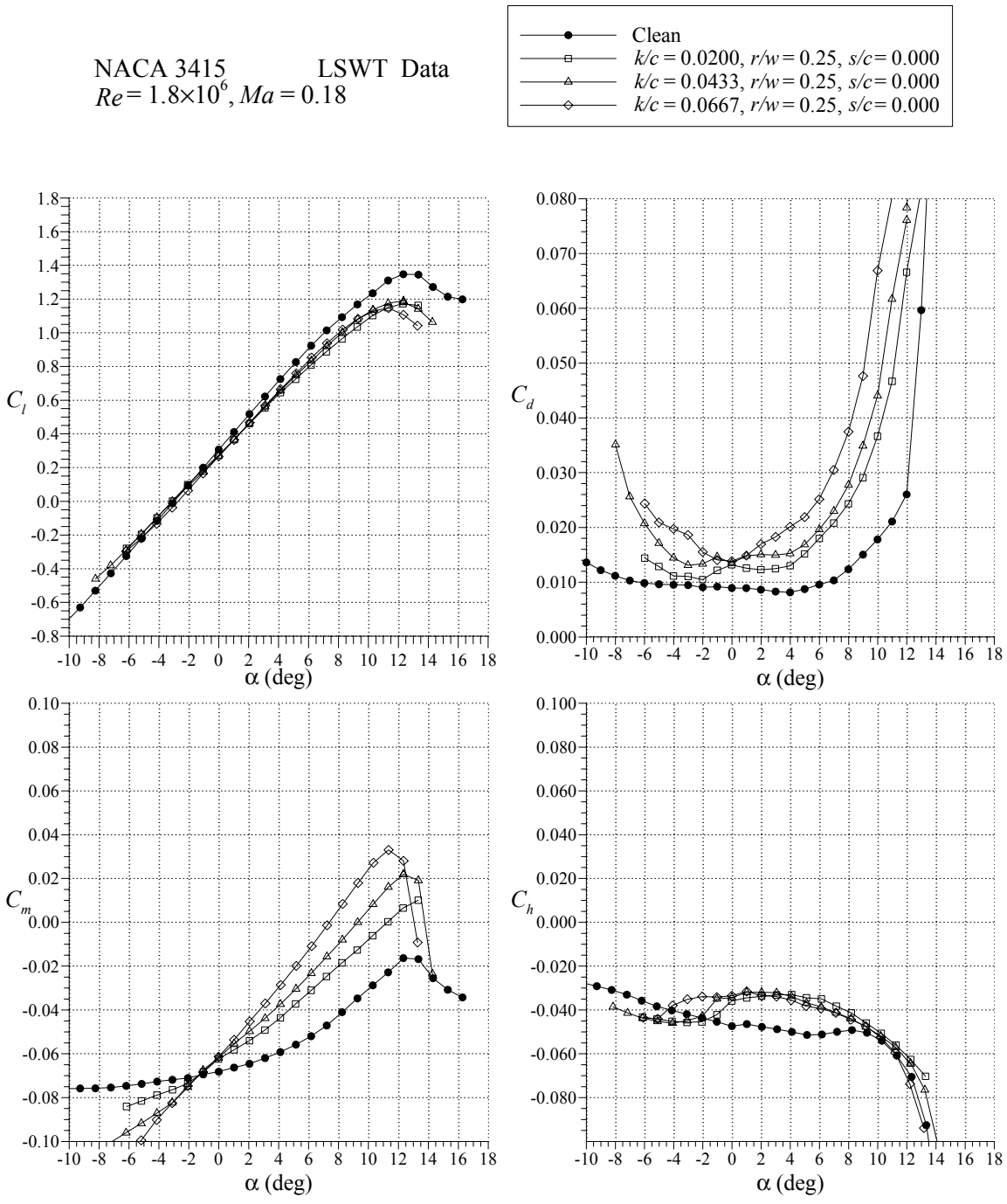

FIGURE 64. EFFECT OF GLAZE HORN HEIGHT ON NACA 3415 AIRFOIL PERFORMANCE

The effect of the horn height had a much larger effect on the lift performance when located on the upper surface downstream of the leading edge. This is illustrated for the NACA 23012 airfoil in figure 65 with the various height shapes located at s/c = 0.034. Here, the $C_{l,max}$ values ranged from about 0.30 to 0.55. So the largest horn shape had nearly half of the maximum lift value caused by the smallest shape. An analogous range was also observed for the NACA 3415

in this investigation and for the NLF 0414 by Kim and Bragg [9]. The effect of horn height on the pitching moment and drag was also more significant at this location than when located at the leading edge.

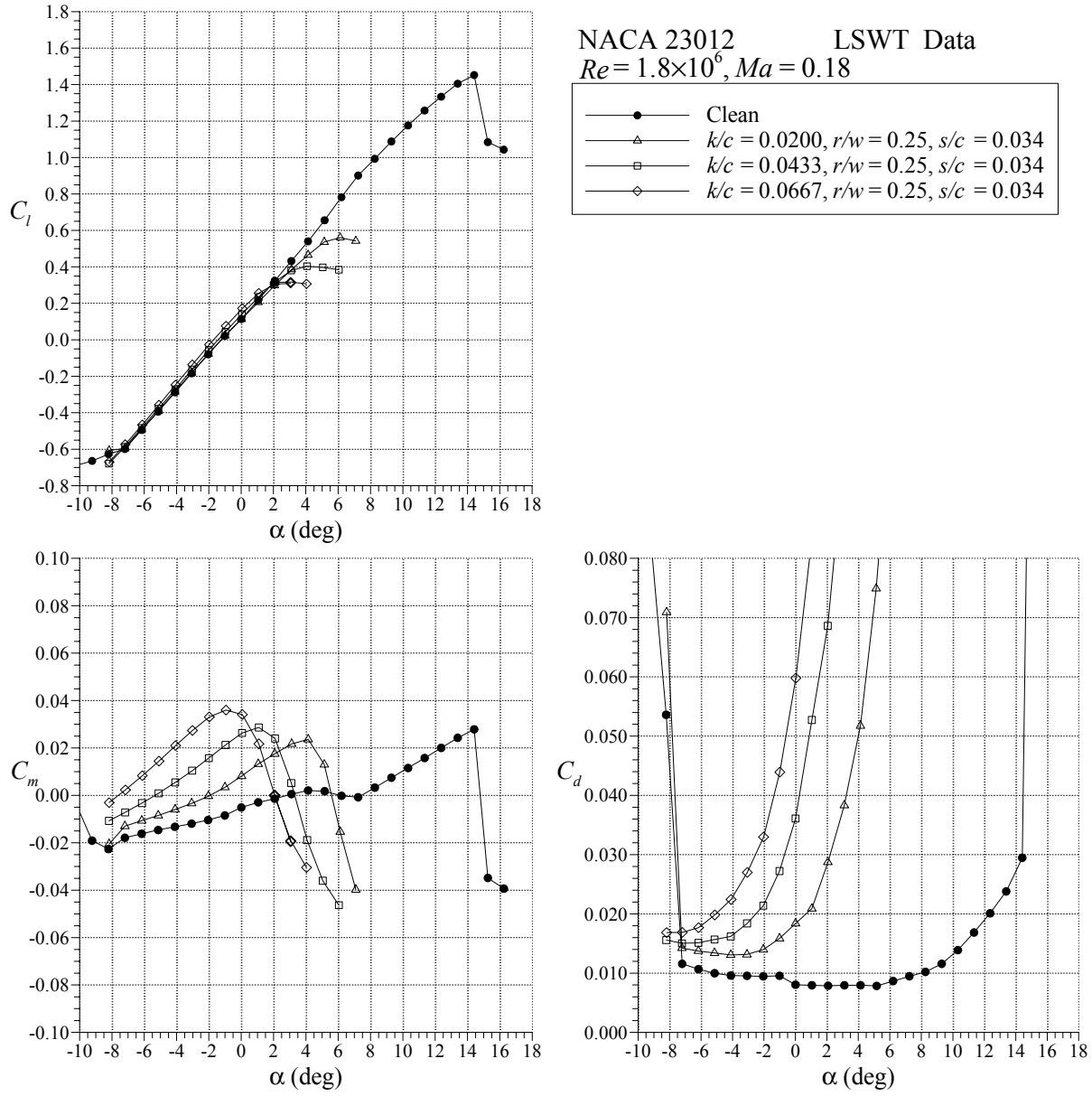

FIGURE 65. EFFECT OF GLAZE HORN HEIGHT ON NACA 23012 AIRFOIL PERFORMANCE

The effect of ice shape location is shown in figures 66 and 67 for the $k/c = 0.0433$ and $r/w = 0.25$ horn shape on the NACA 23012 and 3415 airfoils. The general variation in maximum lift with horn location was similar for the two airfoils. The leading edge to lower surface locations resulted in a much lower lift penalty, and there was less of a dependence upon the location, particularly for the NACA 3415. In this case, the $C_{l,max}$ values were clustered around 1.2 for the two lower surface and leading edge locations. For the NACA 23012 airfoil, the $C_{l,max}$ values

ranged from 1.00 to 1.15. In contrast, the stalling angles for the NACA 3415 airfoil varied two or three degrees with the horn location. For the NACA 23012 airfoil, the maximum lift was attained at the same angle of attack (≈10°) for these locations. As implied in the previous discussion, the effects on maximum lift were much greater for horn locations on the upper surface. The $C_{l,max}$ decreased from 1.00 to 0.40 because the horn location was moved from the leading edge to $s/c = 0.034$ on the NACA 23012 airfoil. The magnitude of this change was nearly identical for the NACA 3415 airfoil, going from about 1.20 for the leading edge location down to 0.60 for $s/c = 0.034$.

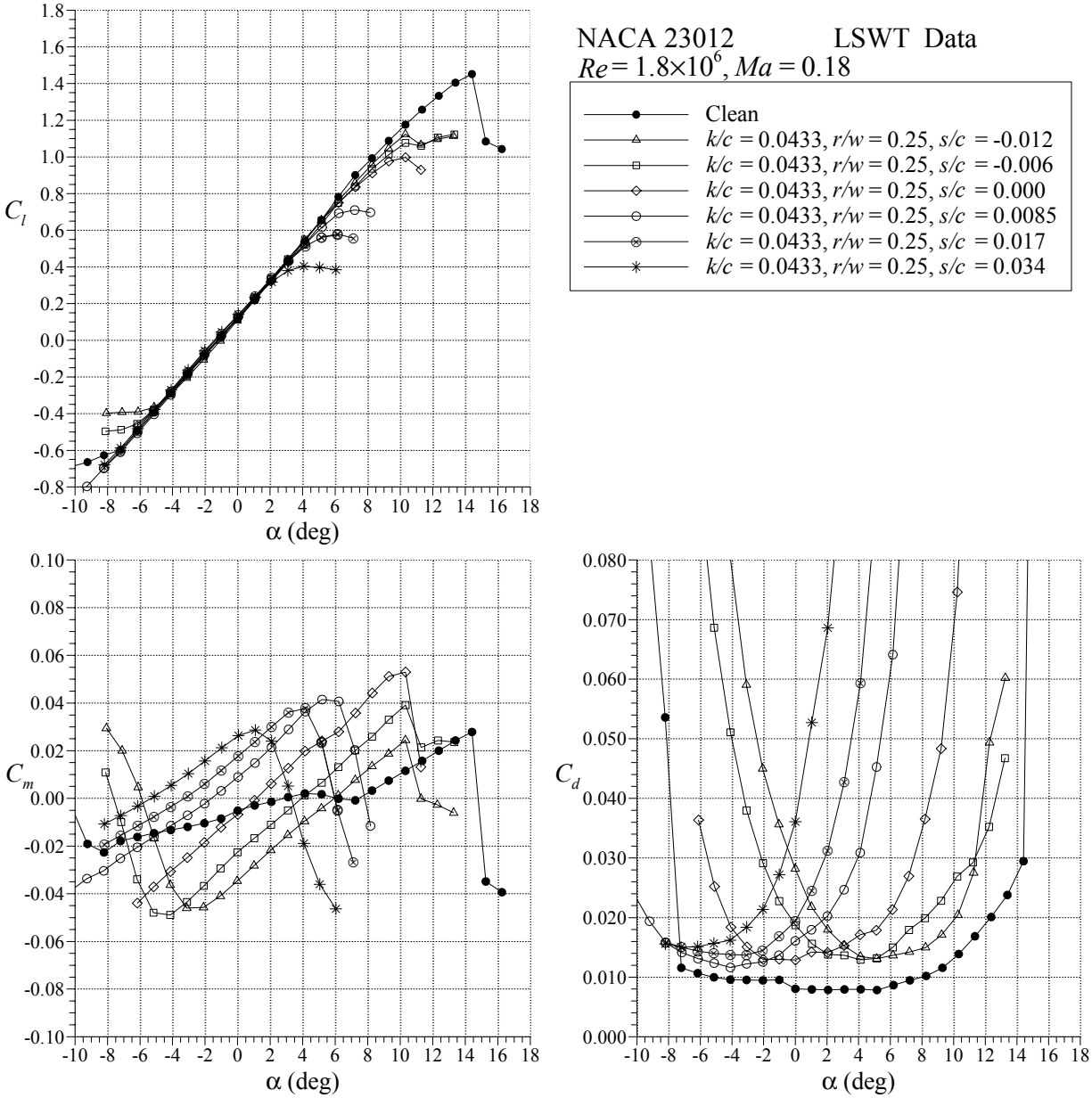

FIGURE 66. EFFECT OF GLAZE HORN LOCATION ON NACA 23012 AIRFOIL PERFORMANCE

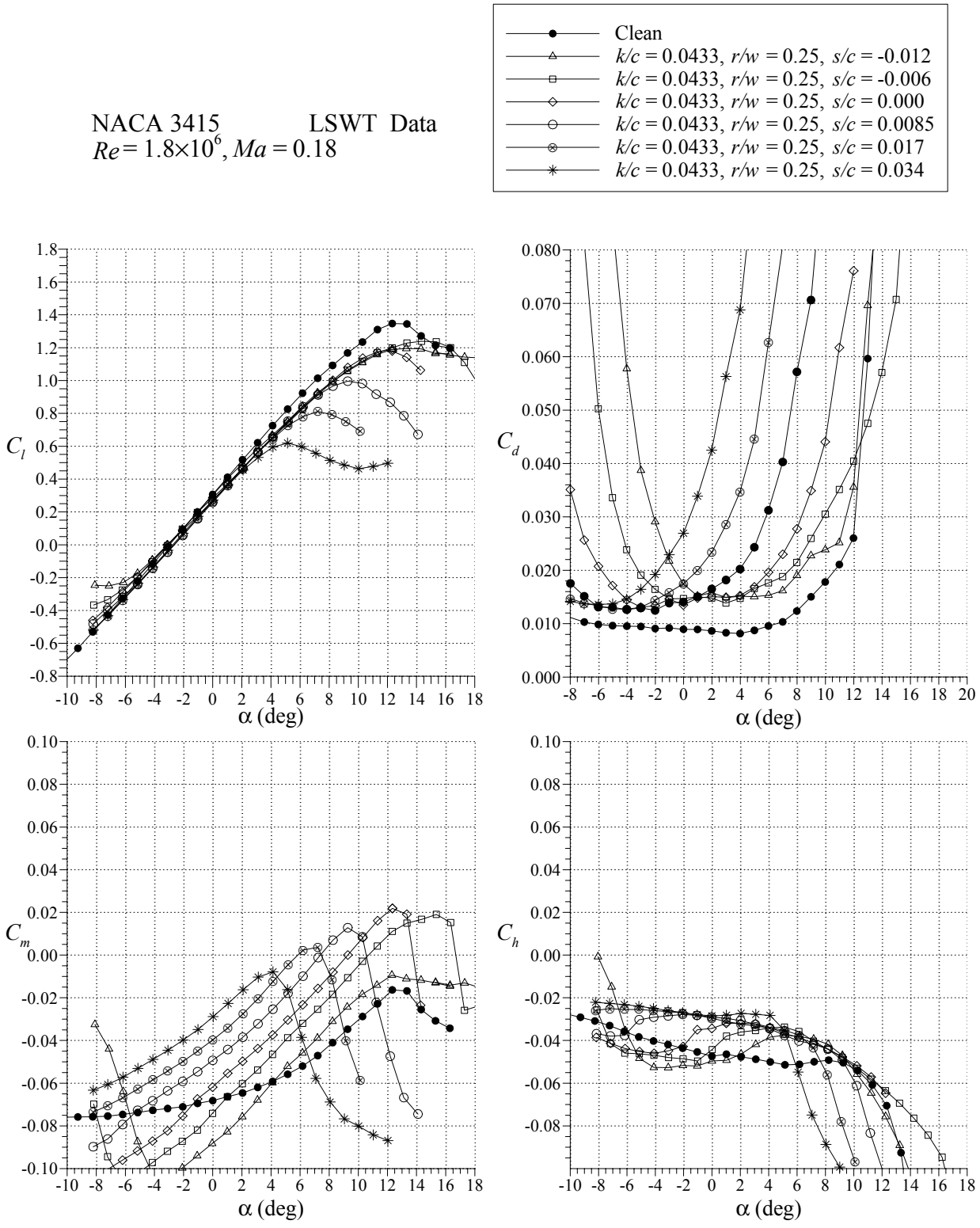

FIGURE 67. EFFECT OF GLAZE HORN LOCATION ON NACA 3415 AIRFOIL PERFORMANCE

The differences in the pitching moment follow the changes in maximum lift behavior. The breaks in C_m occurred at the same angle of attack with the ice shape located on the leading edge and lower surface for the NACA 23012 airfoil, but different angles of attack for the NACA 3415 airfoil. The C_m breaks occurred at lower angles of attack because the horn locations on the upper surface were varied in such a way that the stalling angle decreased. Ice horn locations near the leading edge also resulted in higher nose-up pitching moment values prior to stall than did locations downstream on the upper and lower surfaces. Figure 67 shows that the breaks in the hinge moment data also tended to follow the variation in stalling angle of attack and pitching moment breaks.

The effect of ice shape location on the drag performance did not exhibit such differences between the upper and lower surface locations. Instead, the minimum drag values tended to be about the same for each airfoil regardless of the horn location. This range of minimum C_d was about 0.012 to 0.016 for both airfoils in figures 66 and 67. The plots also show that the minimum C_d tended to occur at lower angles of attack (and lower lift coefficients) because the horn locations change from lower surface to upper surface. This trend seems to support the notion that iced airfoil drag is the lowest at the angle of attack where the ice was accreted, as noted by Kim and Bragg [9].

The effects of horn height and location on maximum lift for all three of the airfoils are summarized in figures 68 through 70 for the NACA 23012, NACA 3415, and NLF 0414 airfoils, respectively. The effects were similar for all of the airfoils for locations from the leading downstream on the upper surface. For the NACA 23012 (figure 68), the $C_{l,max}$ decreased significantly for all horn heights from s/c = 0.000 to 0.0085. The decline then became more linear from s/c = 0.0085 to 0.034. This variation contrasted the NACA 3415 and NLF 0414 airfoils, where the decrease in $C_{l,max}$ tended to be more linear from s/c = 0.000 to 0.034. The changes in maximum lift that occurred for horn locations on the lower surface to the leading edge were much less predictable. In this case, there were a number of competing effects. The simulated ice horns caused less significant flow disturbances on the upper surface, thus resulting in less reductions in maximum lift. The horns may have acted as leading-edge, flap-type devices. This is illustrated for the NLF 0414 case, where the $C_{l,max}$ was actually increased by the simulated ice horn (k/c = 0.0667). The horns also tended to add lift by effectively increasing the chord length of the airfoil. The maximum lift behavior at these locations was a complicated combination of these effects.

Perhaps the most important conclusion to be drawn from figures 68 through 70 is the effect of airfoil geometry. Here again, the airfoil geometry played a role in determining the maximum lift degradation in the iced case. Looking at the data for locations downstream of the leading edge on the upper surface, the lowest $C_{l,max}$ values were for the NACA 23012 airfoil. The effects for the NACA 3415 and NLF 0414 airfoils were similar and less severe. The results here were analogous to the quarter-round data in figure 33 for shapes located at x/c = 0.00 to 0.02.

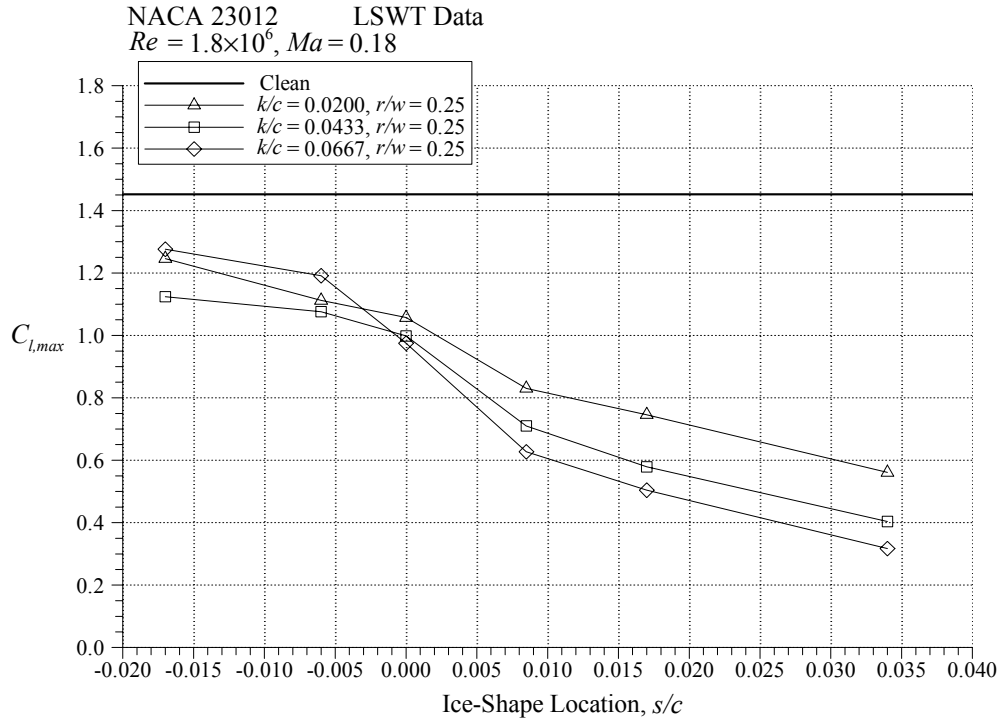

FIGURE 68. EFFECT OF GLAZE HORN ICE SIMULATIONS ON NACA 23012 AIRFOIL $C_{l,max}$

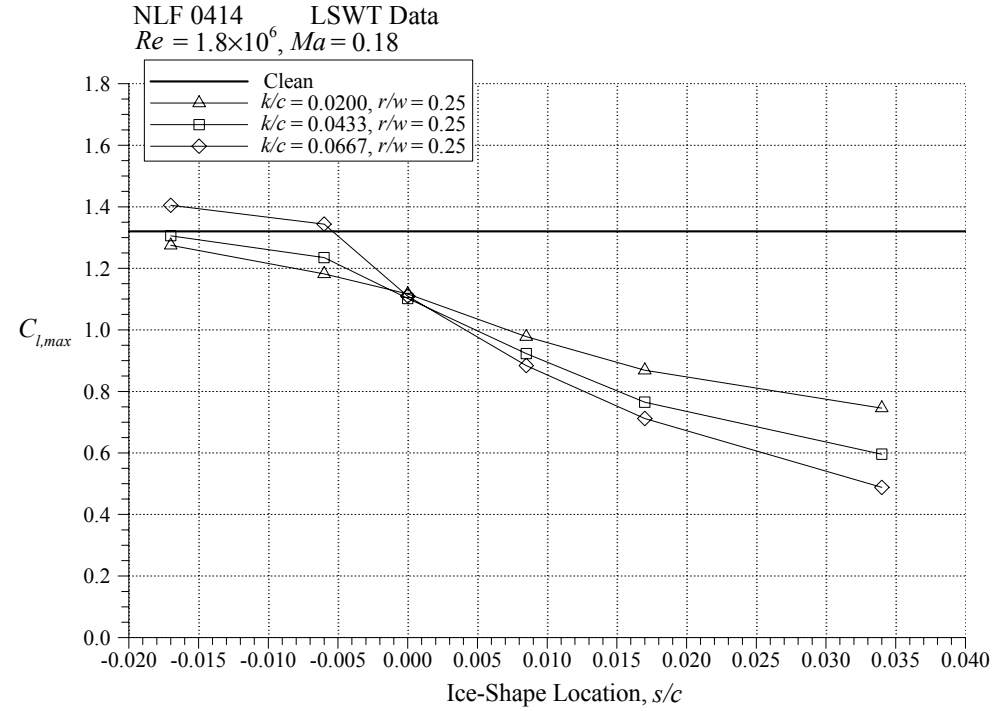

FIGURE 69. EFFECT OF GLAZE HORN ICE SIMULATIONS ON NLF 0414 AIRFOIL $C_{l,max}$

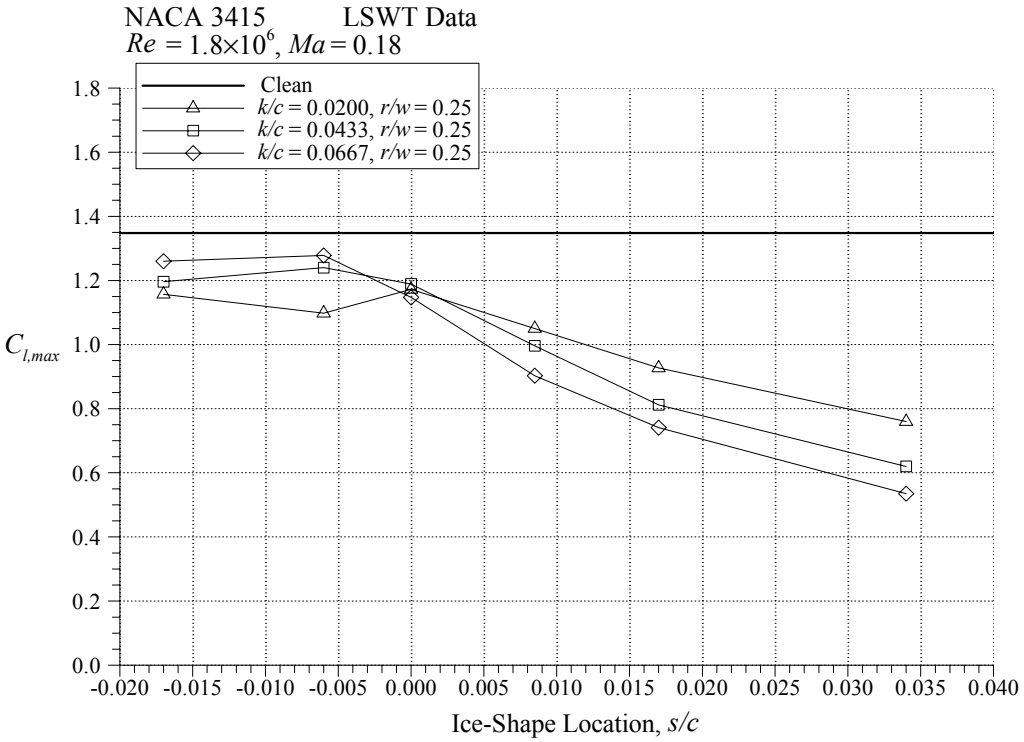

FIGURE 70. EFFECT OF GLAZE HORN ICE SIMULATIONS ON NACA 3415 AIRFOIL $C_{l,max}$

4.4.2 Reynolds and Mach Numbers Effects.

The Reynolds and Mach numbers effects on airfoil performance with the glaze horn-type ice simulations were investigated in the LTPT using the NACA 23012 airfoil. The effect of Reynolds number on the airfoil performance with the k/c = 0.0200 and r/w = 0.25 simulated ice horn at s/c = 0.034 is shown in figure 71. These results are very similar to what was shown for the SLD quarter-round simulations. The only significant Reynolds number differences were in the drag coefficient for negative angles of attack. Identical results were obtained for the larger k/c = 0.0433 horn shape as well. The effect of Mach number is shown in figure 72. For this case, Mach number had only a small effect on $C_{l,max}$. The maximum lift value for Ma = 0.28 would be taken as occurring at about $\alpha = 6°$; however, this value was very close to the lower Mach number. Also, the lift continued to increase in the poststall region. Similar lift behavior was observed with the quarter-round ice shape located at x/c = 0.02 (cf. figure 39). This effect was also observed in the pitching moment data, where the C_m continued to decrease. The drag data exhibited more typical Mach number effects. The anomaly in the lift curve was also observed for the k/c = 0.0433 horn shape, as shown in figure 73. Here, it is difficult to determine that the airfoil has stalled at about $\alpha = 4°$, just by looking at the lift data. The difference in the lift levels in the poststall region are illustrated in figure 74 for $\alpha = 6°$. The increased suction levels aft of the simulated ice shape obviously account for the difference in lift, but the reason for this behavior is not clear.

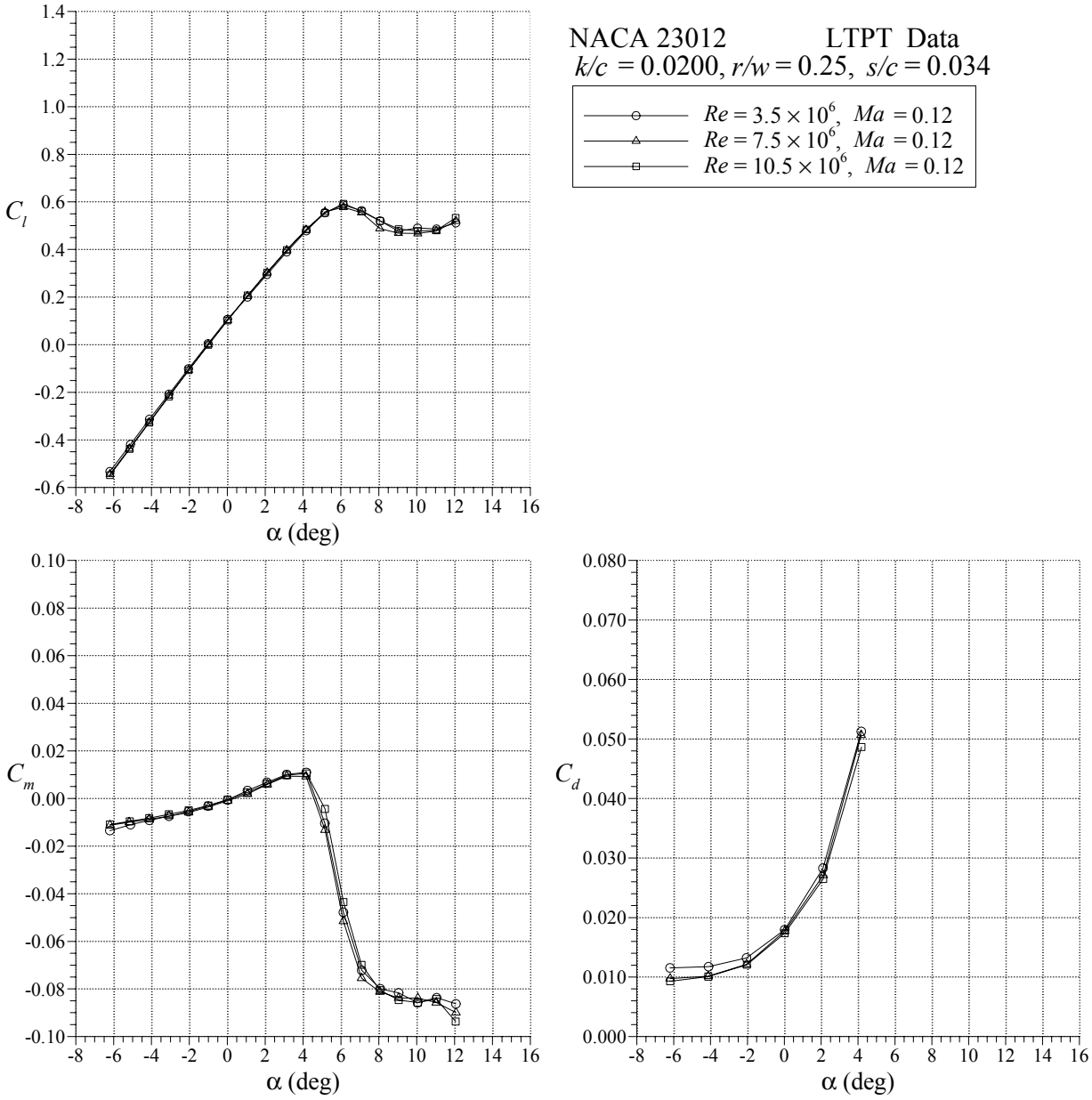

FIGURE 71. EFFECT OF REYNOLDS NUMBER ON NACA 23012 AIRFOIL PERFORMANCE WITH GLAZE HORN ICE SIMULATION

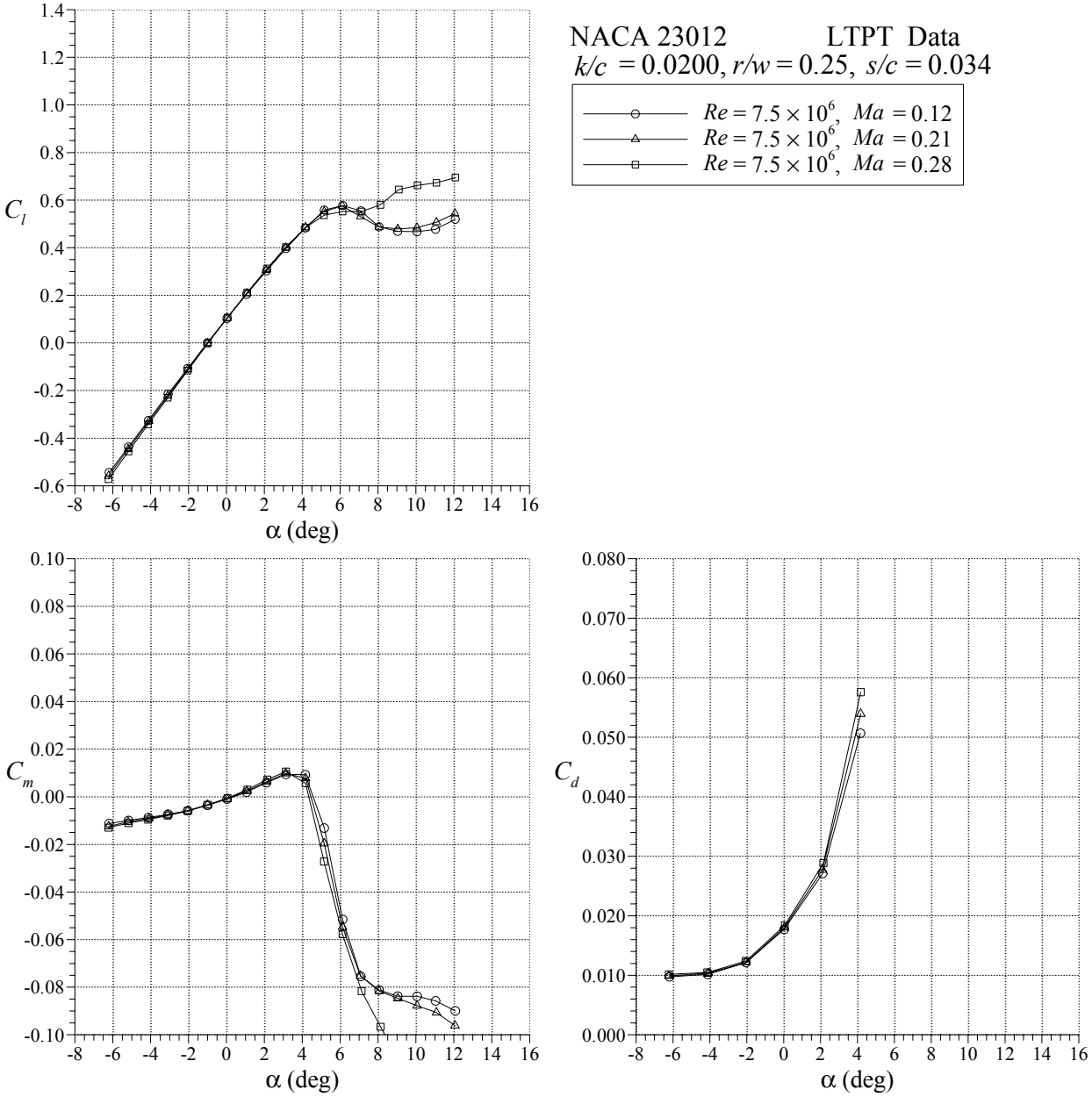

FIGURE 72. EFFECT OF MACH NUMBER ON NACA 23012 AIRFOIL PERFORMANCE WITH GLAZE HORN ICE SIMULATION

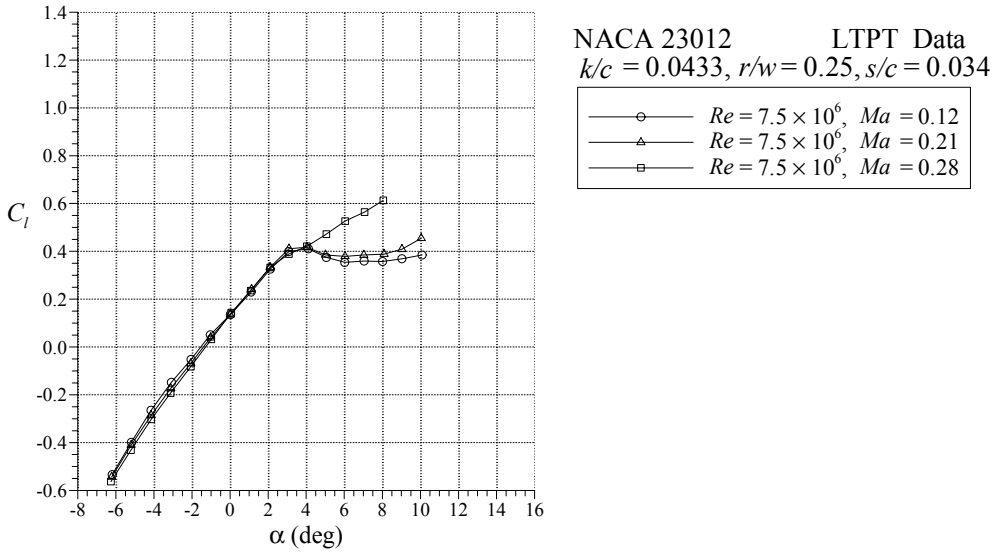

FIGURE 73. EFFECT OF MACH NUMBER ON NACA 23012 AIRFOIL LIFT PERFORMANCE WITH GLAZE HORN ICE SIMULATION

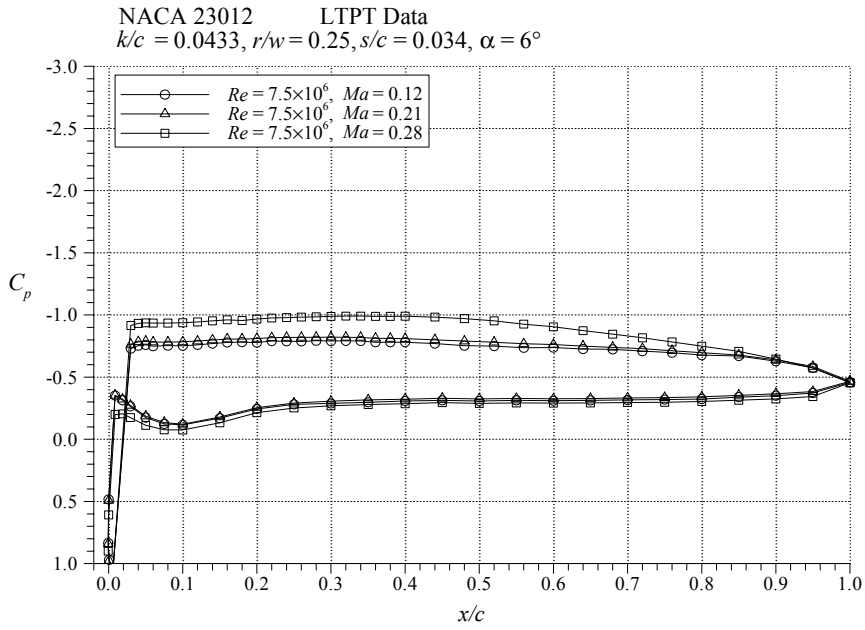

FIGURE 74. EFFECT OF MACH NUMBER ON NACA 23012 AIRFOIL PRESSURE DISTRIBUTION WITH GLAZE HORN ICE SIMULATION

The Mach number behavior for the leading-edge, horn-type simulations also differed from the SLD ice shape simulations at the lower Reynolds number. This is shown in figure 75 for Re 2.0×10^6, where the lift curves were nearly identical. Data from the LTPT were also directly compared to data from the LSWT in figure 76 for this ice shape for closely matched Mach numbers. Here again, there was virtually no Reynolds number dependence in terms of maximum lift. Similar results were also obtained for the $k/c = 0.0433$ horn shape at this s/c location.

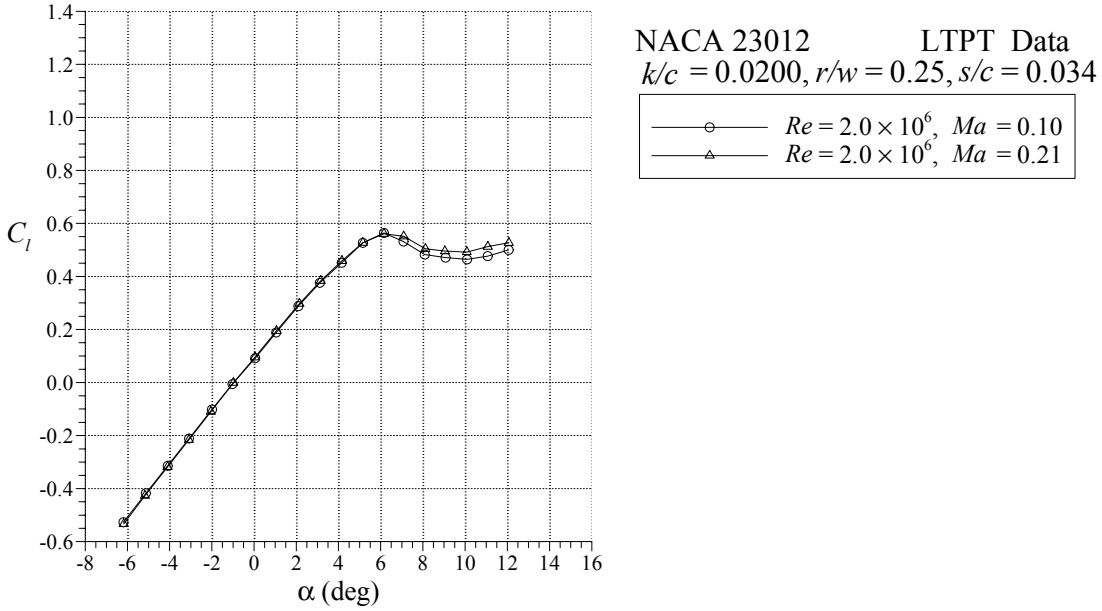

FIGURE 75. EFFECT OF MACH NUMBER (WITH $Re = 2.0 \times 10^6$) ON NACA 23012 AIRFOIL PERFORMANCE WITH GLAZE HORN ICE SIMULATION

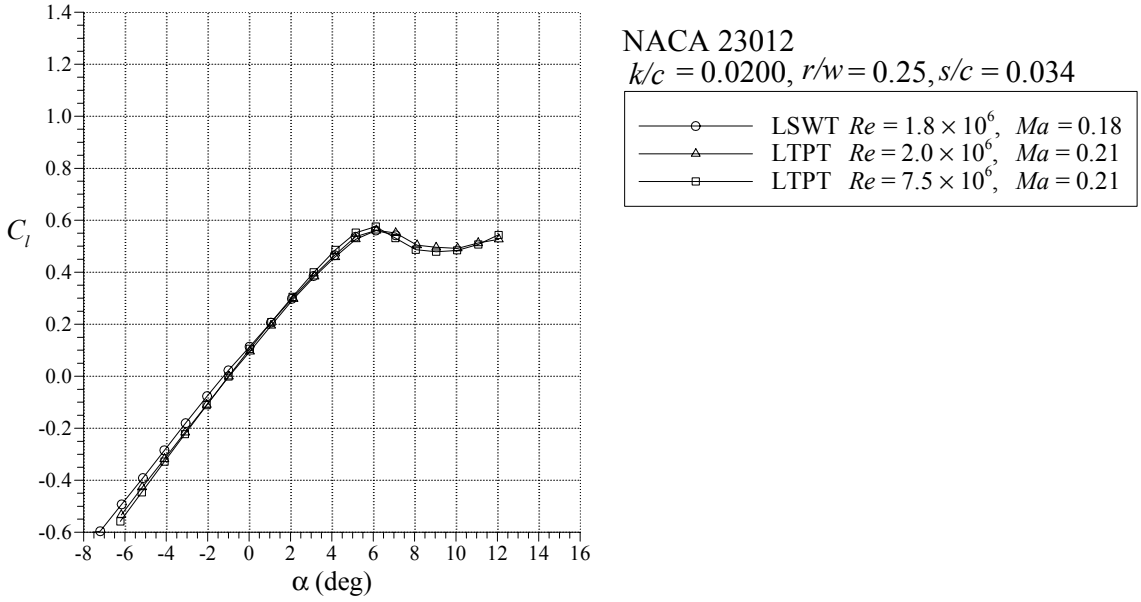

FIGURE 76. COMPARISON OF LTPT AND LSWT DATA FOR THE NACA 23012 AIRFOIL WITH GLAZE HORN ICE SIMULATION AT $s/c = 0.034$

Reynolds number effects on lift were more pronounced for the horn shapes located at the leading edge location. Also, the Mach number anomaly in the lift, shown in figures 72 and 73, was not present. The data in figure 77 show typical increases in lift curve slope with increased Mach number, but the maximum lift values were nearly identical. However, an increase in Reynolds

number from 1.8×10^6 LSWT data to 7.5×10^6 LTPT data showed an attendant increase in maximum lift and lift curve slope for the same horn shape (see figure 78). This Reynolds number dependence was less, but still significant for the smaller, $k/c = 0.0200$ horn shape.

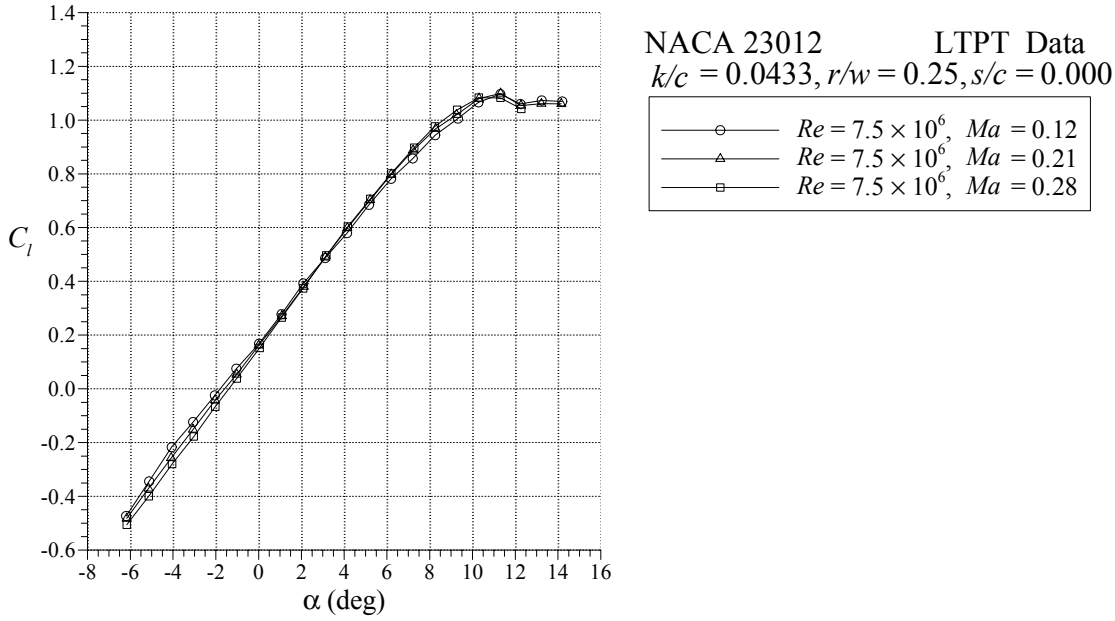

FIGURE 77. EFFECT OF MACH NUMBER ON NACA 23012 AIRFOIL PERFORMANCE WITH GLAZE HORN ICE SIMULATION AT $s/c = 0.000$

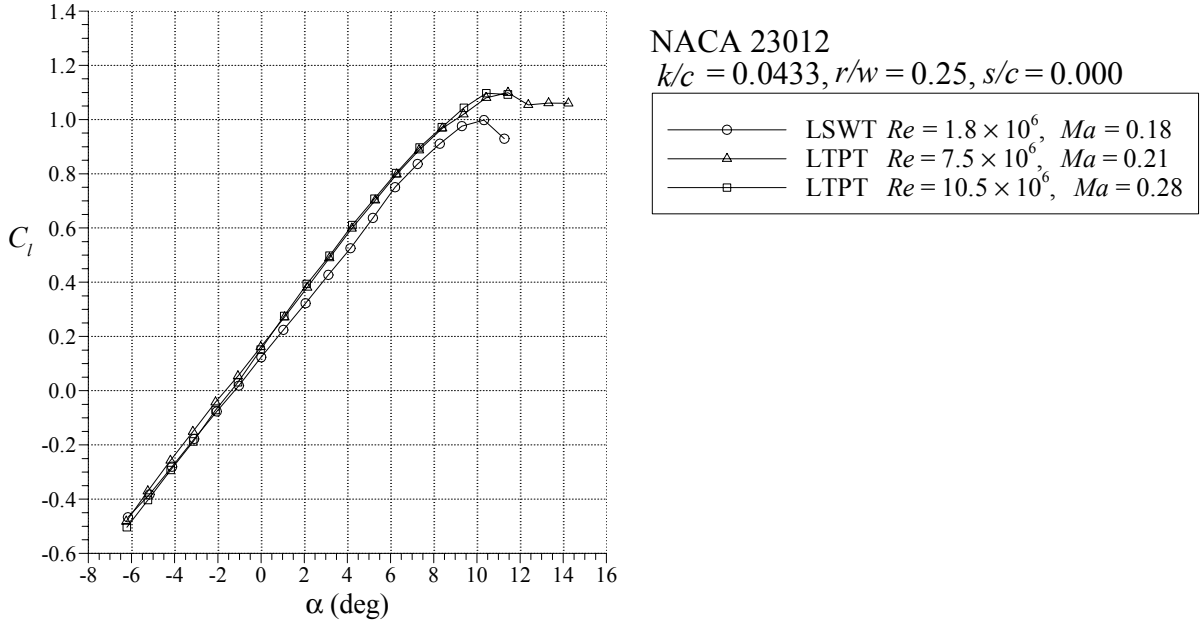

FIGURE 78. COMPARISON OF LTPT AND LSWT DATA FOR THE NACA 23012 AIRFOIL WITH GLAZE HORN ICE SIMULATION AT $s/c = 0.000$

5. CRITICAL ICE SHAPE METHODOLOGY.

The FAA 12A Working Group adopted the following definition of critical ice [2]:

> "Critical ice shapes are those with ice accretion geometries and features representative of that which can be produced within the icing certification envelope that result in the largest adverse effects on performance and handling qualities over the applicable phases of flight of aircraft."

A past method for determining the critical ice shape for a particular aircraft consisted of determining the most severe icing conditions that are inside the certification envelope. This would usually consist of large droplet, high-liquid content icing clouds at near-freezing temperatures that would produce glaze horn accretion. These icing conditions would typically be the same for all types of aircraft. The resultant ice accretions from these conditions would be tested as critical ice shapes. This resulted in large, leading-edge glaze accretions being classified as critical ice shapes for most types of aircraft. Recent studies have shown that while these shapes can result in substantial reductions in aerodynamic performance, smaller protuberances located further downstream from the leading edge can have larger performance degradations. These shapes could form in icing conditions quite different from those in which the large, leading-edge glaze shapes form. Thus, the FAA 12A Working Group decided to formulate a new methodology for determining the critical ice shape for use in the certification process.

5.1 AERODYNAMIC APPROACH FOR CRITICAL ICE SHAPE.

The past method placed the primary emphasis on the icing condition for determining the critical ice shape. The method proposed by the 12A Working Group places a greater emphasis on the aerodynamic effects of ice accretion, rather than the icing condition that would produce a particular shape. It involves a multistep process and is outlined below:

1. Determine the aerodynamic performance parameter to be considered. This could consist of C_l, C_d, C_m, C_h, etc.

2. Establish the threshold value required for safe operation during different phases of flight, such as takeoff, landing, approach, cruise, hold.

3. Determine the ice shape features (size, horn angle, location, etc.), if any, that cause the aerodynamic performance parameter to fall below the threshold value.

4. Determine the icing conditions (if any) that result in ice shapes with these features.

5.2 APPLICATION OF NEW METHODOLOGY USING CURRENT DATA.

The data obtained in the current test were used to evaluate the steps of the new critical ice shape methodology. The NACA 2310 was chosen for this evaluation primarily because it had aerodynamic characteristics that were dissimilar from the three airfoils tested experimentally for this study. Figure 79 shows the geometry comparison of the NACA 2310 and the three airfoils tested at LSWT.

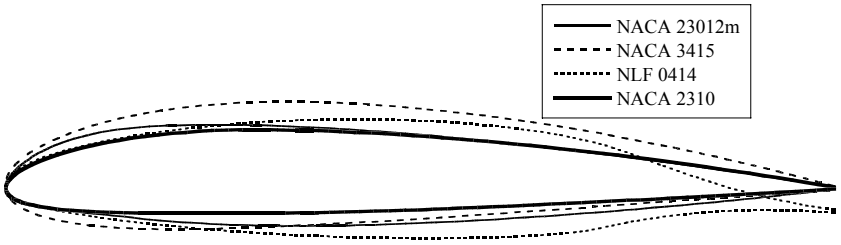

FIGURE 79. NACA 2310 GEOMETRY COMPARED TO THE THREE AIRFOILS TESTED IN THIS STUDY

The first step in evaluating the critical ice shape (as discussed in section 5.1) is to pick the aerodynamic performance parameter to consider. For this evaluation, $C_{l,max}$ was chosen because it is generally the most important parameter when safe aircraft operation is considered.

The second step is to establish a threshold value for $C_{l,max}$ in a given phase of flight. For this, the minimum $C_{l,max}$ during approach was assumed to be 0.50 (although, in practice, this number would be very aircraft specific). Use of the approach phase of the flight allowed the evaluations to be made using data at zero flap deflection.

The third step is to determine the ice shape features that would allow the $C_{l,max}$ value to fall below 0.50. This step required estimating the performance degradation on the NACA 2310 due to icing, using the data from the three airfoils tested for this study. To accomplish this, the clean airfoil aerodynamic characteristics of the NACA 2310 must be known. XFOIL was used to generate the clean airfoil pressure distribution on the NACA 2310, and the comparison to the three airfoils tested at LSWT is shown in figure 80. The comparisons were made at matched lift coefficient of 0.50 for all four airfoils.

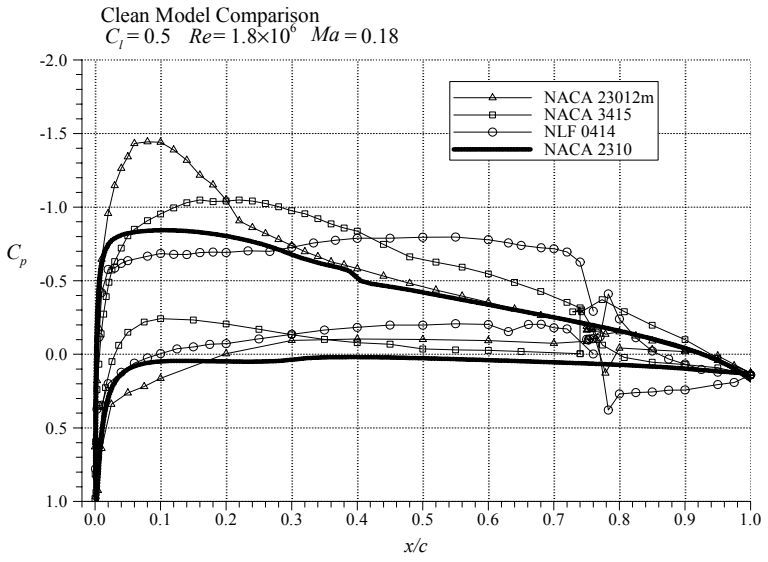

FIGURE 80. NACA 2310 CLEAN AIRFOIL PRESSURE DISTRIBUTION COMPARED TO THE THREE AIRFOILS TESTED IN THIS STUDY

The $C_{p,min}$ of the NACA 2310 was located at x/c = 0.10, which was nearly identical to that of the NACA 23012m. However, the value of the $C_{p,min}$ was much higher at -0.83, compared to -1.44 for the NACA 23012m. Because of this, the NACA 2310 had much less pressure to recover, and a large leading-edge suction region was not present, resulting in a more aft-loaded airfoil than the NACA 23012m. However, it was still more front-loaded than the NACA 3415 and the NLF 0414. The NACA 2310 had a nearly constant pressure gradient in recovery and did not have a region of very severe adverse pressure gradient. Because of this, one would not expect the NACA 2310 to have a chordwise region where it is very sensitive to icing. Also, because the NACA 2310's load distribution fell in between the NACA 23012m and the NACA 3415, its sensitivity to icing that forms near the leading edge would be expected to fall between the NACA 23012m and the NACA 3415. The predicted $C_{l,max}$ versus ice shape location plot for the NACA 2310 (for the k/c = 0.0139 quarter round) is shown in figure 81. Generally, it would look similar to the NACA 3415 data. However, near the leading edge, the $C_{l,max}$ values should be below those of the NACA 3415 but above those of the NACA 23012m.

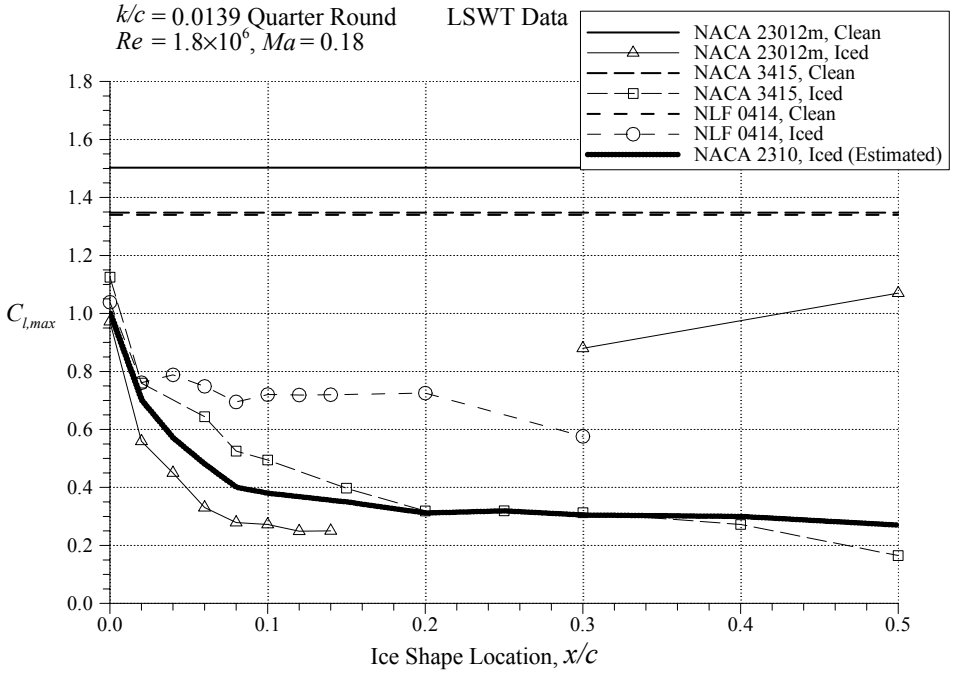

FIGURE 81. ESTIMATED EFFECT OF QUARTER-ROUND ICE SHAPE LOCATION ON $C_{l,max}$ FOR THE NACA 2310 AIRFOIL

The predicted $C_{l,max}$ versus ice shape location plot for the leading-edge glaze shape is shown in figure 82. The $C_{l,max}$ values for the NACA 2310 will likely fall between those of the NLF 0414 and the NACA 23012. This is because the leading-edge pressure distribution is similar to that of the NLF 0414 in that there is almost a step increase in the velocity at the leading edge. However, unlike on the NLF 0414 (which is followed by a long run of slightly favorable pressure gradient), there is a long run of slightly adverse pressure gradient. Because of this, leading-edge ice shapes should have more severe effect than on the NLF 0414. However, the effects will not be as severe as on the NACA 23012 because there is not a severe adverse pressure gradient present near the leading edge.

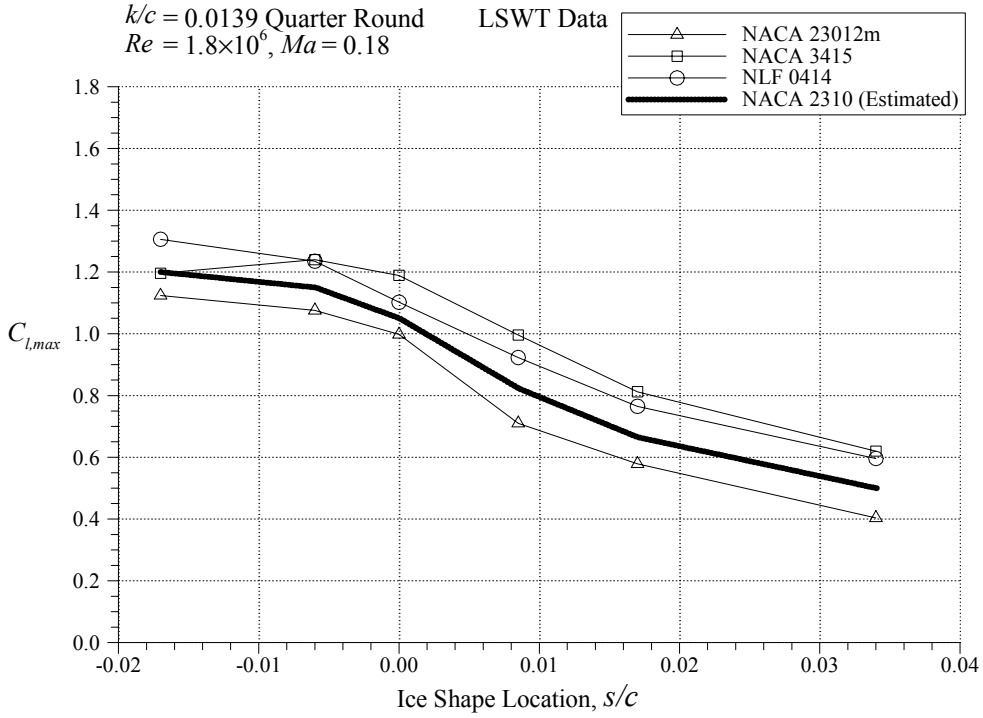

FIGURE 82. ESTIMATED EFFECT OF GLAZE HORN ICE SIMULATIONS ON NACA 2310 AIRFOIL $C_{l,max}$

It is important to note that the description of the iced airfoil characteristics of the NACA 2310 described above is only an educated prediction based on the results from the three airfoils tested at LSWT. As more iced airfoil data becomes available, one would obviously become more confident in the accuracy of these types of predictions. Also, because tests at LSWT and LTPT were 2-D, using the data to directly predict the full aircraft aerodynamic characteristics is not valid. The data should only be used to estimate the most sensitive ice shape location, size, geometry, etc., and not the absolute value of the performance degradation due to icing. This will be explained in more detail in section 5.3. Because of this, step three cannot be completed. However, one can reasonably state that the performance degradation on the NACA 2310 due to ice accretion will become more severe with increasing ice shape height and as the ice shape is located further downstream from the leading edge. It is also likely that smaller ice shapes located well downstream of the leading edge (such as x/c = 0.20) will have a more severe performance degradation than a large shape located near the leading edge.

Because step three could not be completed and a meteorological analysis was beyond the scope of this study, step four could also not be completed.

5.3 IMPLICATIONS OF USING CURRENT DATA FOR NEW CRITICAL ICE SHAPE METHODOLOGY.

First, it is very important to point out that the results from this study should only be used in the limited manner for which it was intended. The results are directly applicable only for straight wing, commuter-class aircraft. Highly swept wings have large amounts of spanwise flow, and

the stalling mechanism may be entirely different than a straight wing. This study was also meant to be a sensitivity analysis of various ice shape parameters on 2-D airfoils and not a test to acquire actual performance losses on real-world aircraft due to real-world ice shapes. Most of the ice simulations used in this study were 2-D, with no spanwise variations. Actual ice accretions have significant spanwise variations, including spanwise gaps due to partial shedding. Spanwise irregularities tend to act like vortex generators, helping to reduce the size of ice-induced separation bubbles. Propeller wash over the wing could potentially have a similar effect, in terms of reducing separation bubble sizes. Because of this, performance losses on aircraft due to real-world ice accretion would generally be less than that caused by 2-D simulated ice shapes that represent them.

Because the models used in this study had a simple flap, one should be careful in applying the results to aircraft with more advanced flap systems. The only effect of the simple flap was to change the camber. On more advanced flaps, the chord is also increased, and boundary layer over the flap is energized through the gap flow. However, the results showed that simply increasing the camber did not significantly alter the sensitivity of an airfoil to icing, as shown in figure 83. This figure shows the summary of airfoil $C_{l,max}$ (of the three airfoils tested) with the k/c = 0.0139 quarter round located at various locations and the flap deflected 10 degrees down. The results were very similar to the zero flap data shown in figure 33. When the ice shape was located upstream of 20% chord, the NLF 0414 had the highest $C_{l,max}$, followed by the NACA 3415 and the NACA 23012m. The only major difference was that all the maximum lift coefficient values were higher (by approximately 0.25) due to increased camber.

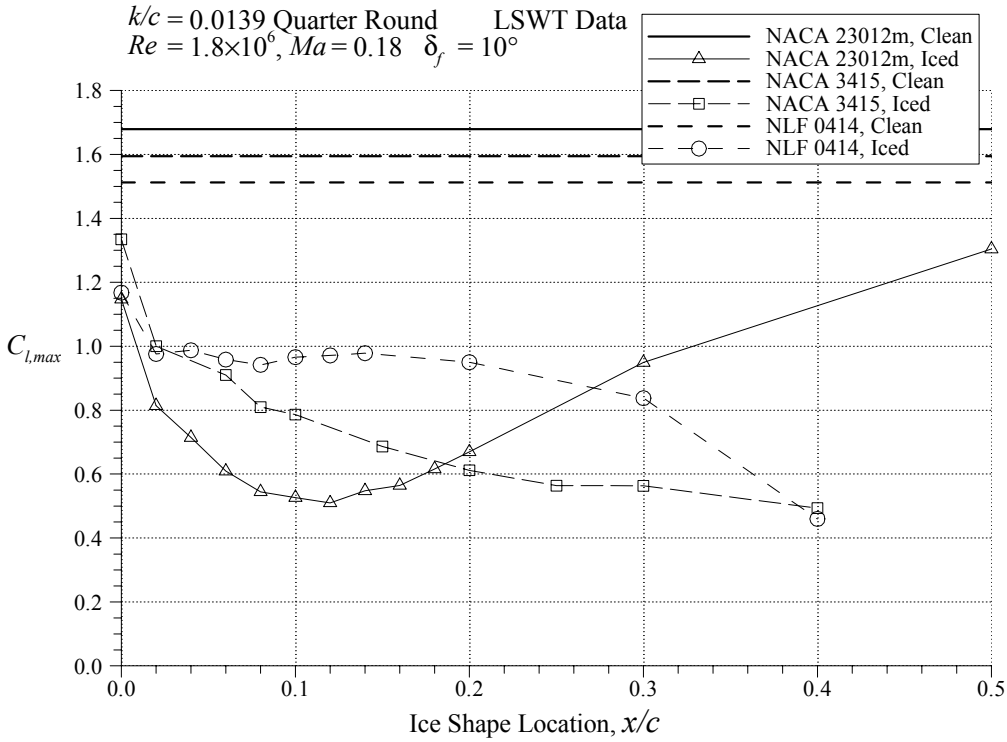

FIGURE 83. EFFECT OF QUARTER-ROUND ICE SHAPE LOCATION ON $C_{l,max}$ WITH 10° FLAP DEFLECTION FOR THE THREE AIRFOILS TESTED AT LSWT

The test also revealed that scaling down the full-size wing and ice accretion geometrically to test in smaller wind tunnels yielded very acceptable results due to the relative insensitivity of iced airfoil aerodynamics to Reynolds and Mach numbers effects. It is much more important to properly scale the ice shape geometrically than it is to attempt to match the Reynolds and Mach numbers at flight conditions. There can still be significant Reynolds and Mach number effects on clean airfoils. If the changes in the aerodynamic coefficients due to icing (when compared to the clean airfoil) need to be known, this effect could be significant. However, the clean airfoil data at high Reynolds and Mach numbers may be obtained through current CFD codes, historical data, or lower-cost (relative to iced configuration) aerodynamic testing.

An airfoil's load distribution played a major role in its sensitivity to ice accretion, particularly in the first 20% chord where ice is likely to accrete. Generally, ice accretions on front-loaded airfoils resulted in larger performance degradations. Because of this, critical ice shapes for these airfoils may be much smaller than those for more aft-loaded airfoils. Figure 84 shows the $C_{l,max}$ versus clean airfoil pitching moment (at C_l = 0.5 for the clean airfoil). Some of the common features of a front-load airfoil are:

- Very low pitching moment about the 1/4 chord
- Location of maximum thickness near the leading edge
- Large, leading-edge suction peak
- No drag bucket

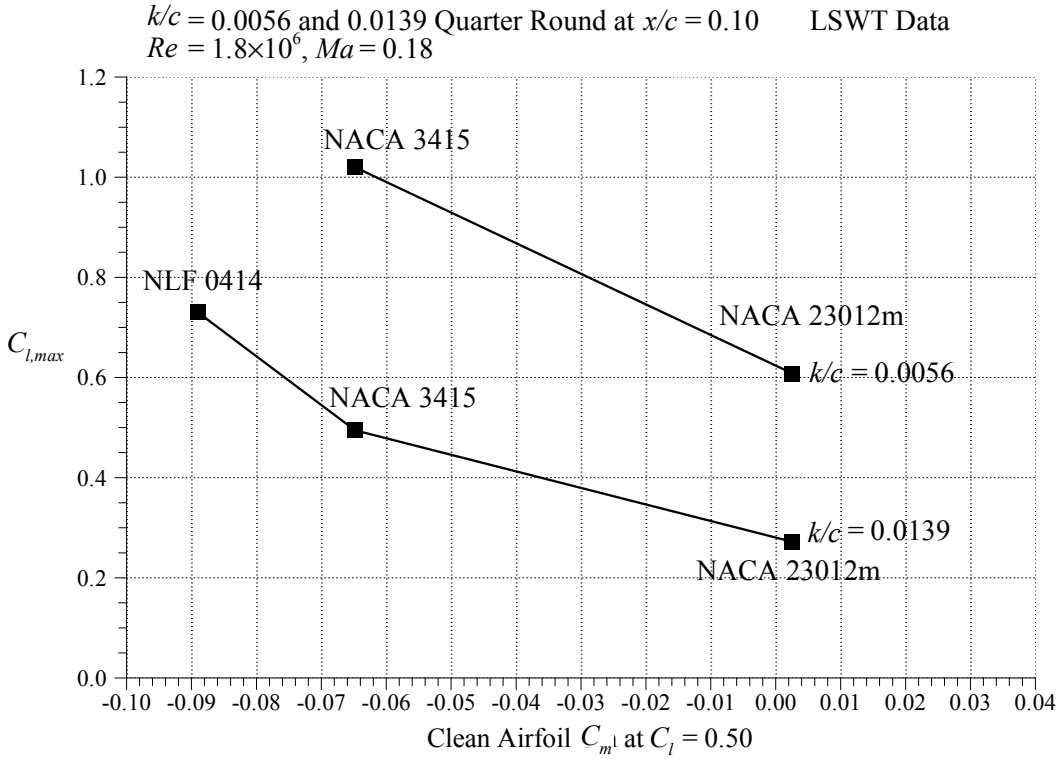

FIGURE 84. VARIATION OF ICED AIRFOIL $C_{l,max}$ WITH CLEAN AIRFOIL PITCHING MOMENT FOR THE THREE AIRFOILS TESTED AT LSWT

6. SUMMARY, CONCLUSIONS, AND RECOMMENDATIONS.

6.1 SUMMARY.

This report presents the results of a 3-year investigation into the effect of ice shape and airfoil geometry on airfoil performance. The overall objective was to improve ones understanding of the relationship between airfoil geometry, ice shape geometry, and the resulting aerodynamic performance degradation. Additional objectives included applying the results to a critical ice shape methodology and determining the effects of Reynolds number and Mach number variations.

Aerodynamic performance testing was carried out on three airfoils: NACA 23012, NLF 0414, and NACA 3415. These sections exhibited a large variation in aerodynamic characteristics. The NACA 23012 is a traditional forward-loaded, low pitching moment airfoil. In contrast, the NLF 0414 airfoil was designed to maintain laminar flow over most of the upper surface. This resulted in a more uniform pressure loading over the forward and mid-chord regions. The NACA 3415 airfoil had aerodynamic characteristics between the other two.

Each of these airfoils was tested with a variety of simulated ice shapes. The three general types of ice shapes considered were supercooled large droplet (SLD), ridge-type ice, intercycle ice, and glaze horn-type ice. The SLD ridge ice was simulated with a wooden forward-facing quarter round that was tested at several chordwise locations on the airfoils. Four intercycle ice shapes were simulated using built-up roughness that was scaled from actual accretions on the NACA 23012 airfoil. Uniform roughness in the form of 80- and 150-grit sandpaper was also tested since this represents a standard roughness that can easily be applied to other tests and has sometimes been used to represent residual or intercycle ice. The glaze horn-type ice was simulated with simple geometric shapes having triangular cross sections and no spanwise variation. These shapes were sized from measurements of upper surface glaze ice horns. Three sizes were tested at several locations on the airfoil leading edge.

The full parametric variation of ice shape simulations and airfoil geometry testing was carried out at the University of Illinois, using the Low-Speed Wind Tunnel (LSWT). The NACA 23012, NLF 0414, and NACA 3415 airfoil models had an 18-inch chord and a 25% simple flap. The lift coefficient, drag coefficient, pitching-moment coefficient, flap hinge moment coefficient, and surface pressure coefficients were acquired during angle of attack sweeps at $Re = 1.0\times10^6$, $Ma = 0.10$ and $Re = 1.8\times10^6$, $Ma = 0.18$. In addition, higher Reynolds number and Mach number testing was performed for a subset of the ice shape matrix on the NACA 23012 airfoil. This testing was conducted at the NASA Langley Low-Turbulence Pressure Tunnel (LTPT), using an unflapped, 36-inch chord model. Since this was a pressure tunnel, a large range of Reynolds numbers (from 2.0×10^6 to 10.6×10^6) and Mach numbers (from 0.10 to 0.28) were tested.

6.1.1 Supercooled Large Droplet, Ridge-Type Ice Accretions.

The results with SLD ice simulations indicated large performance degradations on all three of the airfoils tested. In terms of maximum lift, the penalties were most severe for the NACA 23012 airfoil. In this case, $C_{l,max}$ was reduced to about 0.25 from a clean value of 1.51 (NACA 23012m

flapped model, $C_{l,max}$ = 1.47 for NACA 23012 unflapped model) for a k/c = 0.0139 quarter round located at x/c = 0.10. For the NACA 3415 airfoil with the same shape located at x/c = 0.20, the $C_{l,max}$ was about 0.30 compared to a clean value of 1.35. For the NLF 0414 airfoil, the lowest $C_{l,max}$ measured was 0.58 compared to a clean value of 1.34 with the quarter round located at x/c = 0.30. All of these results were for $Re = 1.8\times10^6$ and Ma = 0.18.

Higher Reynolds number and Mach number testing was also performed for the NACA 23012 airfoil. The clean results showed that the performance, particularly maximum lift, is a strong function of Reynolds number. The $C_{l,max}$ increased to a value of 1.80 for $Re = 10.5\times10^6$ and Ma = 0.21. Mach number had a small effect on maximum lift with the value decreasing with increasing Mach number. Tests performed at the LTPT with the k/c = 0.0139 quarter round on the NACA 23012 airfoil yielded several important results.

- The tests showed that Reynolds number variations (from $Re = 2.0\times10^6$ to 10.5×10^6 at Ma = 0.10 to 0.12) did not significantly affect the iced airfoil performance (including maximum lift). It should be noted that there was a small (less than 0.10) increase in $C_{l,max}$ when the ice shape was located at x/c = 0.20 and no increase when the ice shape was located at x/c = 0.02 and 0.10.

- Mach number variations (from 0.10 to 0.28) played a more significant role in the iced airfoil performance. Reductions (with increasing Mach number) of 0.10 to 0.15 in $C_{l,max}$ were typical.

- A simple geometric scaling of the quarter-round ice simulation between the 18-inch chord LSWT model and 36-inch chord LTPT model yielded excellent results in terms of iced airfoil performance for the NACA 23012. The results also showed that agreement between these two facilities was achieved at closely matched Mach numbers because of the relative Reynolds number insensitivity.

6.1.2 Intercycle Ice Accretions.

Performance testing with built-up roughness intercycle ice simulations performed on the 18-inch chord NACA 23012 airfoil model at LSWT were compared to LTPT results from intercycle ice shape casting simulations. Very good agreement was observed, thus validating the roughness simulation and simple geometric scaling method. The performance penalties were not as large as those caused by the SLD ridge-type ice, but were still very significant. The intercycle ice simulations produced maximum lift values in the range of 0.65 to 0.80 for the NACA 23012 airfoil. These same simulations, when tested on the NACA 3415 and NLF 0414 airfoils, resulted in $C_{l,max}$ values of 0.85 to 0.95 and 0.90 to 1.05, respectively. Similar to the SLD ridge-type ice results, the more severe degradations were for the NACA 23012 airfoil section, in terms of maximum lift. In terms of moderate lift coefficients (0.20 to 0.60 for the clean airfoil), the intercycle ice shapes reduced the lift curve slope and caused more severe lift penalties on the NACA 3415 and the NLF 0414 airfoils compared to the NACA 23012 airfoil.

In contrast to the built-up roughness simulations, tests were also performed with 80- and 150-grit sandpaper applied to the leading edge from x/c = 0.07 on the upper surface to x/c = 0.10 on the lower surface. These results for the NACA 23012 airfoil were compared to LTPT tests

performed with 40- and 80-grit sandpaper. These sizes are approximately the geometrically scaled equivalent of each other, and the data again showed good agreement between the two facilities at closely matched Reynolds and Mach numbers. The effect of the sandpaper roughness was much less severe than the intercycle ice simulations. For example, maximum lift on the NACA 23012 airfoil was reduced to a range of 1.10 to 1.15. The 80- and 150-grit sandpaper tested on the NACA 3415 and the NLF 0414 airfoils resulted in $C_{l,max}$ values of 1.05 to 1.10 and 1.20 to 1.25, respectively.

Results from LTPT testing on the NACA 23012 airfoil with the intercycle ice shapes showed that the lift performance was not significantly affected by changes in Reynolds and Mach numbers over the range tested. The sandpaper roughness, being smaller in height and more uniform in distribution, resulted in lift performance that was more sensitive to Reynolds and Mach numbers effects. Details of these results were presented and discussed in an earlier report.

6.1.3 Glaze Horn-Type Accretions.

The simulation method for the glaze horn-type ice accretion allowed for parametric variation of ice horn features such as tip radius, height, and surface location (horn angle). In this study, the horn angle was always normal to the airfoil surface at the specified horn location. The results of testing on the three airfoils showed that the tip radius of the horn was probably the least important geometric characteristic in terms of iced airfoil performance. The horn height and surface location had much greater effects on performance. For locations near the leading edge, the horn height did not significantly effect the maximum lift values. On the NACA 3515 airfoil, increasing the horn height from k/c = 0.0200 to 0.0667 decreased the $C_{l,max}$ from 1.20 to 1.10 when located at s/c = 0.000. The same height range caused the $C_{l,max}$ to decrease from 0.75 to 0.52 when located downstream at s/c = 0.034. For all three airfoils tested, the $C_{l,max}$ decreased almost linearly with ice shape locations from s/c = 0.000 to 0.034, with the larger-sized horns resulting in lower $C_{l,max}$ values for each airfoil. Similar to the results for the other two ice shape classes, the NACA 23012 airfoil generally had the lowest maximum lift coefficients with the glaze horn ice simulations.

A small subset of these ice simulations was tested on the NACA 23012 airfoil at the LTPT. As for the other two ice shape types, the geometric scaling of the shapes between the two facilities led to very good agreement in the performance results. Typical iced airfoil behavior with varying Reynolds and Mach numbers was observed. That is, an increase in *Re* from 2.0×10^6 to 10.5×10^6 had very little effect on the performance coefficients. The s/c = 0.000 ice shape location showed more Reynolds number sensitivity than did the s/c = 0.034 location. Increases in Mach number from 0.10 to 0.28 tended to cause small decreases in maximum lift. This was more readily observed for the s/c = 0.034 location, thus, it was opposite of the Reynolds number effect.

6.2 CONCLUSIONS.

A major conclusion of this study is that the chordwise location of an ice accretion feature is equally important as its size in determining the airfoil performance degradation, particularly in terms of maximum lift. For the NACA 23012 airfoil, a quarter-round shape with height k/c = 0.0139 resulted in a $C_{l,max}$ of less than 0.25 when located in the range of x/c = 0.10 to 0.20.

However, a glaze horn-type shape with height $k/c = 0.0667$ (nearly five times larger) located at $s/c = 0.034$ (close to the leading edge) resulted in a higher $C_{l,max}$ of approximately 0.30. Therefore, a much smaller ice accretion, located further downstream of the leading edge, caused nearly the same or larger performance loss (in terms of $C_{l,max}$). This same trend was also true for the NACA 3415 airfoil. For the NLF 0414 airfoil, the lowest $C_{l,max}$ measured with the $k/c = 0.0139$ quarter round was 0.58 when located further downstream at $x/c = 0.30$. The lowest $C_{l,max}$ with the much larger ($k/c = 0.0667$) glaze-horn shape was similar at 0.51. The results of this study showed that areas close the leading edge were not necessarily the most sensitive in terms of ice accretion performance degradation. In all cases tested, the smallest performance loss occurred when the ice shape was located at the leading edge ($x/c = s/c = 0.000$).

This study supports the conclusion than an airfoil's load distribution plays a signal role in its sensitivity to ice accretion, particularly in the first 20% chord where ice is most likely to accrete. The results with SLD ridge-type ice simulations generally indicated that more front-loaded airfoils tended to be more sensitive to these types of ice accretion. Of the three airfoils tested, the NACA 23012 was the most front-loaded and had the largest performance degradation due to spanwise ridge ice accretions, especially when located in the range of $x/c = 0.10$ to 0.20. The NLF 0414 airfoil, which was the most aft-loaded of the three airfoils tested, was the least sensitive to SLD ice simulations. The NACA 3415 had a pressure loading between the NACA 23012 and NLF 0414 airfoils. The results of this study further showed that the performance penalties with the SLD ice simulations were also between the other two airfoils. This trend was also generally true for the other two types of ice shapes tested. The clean airfoil load distribution directly affects the global pressure distribution imposed on the separation bubble generated by the ice shape. For more front-loaded airfoils, the separation bubble is forced to recover more pressure, causing complete flow separation at lower angles of attack. Thus, more front-loaded airfoils tend to exhibit larger performance penalties with ice accretion. These conclusions directly contributed to the application of the results to a methodology for determining a critical ice shape.

The results of this study have shown that Reynolds and Mach number effects are small for ice-contaminated airfoils. There was little variation in the integrated aerodynamic coefficients for a Reynolds number range from 1.0×10^6 to 10.5×10^6 and over a Mach number range from 0.10 to 0.28. Because of this Reynolds and Mach numbers insensitivity, a geometric scaling of full-size airfoil section and ice accretion to small sizes suitable for small wind tunnels can yield very acceptable performance results. Based upon the excellent agreement between the higher Reynolds number LTPT results and the low Reynolds number LSWT results, the conclusions reached from the extensive parametric studies on ice shape size, location, and other factors are felt to be reliable when applied to flight Reynolds numbers. There can still be significant Reynolds and Mach numbers effects on clean airfoils. If the changes in the aerodynamic coefficients due to icing (when compared to the clean airfoil) need to be known, these effects could be significant. However, clean airfoil data at high Reynolds and Mach numbers can be more readily obtained through computational methods, historical data, or lower-cost (relative to iced configuration) aerodynamic testing.

6.3 RECOMMENDATIONS.

Recommendations for future study focus on expanding the airfoil and ice shape database and testing models that are more similar to actual airframe configurations. For example, the three ice shape types considered here should be tested on airfoils that are actually in service today. A business jet main wing airfoil and large commercial transport horizontal tail airfoil are two reasonable candidates. The ice shape types should be expanded to look more at SLD accretions and runback-type accretions resulting from anti-icing systems. The ice shapes should be tested with three-dimensional wing configurations to simulate actual airframe configurations. This could involve spanwise variations in the ice simulations as well as wing parameters like taper and sweep. Future tests should also consider models with more advanced flap systems to gauge the airfoil geometry trends found in this study.

7. REFERENCES.

1. Bragg, M.B. and Loth, E., "Effects of Large-Droplet Ice Accretion on Airfoil and Wing Aerodynamics and Control," FAA Report DOT/FAA/AR-00/14, April 2000.

2. "Report of the 12A Working Group on Determination of Critical Ice Shapes for the Certification of Aircraft," FAA Report DOT/FAAA/AR-00/37, 2000.

3. Lee, S., "Effects of Super-Cooled Large-Droplet Icing on Airfoil Aerodynamics," Ph.D. Dissertation, Dept. of Aeronautical and Astronautical Engineering, University of Illinois, Urbana, IL, May 2001.

4. Lee, S. and Bragg, M.B., "Effects of Simulated-Spanwise Ice Shapes on Airfoils: Experimental Investigation," AIAA Paper 99-0092, January 1999.

5. Lee, S., Kim, H.S., and Bragg, M.B., "Investigation of Factors that Influence Iced Airfoil Aerodynamics," AIAA Paper 2000-0099, January 2000.

6. Lee, S. and Bragg, M.B., "An Experimental Investigation of Simulated Large-Droplet Ice Shapes on Airfoil Aerodynamics," *Journal of Aircraft*, Vol. 36, No. 5, September-October 1999, pp. 844-850.

7. Broeren, A.P. and Bragg, M.B., "Effect of Residual and Intercycle Ice Accretions on Airfoil Performance," FAA Report DOT/FAA/AR-02/68, May 2002.

8. Broeren, A.P., Addy, H.E., Jr., and Bragg, M.B., "Effect of Intercycle Ice Accretions of Airfoil Performance," AIAA Paper 2002-0240, January 2002.

9. Kim, H.S. and Bragg, M.B., "Effects of Leading-Edge Ice Accretion Geometry on Airfoil Aerodynamics," AIAA Paper 99-3150, June 1999.

10. Broeren, A.P., "An Experimental Study of Unsteady Flow Over Airfoils Near Stall," Ph.D. Dissertation, Dept. of Mechanical and Industrial Engineering, University of Illinois, Urbana, IL, January 2000.

11. Noe, S.C., "Force Balance Measurements of Wind-Turbine Airfoil Performance With Simulated Leading-Edge Ice Accretions," M.S. Thesis, Dept. of Aeronautical and Astronautical Engineering, University of Illinois, Urbana, IL, 1996.

12. Rae, W.H. and Pope, A., *Low-Speed Wind Tunnel Testing*, 2nd Ed., John Wiley & Sons, New York, 1984.

13. Allen, H.J. and Vincenti, W.G., "Wall Interference in a Two-Dimensional-Flow Wind Tunnel, With Consideration of the Effect of Compressibility," NACA Report No. 782, 1944.

14. Von Doenhoff, A.E. and Abbott, F.T., Jr., "The Langley Two-Dimensional Low-Turbulence Pressure Tunnel," NACA TN 1283, May 1947.

15. McGhee, R.J., Beasley, W.D., and Foster, J.M., "Recent Modifications and Calibration of the Langley Low-Turbulence Pressure Tunnel," NASA TP 2328, July 1984.

16. Paschal, K., Goodman, W., McGhee, R., Walker, B., and Wilcox, P.A., "Evaluation of Tunnel Sidewall Boundary-Layer-Control Systems for High-Lift Airfoil Testing," AIAA Paper 91-3243, September 1991.

17. Jackson, D.G. and Bragg, M.B., "Aerodynamic Performance of an NLF Airfoil With Simulated Ice," AIAA Paper 99-0373, January 1999.

18. Jackson, D.G., "Effect of Simulated Ice and Residual Ice Roughness on the Performance of a Natural Laminar Flow Airfoil," M.S. Thesis, Dept. of Aeronautical and Astronautical Engineering, University of Illinois, Urbana, IL, 1999.

19. Shin, J. and Bond, T.H., "Repeatability of Ice Shapes in the NASA Lewis Icing Research Tunnel," *Journal of Aircraft*, Vol. 31, No. 5, September-October 1994.

20. McCullough, G.B. and Gault, D.E., "Examples of Three Representative Types of Airfoils-Section Stall at Low-Speed," NACA TN 2502, September 1951.

21. Abbott, I.H. and von Doenhoff, A.E., *Theory of Wing Sections*, Dover Publications, 1959.

22. Drela, M., "XFOIL 6.6 User Primer," *MIT Aero and Astro Engineering*, March 14, 1996.

23. Ladson, C.L., "Effects of Independent Variation of Mach and Reynolds Numbers on the Low-Speed Aerodynamic Characteristics of the NACA 0012 Airfoil Section," NASA TM-4071, October 1988.

24. Addy, H.E., Jr. and Chung, J.J., "A Wind Tunnel Study of Icing Effects on a Natural Laminar Flow Airfoil," AIAA Paper 2000-0095, January 2000.

25. Morgan, H.L., Jr., Ferris, J.C., and McGhee, R.J., "A Study of High-Lift Airfoils in the Langley Low-Turbulence Pressure Tunnel," NASA TM 89125, July 1987.